Ultra-Cold CsLi Molecules as a Platform for Quantum Information Processing

by

Zach Hinkle

A thesis
presented to the University of Waterloo
in fulfillment of the
thesis requirement for the degree of
Master of Science
in
Physics (Quantum Information)

Waterloo, Ontario, Canada, 2022

Author's Declaration

I hereby declare that I am the sole author of this thesis. This is a true copy of the thesis, including any required final revisions, as accepted by my examiners.

I understand that my thesis may be made electronically available to the public.

Abstract

Despite their proposal 40 years ago, quantum computers are still in their infancy, with a panoply of various systems demonstrated as potential methods of quantum information processing. Rydberg atoms are a leading platform, but their method of performing entangling operations is limited by the natural lifetimes of Rydberg states, which is on the order of 100 μs. Molecules could perform entangling gates similar to Rydberg atoms with the advantage that molecular states are much longer lived, on the order of 100s of milliseconds. Despite this, no experiment has been performed using molecules for quantum computing. This thesis investigates the feasibility of using molecules for quantum computing as well as presents a new method for producing an atomic beam, designed by the author, that allows for a more economical production of atoms while avoiding heating problems present with traditional ovens.

Acknowledgements

I would like to express my immense gratitude to professor Alan Jamison for his tutelage and guidance. The insights I've gained from Alan, as well as his method of conceptualizing and understanding physical problems have given me a skill set that will undoubtedly serve me well in my future endeavors.

Next, I am greatly indebted to Paul del Franco for being an excellent friend and even better lab partner. Paul has been at my side assisting with every step of the data collection process, and this thesis would not have been possible with so little stress if not for him.

Finally, I'd like to thank Aryan, Candice, Forouzan, Hyo-Sun, and Omar for their camaraderie and willingness to always hear me ham it up on the piano downstairs at a moments notice!

Table of Contents

List of Figures

List of Tables

List of Abbreviations

2D MOT two-dimensional magneto-optical trap vii, 27–31, 34–36, 49

AC alternating current 68

ASME American Society of Mechanical Engineers 26

BEC Bose-Einstein condensate 2, 4, 16, 19

BQP bounded quantum polynomial 22, 23

Ca calcium 65, 66

CaCl calcium chloride 65

CAD computer aided design vii, viii, 28, 50, 52–54

CF ConFlat 26, 27

CNOT controlled-NOT viii, 1, 3, 72–78, 84, 86

Cs cesium 2, 64, 67

CsCl cesium chloride 65, 66

CsLi cesium lithium 2, 20, 25, 49, 75, 76, 78

CZ controlled-Z 73, 75

DC direct current 44–46, 68

EOM electro-optic modulator 38, 40

FM frequency modulation vii, 38–41

FWHM full width at half-maximum 9, 69

ID inner diameter 27, 63

Li lithium 2

MOT magneto-optical trap vii, 3, 13–15, 30, 33, 49, 57–59, 64, 71, 86

NASA national aeronautics and space administration 57

NEG non-evaporable getter 30, 31, 35, 36

NIST national institute of standards and technology 55

NMR nuclear magnetic resonance 20

NP non-deterministic polynomial 22

NPT American national standard taper pipe thread 51, 52

OD outer diameter 27, 63

ODT optical dipole trap 33

PM polarization maintaining vii, 43, 44

SI international system of units 26

Ti:Sub titanium sublimation 32, 36

UHV ultra-high vacuum 2, 26, 30, 32, 33, 47, 49, 57, 59, 60

USC United States customary 26

Chapter 1

Introduction

Quantum computing aims to perform information processing by leveraging quantum phenomena such as entanglement and interference. Information stored in a quantum system—quantum bits, or qubits—can be manipulated in ways not possible with classical systems. This allows for quantum computers to solve certain problems more efficiently than classical computers in theory [25, 50]. In practice, the problems are far from solved. There is not yet a clear platform for use as qubits. Among the possible choices, Rydberg atoms are a leading platform. Molecules could be used to perform quantum computing analogous to Rydberg atoms, while offering the advantage of having many longer-lived states. This is the subject of Chapter 5 which explores a method of performing controlled-NOT (CNOT) gates with molecules. A formula is derived for the fidelity of the gate as a function of the gate time, and shows that high fidelities (99.9%) can be achieved with gate times fast enough to perform thousands of gate operations in a coherence time. The derived fidelity is a best estimate, and future work will be needed to carefully analyze and incorporate technical problems that could be encountered in the implementation. A perturbative approximation of the fidelity is also made that allows for greatly simplifying the form of the fidelity formula. This simple formula will be helpful for planning future research in the lab devoted to quantum computing with ultracold molecules.

These feasibility calculations are an important part of planning future experimental work. However, the process of transitioning from an empty lab to full fledged ultracold atomic and molecular physics experiments requires a tremendous amount of designing and building of the experimental apparatus. First, in Chapter 2, a background on the techniques for cooling and trapping atoms is given, as well as a discussion of some major works in the field of atomic physics. Namely, Bose-Einstein condensation, and the superfluid to Mott insulator transition. Cooling atoms to ultracold temperatures allows researchers a

high degree of control of the atoms, and Bose-Einstein condensates (BECs) show that this control can be extended to fundamentally quantum systems as well. The superfluid to Mott insulator transition capitalizes on this control to allow for studying many-body physics. In particular, it can be used as a tool to help explore the low temperature regime of the Fermi-Hubbard model, which is numerically intractable but believed to contain essential information on the nature of superconducting phase transitions.

BECs, superfluid to Mott insulator transitions, and the experiments we plan to do must all be performed in ultra-high vacuum (UHV), and so require a specially designed vacuum chamber. This is the subject of Chapter 3, which presents the layout of the newly designed vacuum chamber. The vacuum chamber's overall design is a new design of the adviser, all the details of which have been worked out by the author. It is mostly designed from stock vacuum fittings, though a handful of parts are custom pieces designed by the author. It will be used to make gases of cesium (Cs) and lithium (Li) atoms, as well as cesium lithium (CsLi) molecules. The choice of CsLi molecules is for its large dipole moment. An attractive feature of molecules over atoms is their ability to interact via dipole-dipole interactions which atoms, generally, do not. Their qualitatively different interaction behavior leads to the expectation of qualitatively different physics in a BEC.

To make these atoms and molecules, the vacuum chamber requires a method of producing an atomic beam source. Previous designs for producing atomic beams have several draw backs that this thesis aims to solve. Namely, past designs either rely on expensive equipment—such as dispensers—or inefficient nozzles and heating methods. In Chapter 4, a new design is introduced that aims to overcome these drawbacks. In addition, it has been designed to require minimal machining of custom parts. It is a new design that is roughly based on the design of molecular beam epitaxy ovens. The temperature range of the oven is ambient room temperature to a maximum of 450°C. This temperature range allows for the production of cesium and lithium vapors of sufficient pressure to produce an atomic beam. At its maximum operating temperature, the exterior of the vacuum chamber reaches only 60°C. Having such a lower exterior temperature minimizes the temperature gradient near the chamber. Temperature gradients can lead to optics slowly misaligning over time, and air currents that can stir up dust onto the optics. Furthermore, a high temperature exterior makes stabilizing the ambient temperature more challenging.

In addition, working with pure cesium provides its own challenges, as it is highly reactive with water—even the water vapor present in the air. To avoid the dangers of working with pure cesium, the new design was tested using a cesium salt reaction as a source for a cesium gas which produces fluxes ranging from the order of 10^{11} to 10^{12} atoms s^{-1} cm^{-2} over the temperature range 325 to 380°C, and is projected to reach a flux on the order of 10^{13} atoms s^{-1} cm^{-2} near 400°C. These flux rates lead to a prediction for the loading of a

magneto-optical trap (MOT) in about 1 second. Loading of a MOT is usually the first step in trapping atoms for ultracold experiments, and the load rate of this oven allows for fast turn around times between runs of an experiment, such as performing the CNOT gates with molecules outlined in Chapter 5.

Chapter 2

Scientific Background

Quantum computing with atoms and molecules requires the use of many different experimental techniques. The atoms must be cooled and trapped so they can be individually addressed, then they must be manipulated in some way to perform gate operations. Central to using atoms and molecules (and many other platforms) for quantum computing is the two-level system. Its use extends far beyond manipulating qubits, and so will be discussed first followed by a discussion of common techniques for cooling and trapping atoms. Some major experiments of the field are briefly discussed to give context to the richness of the field of cold atoms. Specifically, BECs are discussed, along with with superfluid to Mott-insulator transition in BECs. These two experiments are cornerstones of the field, as they demonstrate the ability for precise control of fundamentally quantum systems, and the ability to perform quantum simulation with cold atoms.

2.1 The Two-Level System

When laser light interacts with an atom, under certain conditions it can be well approximated by a two-level system model. The present discussion will be confined to alkali atoms for simplicity, but the two-level approximation can be used in many situations beyond just atoms.

In atomic physics experiments, and in laser cooling, what one is often interested in is how the valence electron is affected by whatever is influencing the atom. As in the solution to the hydrogen atom, the valence electron has a theoretically infinite number of energy states available to it; the problem then is predicting which of these states the

electron is occupying (or what superposition of states as the case may be). In the two-level approximation, we restrict our attention to only two of these energy levels: the ground state (because the atom will always decay back to the ground state), and one excited state. For the case of atoms irradiated by a laser, the excited state is chosen by the laser frequency. The laser frequency ν is related to the atom's energy E via $E = h\nu$ where h is Planck's constant. If this energy is near the energy difference between the ground state and an excited state, and there is not another excited state with similar energy, we can make a two-level approximation (Chapter 2 of Reference [13]).

To understand the effects of light coupling with the atom, we begin with the atom's Hamiltonian. The eigenstates of the atom's Hamiltonian, by definition, satisfy the eigenvalue equation

$$\hat{H}_0|i\rangle = E_i|i\rangle \tag{2.1}$$

and these states are simply the unperturbed energy states of the atom. For concreteness, we can label the ground state as $|0\rangle$ and the excited state of interest as $|1\rangle$ so we have

$$\hat{H}_0|0\rangle = E_0|0\rangle \tag{2.2}$$

$$\hat{H}_0|1\rangle = E_1|1\rangle \tag{2.3}$$

for these two levels where we shall assume $E_1 > E_0$ and $E_0 \neq E_1$. We are here assuming that the states $|0\rangle$ and $|1\rangle$ are the only states with their respective energies. A real atom may have degeneracies that require additional techniques (such as applying a magnetic field to break degeneracies), but the overall picture remains the same.

Next we include the interaction of the atom with laser radiation. To do so, we begin with the expression for a monochromatic plane wave

$$\mathbf{E} = \mathbf{E}_\mathrm{a} \exp[i(\mathbf{k}\cdot\mathbf{x} - \omega t)] \tag{2.4}$$

where $\mathbf{E}_\mathrm{a}$ is an arbitrary constant electric field, assumed real here for simplicity. The spatial portion of the light wave can be Taylor expanded and terms beyond zeroth order can be neglected. This is because the quantity $\mathbf{k}\cdot\mathbf{x}$ is vanishingly small even at first order which can be seen as follows. For light interacting with an atom, the wavelength is on the order of 10^{-7} meters, leading to a wavenumber on the order of 10^7 inverse meters. The position of the valence electron meanwhile is on the order of several Bohr radii i.e. 10^{-10} meters hence $\mathbf{k}\cdot\mathbf{x} \sim \mathcal{O}(10^7 \times 10^{-10}) = \mathcal{O}(10^{-3})$. This leads to

$$\mathbf{E} = \mathbf{E}_\mathrm{a}(1 + \mathcal{O}(\mathbf{k}\cdot\mathbf{x}))\exp(-i\omega t). \tag{2.5}$$

We then need the real part of this field which leads to

$$\mathfrak{Re}(\mathbf{E}) = \mathbf{E}_\mathrm{a}(\exp(-i\omega t) + \exp(i\omega t))/2. \tag{2.6}$$

We can see how this light interacts with the atom by considering the interaction from the perspective of the atom's valence electron. This electron sees the rest of the atom as a positively charged core which together with the electrons forms a physical dipole. The energy of a dipole $\mathbf{d}$ in an electric field is given by $\mathcal{E} = -\mathbf{d} \cdot \mathbf{E}$ and so the correction term to our Hamiltonian becomes

$$\delta\hat{H} = -e\mathbf{r} \cdot \mathfrak{Re}(\mathbf{E}) \tag{2.7}$$

where $\mathbf{r}$ is the position operator of the electron relative to the nucleus. This leads to the full Hamiltonian

$$\hat{H} = \hat{H}_0 + \delta\hat{H} = \hat{H}_0 - e\mathbf{r} \cdot \mathfrak{Re}(\mathbf{E}) = \hat{H}_0 - e\hat{\mathbf{r}} \cdot \mathbf{E}_\mathrm{a}/2(\exp(-i\omega t) + c.c.). \tag{2.8}$$

The following discussion will benefit from expressing the full Hamiltonian in matrix form. We will express Equation 2.7 in the eigenbasis of $\hat{H}_0$, and therefore, due to the parity of the position operator, all diagonal terms of δH are zero. Meanwhile, the off diagonal terms are all of the form

$$H_{ij} = \langle i|\hat{H}|j\rangle = \langle i|e\mathbf{r} \cdot \mathbf{E}_\mathrm{a} e^{i\omega t}|j\rangle, \; i \neq j. \tag{2.9}$$

To cut down on notation, we first define the Rabi frequency as

$$\Omega = \frac{\langle 0|e\mathbf{r} \cdot \mathbf{E}_\mathrm{a}|1\rangle}{\hbar} \tag{2.10}$$

thus leading to the matrix

$$\delta\hat{H} = -\hbar \begin{bmatrix} 0 & \frac{\Omega}{2}(e^{i\omega t} + e^{-i\omega t}) \\ \frac{\Omega}{2}(e^{-i\omega t} + e^{+i\omega t}) & 0 \end{bmatrix}. \tag{2.11}$$

This Hamiltonian can be simplified by applying a rotating wave approximation [20, 24]. To see this, we begin by transforming into the interaction picture using the unitary operator $\hat{U} = \exp(i\hat{H}_0 t/\hbar)$ (the interaction picture is discussed in Chapter 5 of Reference [46]). Making the transformation

$$|\psi\rangle \to \hat{U}|\psi\rangle \tag{2.12}$$

the Schrödinger equation becomes

$$\hat{U}^\dagger \frac{d}{dt}(\hat{U}|\psi\rangle) = i\hbar\hat{U}^\dagger \hat{H}\hat{U}|\psi\rangle \tag{2.13}$$

where the $\hat{U}^\dagger$ terms are included to preserve unitarity [46]. Expanding the left hand side and collecting derivatives of $|\psi\rangle$ on one side shows that $\hat{H}$ transforms as

$$\hat{H} \to \hat{U}^\dagger \hat{H}\hat{U} - i\hbar\hat{U}^\dagger \frac{d\hat{U}}{dt}. \tag{2.14}$$

For simplicity, we may redefine our zero for energy so that

$$\hat{H}_0 = \begin{bmatrix} 0 & 0 \\ 0 & (E_1 - E_0) \end{bmatrix} = \begin{bmatrix} 0 & 0 \\ 0 & \hbar\omega_0 \end{bmatrix} \tag{2.15}$$

where in the final equality ω_0 has been defined as $\omega_0 = (E_1 - E_0)/\hbar$. Taylor expanding $\hat{U}$ leads to

$$\hat{U} = \begin{bmatrix} 1 & 0 \\ 0 & 1 \end{bmatrix} + i \begin{bmatrix} 0 & 0 \\ 0 & \omega_0 \end{bmatrix} t + i^2 \begin{bmatrix} 0 & 0 \\ 0 & \omega_0 \end{bmatrix}^2 t^2 + ... = \begin{bmatrix} 1 & 0 \\ 0 & e^{i\omega_0 t} \end{bmatrix}. \tag{2.16}$$

This transformation can be thought of as transforming to a new reference frame where the state $|1\rangle$ is now rotating in the complex plane with frequency ω_0. Applying this transformation to Equation 2.7 we get

$$\delta\hat{H} \rightarrow \hat{U}^\dagger \delta\hat{H}\hat{U} - i\hbar\hat{U}^\dagger \frac{d\hat{U}}{dt} = -\hbar \begin{bmatrix} 0 & \frac{\Omega}{2}\left(e^{i(\omega_0-\omega)t} + e^{i(\omega_0+\omega)t}\right) \\ \frac{\Omega}{2}\left(e^{-i(\omega_0-\omega)t} + e^{-i(\omega_0+\omega)t}\right) & -\omega_0 \end{bmatrix}. \tag{2.17}$$

Here the rotating wave approximation can be made. Because in this two-level approximation we assumed that $\omega \sim \omega_0$, the terms $\omega_0 - \omega$ will be close to zero while $\omega + \omega_0$ will be near $2\omega_0$ which is many orders of magnitude greater. As such, the oscillations from $\omega + \omega_0$ will average to zero over time scales of interest, such as the time to transition from the ground to excited state. The time to transition from ground to excited state is governed by the Rabi frequency, which is typically on the order of kHz, while the atomic transition frequency is typically on the order of 100s of THz.

That the terms $\omega + \omega_0$ will average to zero amounts to dropping these terms from the Hamiltonian. This leads to

$$\delta\hat{H} \approx \delta\hat{H}' = -\hbar \begin{bmatrix} 0 & \frac{\Omega}{2}\left(e^{i(\omega_0-\omega)t}\right) \\ \frac{\Omega}{2}\left(e^{-i(\omega_0-\omega)t}\right) & -\omega_0 \end{bmatrix}. \tag{2.18}$$

We may now transform back to the non-rotating frame:

$$\delta\hat{H}' \rightarrow \hat{U}\delta\hat{H}'\hat{U}^\dagger - i\hbar\hat{U}\frac{d\hat{U}^\dagger}{dt} = -\hbar \begin{bmatrix} 0 & \frac{\Omega}{2}\left(e^{-i\omega t}\right) \\ \frac{\Omega}{2}\left(e^{i\omega t}\right) & 0 \end{bmatrix}. \tag{2.19}$$

Noting that this transformation and its inverse does not affect H_0 (since the approximation does not affect any terms in H_0), the total Hamiltonian thus becomes

$$\hat{H} \approx \hat{H}' = \hbar \begin{bmatrix} 0 & \frac{\Omega}{2}\left(e^{-i\omega t}\right) \\ \frac{\Omega}{2}\left(e^{i\omega t}\right) & \omega_0 \end{bmatrix}. \tag{2.20}$$

This has simplified the Hamiltonian, but it can be simplified further. Specifically, we would like to totally remove the time dependency from the Hamiltonian. This is because time-dependent Hamiltonians require much more complex mathematical techniques to analyze. After the rotating wave approximation, a transformation to the dressed atom picture. The dressed atom picture is discussed at length in Reference [13]. Functionally, it serves to move the time dependencies out of the Hamiltonian and onto the states. This is done with the unitary matrix

$$\hat{U}_{\mathbf{d}} = \begin{bmatrix} 1 & 0 \\ 0 & e^{-i\omega t} \end{bmatrix}. \tag{2.21}$$

Applying this transformation, $\hat{H}'$ becomes

$$\hat{H}' = \hbar \begin{bmatrix} 0 & \frac{\Omega}{2} \\ \frac{\Omega}{2} & \omega_0 - \omega \end{bmatrix} = \hbar \begin{bmatrix} 0 & \frac{\Omega}{2} \\ \frac{\Omega}{2} & -\delta \end{bmatrix} \tag{2.22}$$

where in the last equality, we have substituted in the detuning $\delta = \omega - \omega_0$. This is the two-level system Hamiltonian in the rotating wave approximation and dressed atom picture. This Hamiltonian allows for one to predict the time evolution of an atom interacting with laser radiation. The off-diagonal terms couple the ground and excited states through the Rabi frequency, Ω, and hence set an important time scale for the atom-light interaction. For instance, if the ground and excited states were being used as the $|0\rangle$ and $|1\rangle$ states for quantum computing, the Rabi frequency sets the speed at which bit flips can be performed (this will be seen in detail in Chapter 5). The Hamiltonian however provides no information about the lifetimes of the states—another important time scale for quantum computing.

While the Rabi frequency sets the speed at which a bit flip can be performed, the excited state lifetime limits how long information can be stored in the qubit before being lost to spontaneous decay. For dipole transitions, the rate of decay from an initial state to a final can be calculated from Fermi's golden rule and Einstein's A and B coefficients. Einstein showed that the rate of spontaneous emission, A_{10} is related to the rate of stimulated emission, B_{10} through the equation

$$A = \frac{\hbar\omega^3}{\pi^3 c^3} B_{10} \tag{2.23}$$

where ω is the laser's frequency. Stimulated emission B_{10} can be determined using Fermi's golden rule for coupling to a continuum. The result is that

$$B_{10} = \frac{2\pi e^2}{3\hbar^2} |\langle 1|\mathbf{r}|0\rangle|^2 \tag{2.24}$$

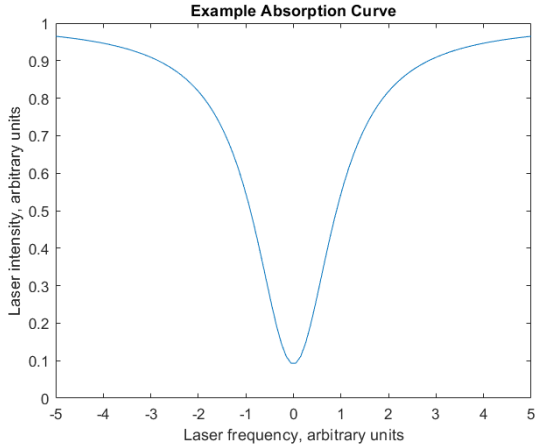

Figure 2.1: Example absorption of a laser by a cloud of atoms.
A laser is shone through a cloud of atoms and its intensity after passing through the cloud is measured. The intensity is shown as a function of frequency.

and therefore

$$A_{10} = \frac{4e^2\omega^3}{3c^3\hbar}|\langle 1|\mathbf{r}|0\rangle|^2 \tag{2.25}$$

where here $\mathbf{r}$ is defined as in Equation 2.7.

For an arbitrary excited state of an atom, there could be many different states to decay to. The total decay rate for a specific excited state is then simply given by the sum over all the various final decay states available to the atom[8]. The lifetime of the state, τ is defined as the inverse of its decay rate.

The Rabi frequency and lifetime set two important time scales for performing operations. Another important scale for the system is the linewidth of the transition, Γ. There is an important connection between the decay rate of a transition and the linewidth. Direct application of the time-energy uncertainty principal leads to the relation that the linewidth is related to the lifetime by $\tau = 1/\Gamma$. The transition linewidth can be understood as follows. Consider an experiment in which one shines a laser at an atom and measures how much of the laser is absorbed for various frequencies. If this is done near a transition frequency, one would see a graph similar to the blue curve shown in Figure 2.1. That is, there is not one frequency that is absorbed but a whole host of frequencies that are absorbed to varying degrees. The degree of spread of this curve is characterized by the full width at half-maximum (FWHM) which is the range of frequencies over which the absorption is half its maximum value or greater. The FWHM is the linewidth of the transition. There

is nothing in principal from preventing two transition being so close together that there is significant overlap of their transition frequencies. The two level approximation thus requires that such is not the case: all other transitions are far enough away in frequency space that there is not any overlap. That is, the separation in frequency units between excited state energy levels is larger than the limewidths of the states. In summary, the three important scales for a two level system are its Rabi frequency, its lifetime, and the linewidth compared to the level spacing. The Rabi frequency is the time scale over which a bit flip can occur, the lifetime is the amount of time information can be stored in an excited state before being lost to decay, and the ratio of the level spacing to linewidth characterizes the appropriateness of using a two level approximation.

The two level system allows a simple model for understanding how an atomic qubit will behave, but if atoms are to be used for quantum computation, the experimenter must have some way of keeping track of each atom. This requires cooling and trapping the atoms before performing any gate operations on them. What follows is a summary of common techniques used to cool and trap atoms.

2.2 Laser Cooling and Trapping

Laser cooling allows clouds of atoms to be reduced to temperatures on the order of micro-Kelvin and lower. Through kinetic theory, there is a correspondence between a thermalized gas' temperature and mean velocity of the particles. Thus, cooling atoms to micro-Kelvin temperature and below corresponds to slowing to relatively low speeds[1]. This is appealing as it allows for precise control of the atoms.

To begin laser cooling a beam of atoms, a simple technique is used. A laser is shone counter-propagating to the atoms with a frequency slightly red-detuned from a fast transition in the atoms. The Doppler shift will cause the laser frequency to be blue shifted in the atoms' frame thereby counteracting the detuning in the lab frame. Based on the mean velocity of the atoms in the beam, one can then choose an appropriate amount of detuning so that the laser is on resonance in the atoms' frame. Consider now a single atom in the beam. The atom is stimulated to an excited state by absorbing a photon from the laser. The photon's momentum is opposite the atoms' and thus causes a decrease in the atom's momentum. When the atom decays, the photon is reemmitted causing an increase to the atoms' momentum of the same magnitude. The cooling comes from the fact that the photons from the laser always impart a momentum change in the same direction, while

[1]For instance, a gas of Cesium atoms at 1 μK would correspond to a mean velocity of about 1 cm/s.

the photons reemitted by the atom decay in any direction randomly thereby having the effect of mostly canceling out in aggregate.

Being slowed down in this way, the atoms will quickly be slowed to the point they are no longer on resonance with the laser. The natural thought is then to adjust the lasers detuning so the atoms are back on resonance. This will cause another small change in velocity before the atoms go off resonance again. The process can then be repeated again and again to appreciably cool the atoms. In practice, this is done by continuously sweeping the frequency of the laser and is known as chirp cooling (in analogy to the fact that a bird's chirp sweeps through frequency). Chirp cooling has the draw back that it takes a continuous stream of atoms and cools them in discrete packets. There is a second method of cooling that uses a static laser frequency known as Zeeman slowing which cools the stream of atoms continuously [20].

In Zeeman slowing, the Doppler shift is again the mechanism responsible for cooling the atoms, but instead of adjusting the laser's frequency as the atoms cool, the atoms' resonance frequency is adjusted. This is done by passing the atoms through a magnetic field while leaving the laser at the desired transition frequency. In the atoms' frame, the light will be blue shifted, but the magnetic field will also increase the frequency needed to drive transitions for $m_l > 0$ states. One can construct the magnetic field in such a way so that as the atoms pass through the field, the amount by which the cooling Doppler shifts the atoms off resonance is exactly compensated for by a decrease in the magnetic field strength. After this large-scale slowing of the atom, there are methods to cool the atoms further such as optical molasses and Sisyphus cooling[20].

The optical molasses technique cools in all three direction simultaneously by crossing three pairs of counter-propagating laser beams orthogonal to each other and red detuning all the lasers from the atomic transition frequency as shown in Figure 2.2. Considering just one pair of counter-propagating lasers, the velocity component in this direction will cause a certain amount of Doppler shift to both lasers beams, red shifting the beam propagating in the same direction and blue shifting the beam propagating opposite. The result is that regardless of the atomic motion, the atoms will always be more on resonance with the lasers that are propagating opposite their motion. This means the rate atoms absorb photons decreasing their momentum is greater than the rate of absorbing photons increasing their momentum, with an overall result that the atoms are slowed. The slowing force is proportional to the atoms velocity and so acts like a drag force, giving rise to the analogy with molasses which is very viscous. There is a fundamental limit to cooling via this technique known as the Doppler limit. Naively, it may seem that the imbalance in the absorption rates will only be balanced once the atoms velocity reaches zero, but fluctuations complicate the matter. As the velocity slows to the point that there is little difference in the

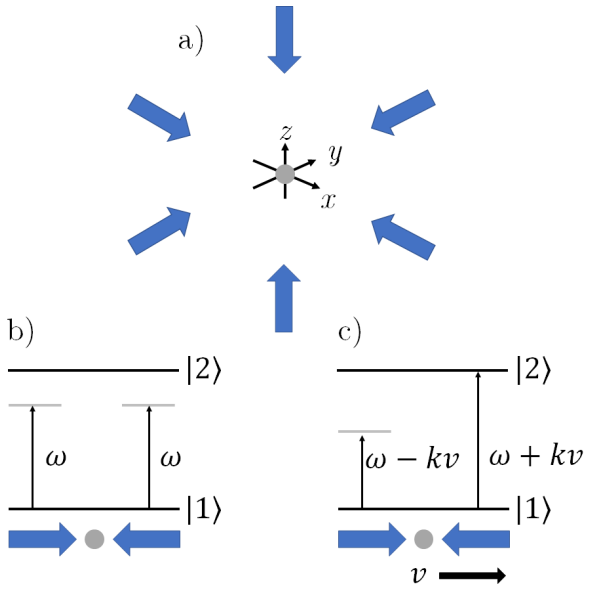

Figure 2.2: Configuration of lasers for optical molasses.
a) The spatial arrangement of the six lasers. b) The detuning of the lasers as seen in the lab frame or by an atom at rest in the lab frame. c) The detuning of the lasers as seen by an atom moving relative to the lab frame. The Doppler shift experienced by a moving atom always causes the laser traveling opposite its motion to be more on resonance. Image adapted from Reference [20].

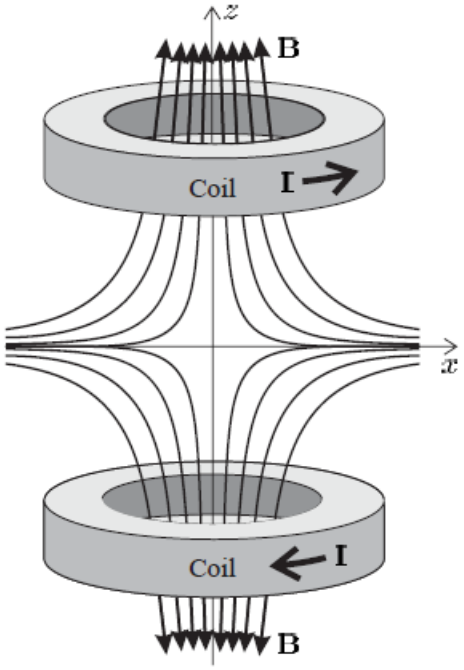

Figure 2.3: Magnetic field from anti-Helmholtz coils.
The field produced by anti-Helmholtz coils is radially symmetric and zero halfway between the coils on the symmetry axis. Image taken from Reference [20].

detuning of the two beams (compared to the thermal energy), the random nature of absorption will lead to the possibility that more photons are absorbed from the red-detuned beam during some periods of time, with the overall result leading to a random walk of the velocity along the laser axis. The Doppler limit for a two level system in optical molasses is given by [20]

$$k_{\mathrm{B}} T_{\mathrm{D}} = \frac{\hbar \Gamma}{2}. \tag{2.26}$$

By adding a pair of anti-Helmholtz coils, and carefully choosing laser polarization, the optical molasses configuration can be turned into a magneto-optical trap (MOT). Such an arrangement is shown in Figure 2.4. Anti-Helmohltz coils are a set of current carrying rings oriented with their symmetry axes aligned and separated by a distance equal to their radius. If the current in both coils has the same handedness, the coils are operating in the Helmholtz configuration, while if they are opposite the coils are operating in the anti-

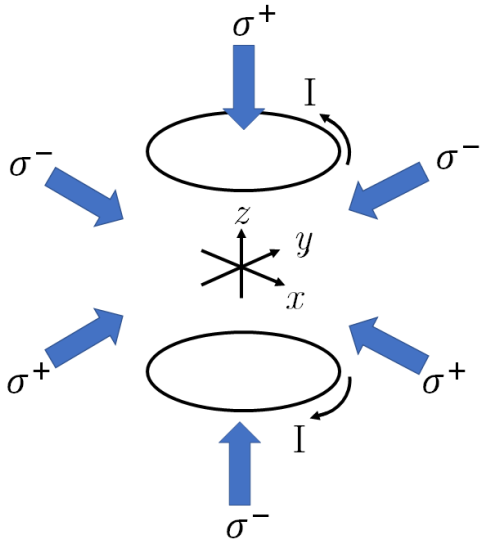

Figure 2.4: Configuration of lasers and coils for a MOT.
Note that while the magnitude of the magnetic field is unchanged through a parity inversion, the direction is reversed. This is why circular polarization of opposite handedness is needed between each of pair of lasers to ensure the correct transition is addressed. Image adapted from Reference [20].

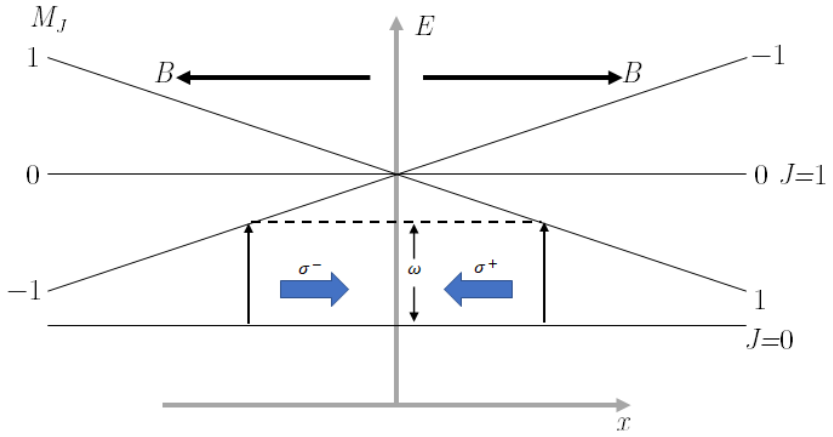

Figure 2.5: Zeeman shift produced in a MOT.
The magnetic field varies approximately linearly near the center of the trap, and therefore so does the Zeeman shift. Circular polarization allows one to select which of the M_J sub-levels the laser will drive to. One can therefore select the polarization that ensures the transition being driven is the one with a negative Zeeman shift irrespective of which side of the trap the atom is on. Image adapted from Reference [20].

Helmholtz configuration. The addition of the anti-Helmholtz coils introduces a magnetic field that varies linearly near the center of the trap across the width of the laser beams and is shown in Figure 2.3. In addition, the magnetic field is radially symmetric about the axis of the coils[20]. Let's consider how this field affects the $J = 1$ manifold of an atom. We begin by aligning the x-axis of our coordinate system with the axis of the coils and defining the origin halfway between the coils. Then, confining our attention to only the x-direction, in the region $x > 0$ the magnetic field will produce a Zeeman shift that is negative for $M_J = +1$ and positive for $M_J = -1$. Since the magnetic field is radially symmetric, in the region $x < 0$ the field has equal magnitude but opposite direction, therefore the $M_J = -1$ state now experiences the negative shift while the $M_J = 1$ state's shift is positive. Since the laser is red-detuned, in the $x > 0$ region the $J = M_J = 0$ to $J = -1, M_J = 1$ transition will be shifted towards resonance. This transition can be preferentially driven by using circularly polarized light of the correct handedness. For $M_J = 0$ to $M_J = -1$ this is σ^- light. In the $x < 0$ region we have the opposite effect; now $M_J = 1$ is shifted closer to resonance so we must use σ^+ light to drive the $M_J = 0$ to $M_J = -1$ transition. By selecting the laser beams' polarizations in this way, we introduce an additional scattering force that is dependent on the strength of the magnetic field. Since within the beam width of the

lasers the magnetic field's gradient varies linearly, the scattering force is proportional to displacement from the center of the coils [20], and so acts as a restoring force much like a spring-mass-damper system from classical mechanics (with damping coming from the optical molasses technique).

Finally, Sisyphus cooling allows for the cooling of atoms below the Doppler limit. In Sisyphus cooling, the atoms travel through a pair of counter-propagating lasers with orthogonal linear polarizations like that shown in figure Figure 2.6.b. This produces a polarization gradient whereby the polarization transitions from linear to negative circular (σ^-) to linear to positive circular (σ^+) back to linear over the course of one wavelength. This polarization gradient has two effects that combine to give Sisyphus cooling. The first is that σ^+ and σ^- light produce an effect known as optical pumping. The polarizations are so named because σ^+ light only allows optical transitions in which $\Delta m = +1$ and similarly σ^- only allows $\Delta m = -1$. For the sake of argument, consider a transition between states with orbital angular momentum $l = 1$ to $l = 2$. If driven by σ^+ light, m will increase by one. The atom will then decay after some time and the magnetic moment is free to change by ± 1 or 0. The result is that σ^+ light will never result in a *decrease* to the magnetic moment quantum number. It is only when the decay causes a $\Delta m = -1$ that the final state is unchanged, while in all other cases the final state will have changed by one or two units of magnetic moment. Over many cycles, the atom will tend towards the $|l = 1, m = 1\rangle$ to $|l = 2, m = 2\rangle$ transition. Similarly, σ^- would tend to cause the atoms to collect into the $|l = 1, m = -1\rangle$ to $|l = 2, m = -2\rangle$ transition.

The second effect that allows Sisyphus cooling is that the light shift is polarization dependent. For red-detuned circularly polarized light, the light shift causes the state being pumped into to have a lower energy level than the other m states. This means there is slightly more energy carried off in each decay than was imparted by the excitation, which over many cycles will result in cooling.

2.3 Bose-Einstein Condensation

The previous techniques allow one to load into a conservative trapping potential where a BEC can be formed. A BEC is a gas of bosons that has been cooled to the point that the bosons' deBroglie waves begin to overlap. This creates an interference effect that adds constructively for bosons, which has the effect of enhancing the overlap. This leads to the wave functions of the bosons settling into a single macroscopic wavefunction. Bose-Einstein condensation was first proposed in the 1920s [17] and experimentally realized in the 1990s [4]. The first BECs were created using rubidium-87 atoms in a magnetic trap

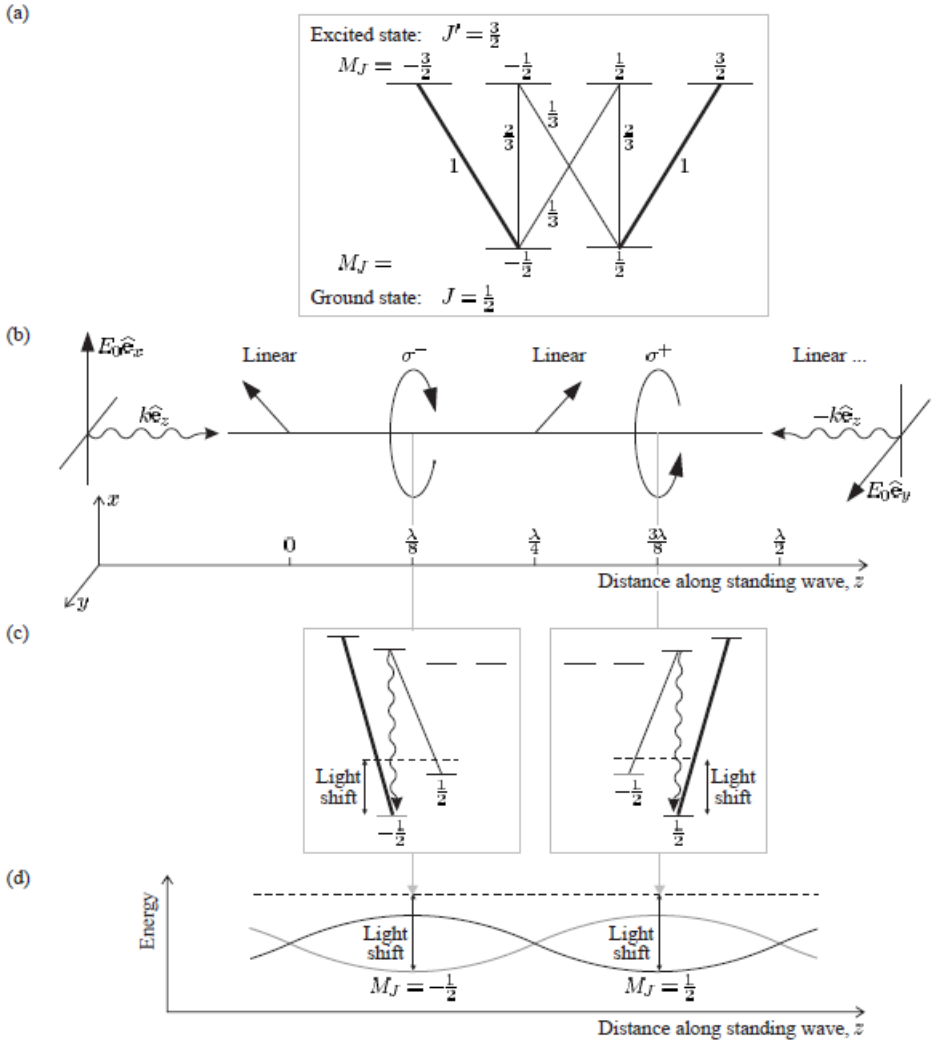

Figure 2.6: Diagram of the sisyphus cooling technique.
a) Level diagram for a $J = 1/2$ to $J' = 3/2$ transition. The fractions next to the lines connecting the ground and excited states denote the relative strength of the transition as compared to the $M_J = \pm 1/2$ to $M_J = \pm 3/2$ transitions. b) Diagram of how the polarization gradient changes along the standing wave. c) Diagrams showing how the energy levels are affected by the light shift for σ^- and σ^+ polarizations. d) Graph showing how the ground state energy levels are shifted as a function of the distance along the standing wave. Image taken from Reference [20].

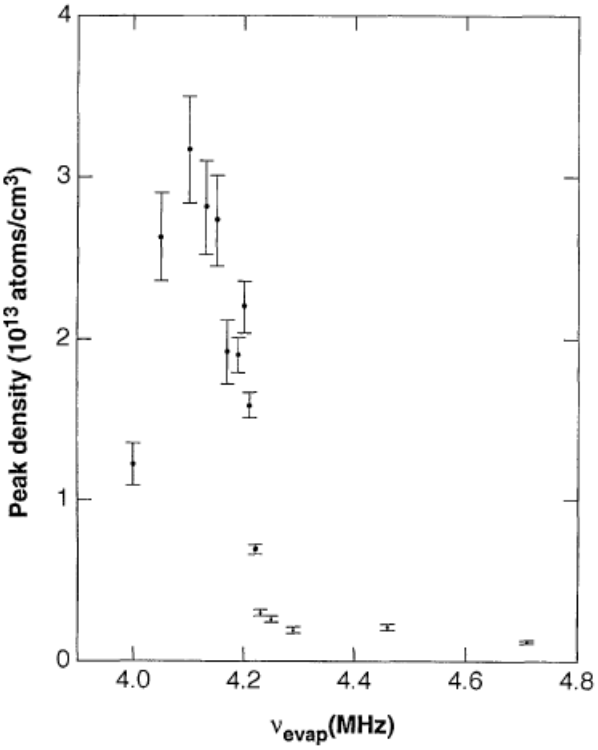

Figure 2.7: Peak density vs. evaporation frequency.
This graph shows the peak density at the center of the sample as a function of the evaporation frequency ν_{evap}. The evaporation frequency is the frequency of an RF pulse used to facilitate evaporative cooling. A higher frequency corresponds to colder atoms being evaporated. The density sharply increases near $\nu_{\text{evap}} = 4.23$ MHz. The density begins to fall afterwards due to ν_{evap} causing atoms in the condensate to evaporate. Image taken from Reference [4].

that was cooled to various temperatures and the density measured. It was found that at 170 nK, a discontinuity was observed in the gas' density, with a large fraction of the atoms collecting near the center of the cloud as the temperature was lowered further. Their graph showing this is reproduced in Figure 2.7. Since density is a thermodynamic quantity, its discontinuity is a strong indication of a phase transition. And since this phase transition occurs as temperature is varied, it is a thermal phase transition.

A quantum phase transition can also be induced in a BEC if it is held in an optical lattice. By tuning the lattice depth, BECs have been shown to exhibit a quantum phase transition from a superfluid to a Mott insulator[23]. This can be seen in Figure 2.8. A quantum phase transition is one that can occur at 0 K. In this instance, it is the interactions that produces the transition. At small depths, the BEC exhibits broad phase coherence across the entirety of the condensate, but as the the lattice depth is tuned past a critical point, phase coherence becomes limited to within each lattice site only. That such a phase transition can be produced in a BEC makes BECs an attractive tool for use in quantum simulation. For instance, related work has allowed for the creation of a cold-atom Fermi-Hubbard antiferomagnet [38]. That the low-temperature Fermi-Hubbard model can be simulated with cold-atoms is advantageous because it is numerically intractable with classical computers. Hence, cold-atoms allow for the exploration of a parameter space inaccessible to classical computers. The Fermi-Hubbard model in the low temperature regime is believed to model essential aspects of high critical temperature superconductors.

2.4 Ultracold Molecules

Ultracold polar molecules offer a potential avenue for quantum computation and simulation. Whereas atoms largely interact through short-ranged contact interactions (which are generally limited to nearest-neighbors interactions), polar molecules benefit from a relatively long-ranged, spatially anisotropic dipolar interaction. When arranged in a lattice, such a system is strongly suggestive of spin-lattice models in condensed matter physics. Furthermore, the previous discussed experiments can also be performed with molecules instead of atoms.

Most notably, dipole interactions between $^{40}K^{87}Rb$ molecules have been used to form a spin-lattice system where spin is coded in the rotational states of the molecules [57]. In this seminal work, spin exchange mediated by the dipolar interaction was observed between molecules in a 3D optical lattice, marking the first time a dipolar interaction between molecules in a lattice was observed. The molecules were loaded into the lattice

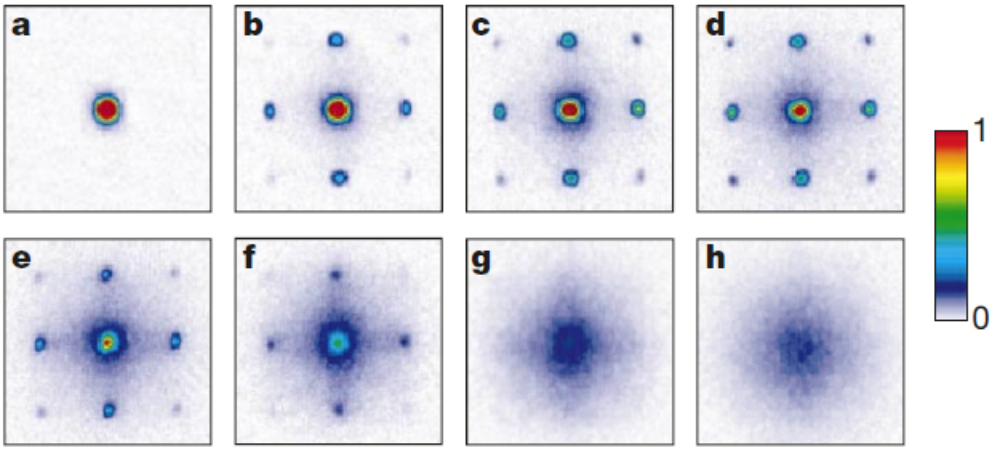

Figure 2.8: Observation of superfluid to Mott-insulator transition.
The panels are organized by increasing trap depth. Panels **a** through **f** exhibit interference between neighboring lattice sites which is lost in panels **g** and **h**. It was found however that turning the depth back down re-acquires the interference pattern. Image taken from Reference [23].

and prepared and probed using microwave pulses. Specifically, the atoms in the $|\downarrow\rangle$ spin state were measured as a function of time using Ramsey interferometry. The Ramsey contrast was found to exhibit an oscillatory character ontop of an overall decay. The decay was measured for different lattice filling fractions and found to be strongly dependent on the density which is a signature of multi-body interactions. The oscillatory character was removed by applying a specific multi-pulse refocusing sequence from nuclear magnetic resonance (NMR) designed to remove dephasing brought on by dipole-dipole interactions. That this pulse was able to remove the oscillation, in addition to the fact that the oscillation frequency matched that predicted from theory, is strong evidence of the dipole-dipole interaction between molecules. In this experiment, filling factors were about 10%. To fully capitalize on the dipolar interaction afforded by molecules, it is desirable to have a higher filling factor. Furthermore, the molecules must be cold enough that the thermal energy is comparable to or lower than the dipolar interaction energy. Both these can be achieved using evaporative cooling, which has recently been demonstrated for KRb molecules [34] and expected to extend to other bi-alkalis. Specifically, we plan to use CsLi molecules, as evaporative cooling depends on dipole-dipole interactions and CsLi has a larger dipole moment than KRb [32].

2.5 Quantum Computing

Quantum computers set themselves apart from the computers we are all familiar with—classical computers—in two distinct ways. The first is the characteristics of how information is stored. With classical computers information is stored in bits. Anything that can take on two discrete and distinct values can serve as a bit e.g. the faces of a coin, whether or not light is being emitted from a light bulb, or the polarity of a magnetic field at a specific region on a hard disc. These states could then be labeled as 0 and 1. Common to all these systems is that the bit will exist in exactly one of the distinct states at any time. In contrast, with quantum computers information is again stored in systems that can take on different states, but these states must exhibit quantum phenomena: superposition, entanglement, et cetera. Some examples of quantum bits (qubits) include the spin states of atoms in a molecule (spin up or spin down) or the polarization of photons (vertical or horizontal). These systems' states are then labeled as $|0\rangle$ and $|1\rangle$. What sets these qubits apart from their classical cousins is that qubits are not restricted to occupying only one of their states at a time. Instead, superposition affords them the possibility to occupy a continuous set of states. For any complex number α such that $|\alpha| < 1$, the state $|\psi\rangle = \alpha|0\rangle + \sqrt{1-\alpha^2}|1\rangle$ is a valid quantum state.

This leads to the second distinction between classical and quantum computers, which is the nature in which the information is processed. Because of classical bits' intrinsic discreteness, the manipulation of multiple strings of bits is limited to logic gates; that is, performing logical operations such as AND and OR on the bits. The quantum behavior afforded by qubits gives rise to processing the information in a distinctly different way. Quantum systems allow the establishment of interference and entanglement between the qubits. Interference could be used, for example, to cause the qubits to only exist in the superposition of numbers that factor the input number [2].

The final readout of information is also different between classical and quantum. It might seem that superposition could allow an immense speed-up over classical computers because the qubits could store multiple pieces of information at the same time. And while in a sense that is true, problems arise when one goes to read the stored data. Wavefunction collapse will cause the qubits to take on one of their superposed states randomly. The user therefore cannot gain access to all of the information contained in a quantum system, generally.

Nonetheless, quantum computers still offer advantages over classical computers that make them worth pursuing. Notably, there are known algorithms for quantum computers

[2] In fact, this idea lies behind Shor's factoring algorithm [50].

that would allow for factoring large numbers [50] and searching [25] in fewer operations than required by classical computers. Quantum computers are also a natural choice for simulating quantum systems. Quantum simulation is the technique of taking a quantum system that is insoluble with traditional means (i.e. hand calculations and classical computer simulations) and creating a system with analogous effects. The utility is that the analog system is chosen to afford the researcher with much more control than would be had in the original system. In this way, one can set up the analogous system as needed and observe how it evolves in time, or induce changes in it as desired to study how the system behaves under different conditions. By creating this analogous system, one arrives at the solution to the original system's behavior by simply measuring the system at some time. Quantum simulations could help to solve some pressing problems of our time. For instance, fertilizer production requires ammonia, which is usually synthesized from nitrogen. This is done through a reaction that requires a great deal of heat i.e. energy. It is known that ammonia is produced at room temperature by certain bacteria, but their mechanism is unknown. Quantum computers could aid in studying how the bacteria produce ammonia [36].

2.5.1 Computational Complexity

It was mentioned in the previous section that algorithms are known that would allow quantum computers to factor large numbers and search with fewer operations. As it stands however, a classical computer or even pen and paper can out perform the leading quantum computer's ability to factor. It is therefore worth a brief discussion of computational complexity to clarify this point.

In computational complexity theory, problems are grouped by how the amount of resources needed by a computer to solve the problem grows as the input to the problem grows. For instance, if the number being factored grows from having 4 digits to 8 digits, does the number of needed resources double, increase by ln(2) or something else? From a computational complexity point of view, the simplest problems are those whose resources grow as a polynomial function of the size of the input. This group is called polynomial or P for short. On the other extreme are problems whose resources scale exponentially with the input. The short hand EXP denotes the group of algorithms whose complexity's upper bound scales exponentially with the input. Factoring algorithms fall into the complexity class non-deterministic polynomial (NP). These are problems where the resources required to verify a solution scales as a polynomial to the input but the resources to find a solution scale by more than a polynomial. The set of problems considered easy for a quantum computer are called bounded quantum polynomial (BQP) and is the class of problems for

which a quantum computer's needed resources scale polynomially with the input. With a quantum computer, factoring falls into the class BQP and so is expected for large numbers to be more easily performed with a quantum computer than a classical computer.

2.5.2 DiVincenzo Criteria

Since there are still many platforms being explored for quantum computing, a set of criteria has been developed to help distinguish what is needed for a system to be a viable platform for quantum computing. They are called the DiVincenzo criteria, named after their inventor David P. DiVincenzo [16]. The five criteria are as follows.

1. **A scalable system with well characterized qubits**. Scalability is an important challenge facing every platform, for as more qubits are introduced to the system, the number of ways a qubit can incorrectly entangle with the other qubits grows exponentially. That the qubits are well characterized means that, for instance, if one is using a two level approximation, the qubit must remain in those two levels only.

2. **The ability to bring the system to an initial fiducial state**. Quantum algorithms require the system to begin in a specific initial configuration. Therefore, a working quantum computer must be able to bring the qubits into this configuration.

3. **A universal set of gates**. A universal set of gates means that there is a small set of gates the quantum computer can perform, and this set of gates can be combined in such a way as to create any arbitrary quantum gate needed. A universal set can be made a number of different ways [42], but at minimum requires two single qubit operations and one "entangling" i.e. two-qubit operation [36].

4. **A qubit specific measurement system**. The measurement must be able to measure each qubit individually in order to read out the number stored by the qubits.

5. **Long relevant decoherence times**. The decoherence must be long as compared to the gate time. If the qubits' entanglement were to be lost before all the gates in an algorithm could finish, the algorithm would not produce the correct results, and so the computer would be rendered ineffective.

2.5.3 Quantum Computing with Molecules

Molecules are an untapped experimental avenue for quantum computing, but they afford some useful characteristics. First, like Rydberg atoms (a leading platform for quantum

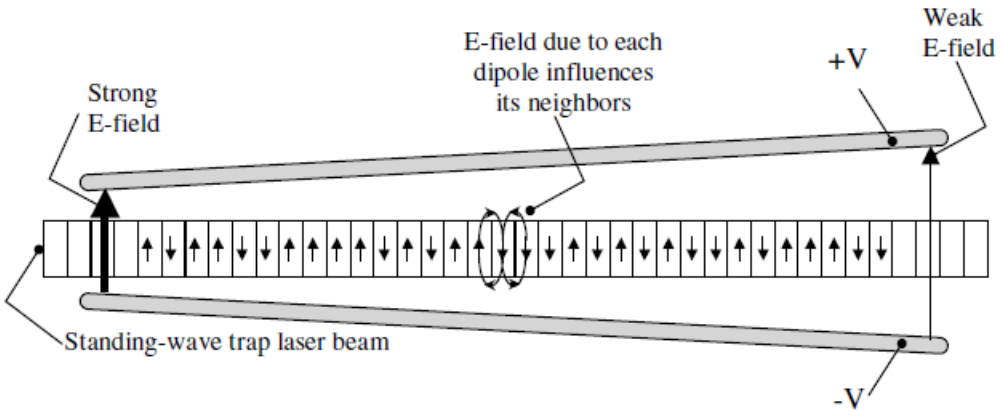

Figure 2.9: Schematic of a method to perform quantum computing with molecules. Molecules are held in an optical lattice and oriented using an electric field. The electric field varies along the optical lattice so that the Stark shift is different for each molecule. Image taken from Reference [14].

computation currently) molecules have dipole moments that are state dependent: one can then turn interactions between molecules on and off by exciting qubits to a highly dipolar state as needed. Further, as compared to Rydberg atoms, molecules have states with much longer lived lifetimes, up to seconds for molecules as compared to 100s of μs for Rydberg atoms. Molecules are therefore expected to perform favorably in comparison with Rydberg atom computing as will be explored in Chapter 5.

While Chapter 5 introduces a new method of performing quantum computing, the idea of using molecules for quantum computing itself is not new. In 2002 a scheme was published for using molecules as qubits. In this scheme, the ease of polarizing molecules is used to allow the user to easily address the molecules individually via a stark shift. A diagram of the method is shown in Figure 2.9. The electric field serves to orient the molecules so that information can be encoded via the molecule's orientation (aligned or anti-aligned with the field) while the electric field gradient shifts the energy levels compared to neighboring qubits, making each molecule individually addressable. This scheme relies on the superfluid to Mott-insulator transition in BECs to achieve unity filling, which the paper notes it is unknown how effectively this would work for molecules, but speculates that it would be favorable since the interactions between polarized molecules is many orders of magnitudes stronger than neutral atoms.

2.6 Summary

Quantum computers offer the potential for more efficiently solving certain problems than classical computers, and molecules offer the potential for more efficiently performing quantum computation, as will be explored in Chapter 5. Molecules can be made and precisely controlled through techniques such as those discussed here. We will make CsLi molecules, and so this requires a separate source of atoms for each species, as well as a chamber to trap and cool them before being combined into molecules. The apparatus for performing these tasks will be discussed in the next chapter.

Chapter 3

Towards Laser-Cooling Cesium

The previous chapter focused on the theory of laser cooling atoms and some landmark experiments that have been achieved with these techniques. This chapter focuses on how these techniques will be implemented in the lab. Specifically, the techniques of the previous chapter must be carried out in ultra high vacuum and hence require a vacuum chamber. In addition, to perform cooling, Rabi oscillations, and other such tasks necessary for quantum computing, lasers must be precisely locked to the desired frequencies and efficiently distributed throughout the lab. We begin with a discussion of the new vacuum chamber's design, followed by the techniques used for locking and distributing lasers.

3.0.1 Dimensioning and Vacuum Standards

In this and the next chapter, a great deal of dimensions will be given, not all in the international system of units (SI). Dimensions are instead given in their native unit system. That is, if a part was drawn and made using inches, the dimension will be given in inches. Because both United States customary (USC) and metric units will be used, American Society of Mechanical Engineers (ASME) standard Y14.5 1.6.2(a) will be followed in which lengths in inches less than one inch will not have a leading zero before the decimal point, while lengths in millimeters less than one millimeter will have a leading zero[2].

Vacuum systems have also developed standards, specifically revolving around the shapes of the flanges used. There are several common flange designs, but for achieving UHV, the standard ConFlat (CF) design must be used. CF flanges use a unique gasket material compared to other flange standards. When joining two vacuum flanges together, regardless of the standard used, a gasket must be placed between the flanges to help seal the chamber.

Rather than using rubber or plastic as their gasket, CF flanges use a soft metal, typically copper. The flanges have sharp edges that can dig into the soft metal gasket and create a seal that can hold much lower vacuum than rubber.

CF flanges come in a variety of sizes, and are specified either by the flange's nominal outer diameter (OD) in inches followed by the letters CF, or the flange's inner diameter (ID) in millimeters preceded by the letters DN. This thesis will refer exclusively to CF flange sizes using the inch sizes.

3.1 The Experimental Apparatus

Figure 3.1 shows the apparatus that will be used to perform experiments involving molecules in the lab. The apparatus is a vacuum chamber that can be understood as 4 separate sections: 2 ovens (which are identical), the two-dimensional magneto-optical trap (2D MOT) chamber, and the main chamber. Atomic beams are produced from the ovens and trapped in the 2D MOT before being pushed into the main chamber where experiments are performed. There are two identical ovens on the apparatus so that each can be loaded with a different element, specifically, one with lithium and the other cesium.

Lithium and cesium have been chosen for the large dipole moment that is produced when combined into a molecule—the largest of all bi-alkalis [32]. But there are other qualities that make them favorable as well. Lithium alone has shown much success for its use in quantum simulation of the Fermi-Hubbard model [38] and both species have strong Feshbach resonances both individually and for use in forming molecules. Additionally, the two atomic species have very different wavelengths and so can easily be independently controlled.

3.1.1 The Oven

The oven in our experiments is unorthodox, and a detailed discussion of its design is delayed until Chapter 4. Broadly, the oven consists of a crucible housed within a vacuum chamber as shown in Figure 3.2. The crucible is loaded with a chunk of the desired element and brought to a high enough temperature to form an atomic vapor. This vapor effuses from a nozzle on the front of the crucible forming an atomic beam which then passes through a Zeeman-slower tube.

A Zeeman slower tube is a nipple that has been wrapped with a coil of wires in a

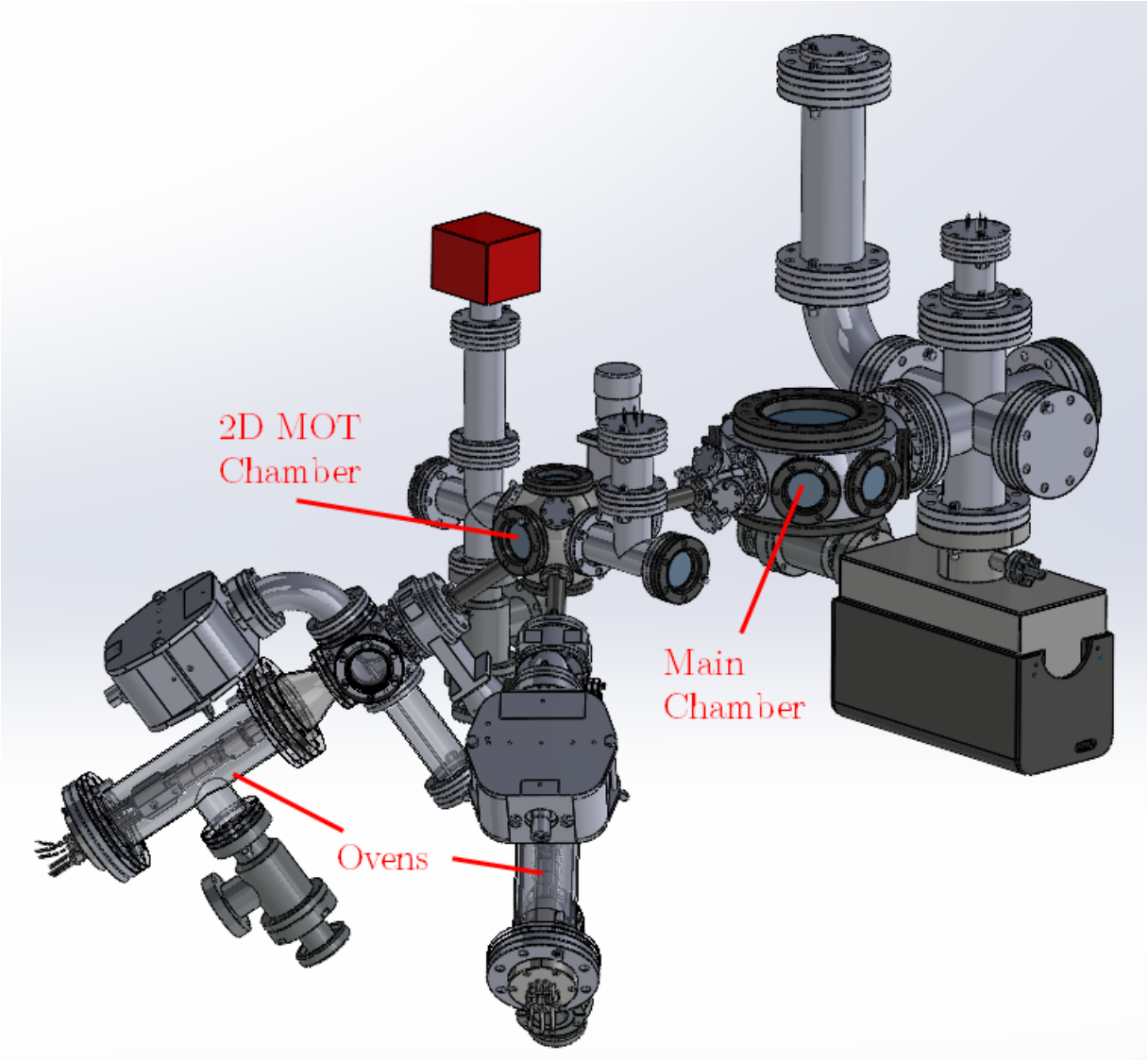

Figure 3.1: Computer aided design (CAD) model of the experimental apparatus. The vacuum chamber is made of three main sections: the ovens, the 2D MOT chamber, and the main chamber. Atomic beams are produced from the ovens and trapped in the 2D MOT before being pushed into the main chamber where experiments are performed.

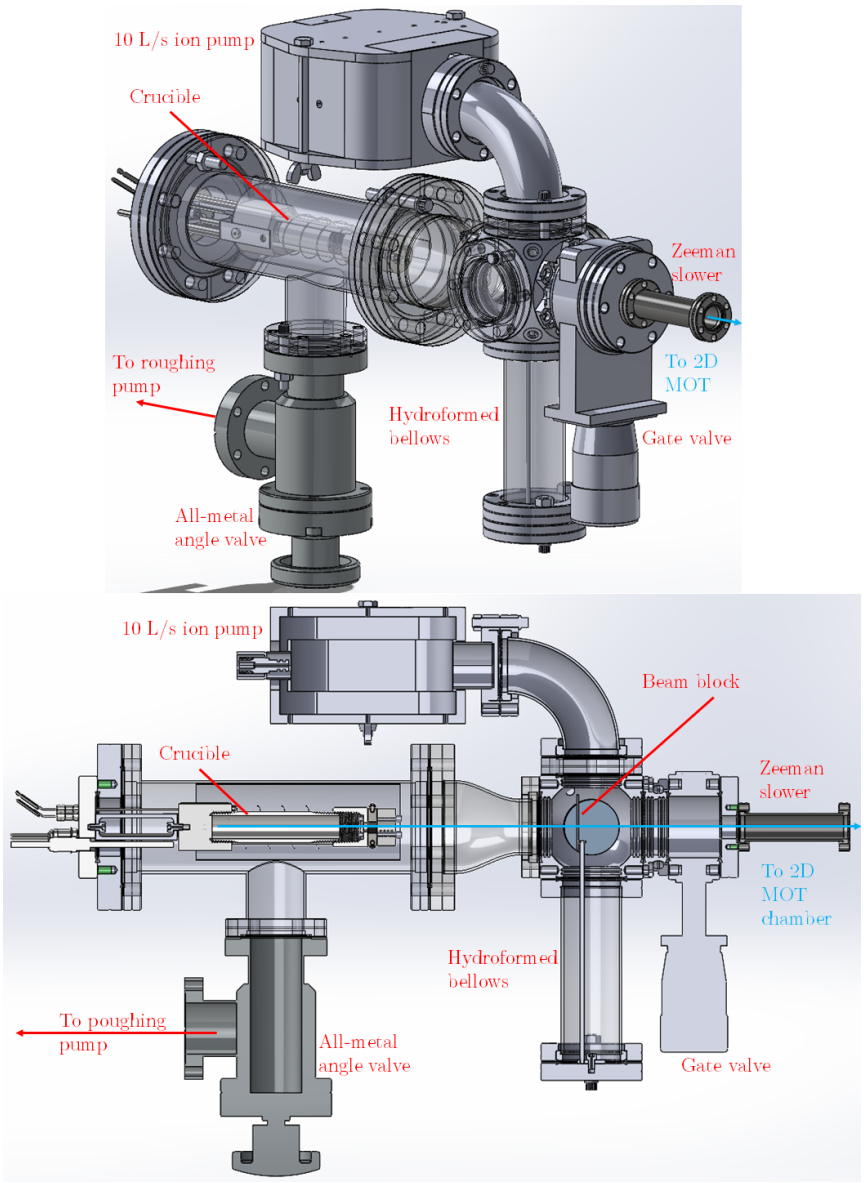

Figure 3.2: Trimetric and cross section views of the oven assembly.
Top: trimetric view. **Bottom:** cross section. The oven consists of the crucible, a 10 L/s ion pump, an angle valve for connecting to a rough pump when initially evacuating the chamber, a beam block that can be moved in front of the beam to stop its flow from reaching the 2D MOT when needed, a gate valve to allow ioslating the oven from the rest of the chamber when in need of servicing, and a Zeeman slower.

precise arrangement[1]. Current may be passed through the wire to form a magnetic field which produces a Zeeman shift in the atoms' energy levels. The laser's frequency is tuned to be on resonance with the transition between one of these shifted levels and the ground state as the atoms leave the oven. However, the atoms leave the oven at a temperature of several hundred degrees Celsius, resulting in an average velocity of several hundreds of meters-per-second directed towards the beam. For the laser light to be on resonance with the atoms it must be corrected for the Doppler shift the atoms will experience. Accounting for this, the atoms will absorb photons from the laser resulting in a change of momentum opposite their direction of motion. When the atoms decay, the photons are reemitted with no preference for direction and so in aggregate do not appreciably change the momentum. As the atoms slow, they experience a new Doppler shifted frequency and would no longer be on resonance with the laser if the magnetic field in the nipple were uniform. The number of turns of wire on the nipple is therefore varied in a precise way so that the Zeeman splitting along the nipple varies in such a way as to keep the laser on resonance with the slowed atoms. At the end of the Zeeman slower, the slowed atoms are predicted to have a velocity near 25 m/s [27] and pass into the 2D MOT chamber assembly.

3.1.2 The Two Dimensional Magneto-Optical Trap Chamber

After exiting the Zeeman slower, the atoms enter the 2D MOT chamber. This chamber serves as a staging area to collect atoms before moving them into the main chamber to perform experiments. Our design for the realization of a MOT is shown in Figure 3.3. The cross-sectional view shows the arrangement of the lasers needed to form the optical part of the trap. Not shown in the figures are the coils needed to produce the 2D-quadrupole magnetic field for the trap. Space has been left above, below, and to the sides of the chamber to allow access for magnetic coils. On either side of the chamber are additional vacuum fittings whose purpose is to facilitate maintaining UHV in the chamber. On the left is a four way cross. The through way allows the laser access to the chamber, while the branches allow for the fitting of a combination NEG+ion pump on top and an angle valve on bottom for connecting to a roughing pump for initial evacuating. On the right is a tee whose branch contains an ion gauge for monitoring the pressure near the chamber. On the back of the chamber is a gate valve that can be closed to isolate the 2D MOT from the rest of the system when servicing is needed. On the front of the chamber is a viewport which allows a fifth laser beam acccess to the chamber. The laser is used to push the trapped atoms into the main chamber.

[1]This is covered in Omar Ali's thesis [27].

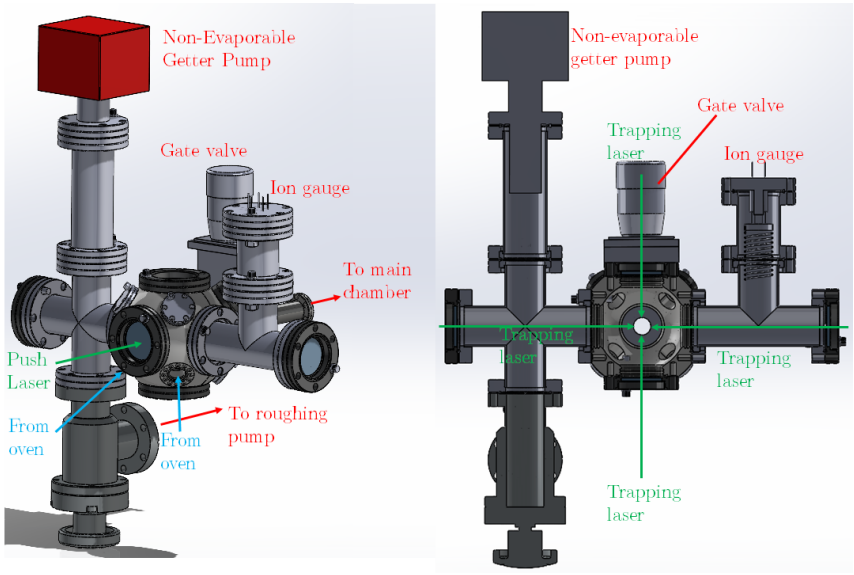

Figure 3.3: Trimetric and cross section view of the 2D MOT chamber assembly. **Left:** trimetric view **Right:** cross section. The cross and tee fittings on either side of the chamber are to facilitate maintaining high vacuum. The 4-way cross has a non-evaporable getter (NEG) on top and all-metal angle valve for attaching to a rough pump for initial pumping. The cross on the right is fitted with an ion gauge to measure pressure.

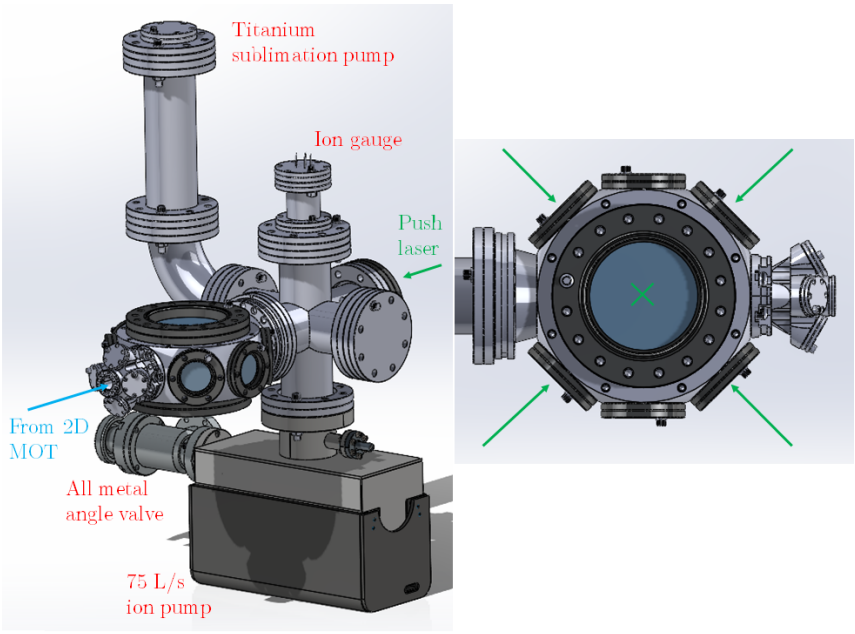

Figure 3.4: Trimetric and top-down view of the main chamber assembly. **Left:** front view. The main chamber is surrounded with many viewports to allow as much optical access as possible to the atoms and molecules. The 6-way cross serves to facilitate maintaining UHV by allowing the attachment of a titanium sublimation (Ti:Sub) pump, 75 L/s ion pump, and ion gauge. The ion pump is fitted with an all-metal angle valve to allow for rough pumping when initially evacuating the chamber. **Right:** top-down view showing viewports used for trapping. The green arrows denote trapping lasers in the plane, while the green cross denotes a trapping laser going into the page. There is also a sixth laser not shown entering from the bottom of the chamber.

3.1.3 The Main Chamber

The laser used to push the atoms into the main chamber cannot also pull the atoms, so a second pushing laser is needed in the main chamber to slow the atoms back down. This is shown in Figure 3.4. In addition, the cross section shows the trapping lasers and the push lasers which are depicted as a green dot.

In addition to the viewports being shown used for trapping, there are 4 more viewports that allow additional access to the lattice as needed. Backing the main chamber is a 6-way cross which is attached with an ion pump, Ti:Sub pump, and ion gauge to allow for maintaining UHV. The final fitting of the cross is currently fitted with a blank to allow for

the possibility of future expansion. At the front of the chamber is a 5-port multiplexer. The multiplexer converts the single $2^3/_4$ CF port into five $1^1/_3$ CF ports. Currently, only the center port is in use, but the 4 surrounding ports allow for the option of future expansion e.g. to feed microwave antennae into the chamber.

Because this vacuum chamber is to be used for experimental physics work, one cannot say with any certainty how exactly experiments will be performed over the lifetime of the oven. It has therefore been designed to afford as much optical access to the main chamber as possible. To this end, all the viewports have been coated with a broadband anti-reflection coating that extends from 650nm to 1100nm. This range is chosen because lithium is resonant with about 671 nm light while cesium is resonant with 852 nm light. Optical lattices can vary in size, and so the additional coating further in the IR allows for longer wavelength optical lattice beams to enter the chamber efficiently.

Currently, the plan is to use the diagonal viewport entrances for all the trapping lights, which include a 3D MOT, optical dipole trap (ODT), and 3D optical lattice. The reason for using the diagonal viewports for trapping is to allow for future expansion. A glass cell is planned to be added in the future, and this would be best placed perpendicular to the atomic beam to afford the most room for optical access to the cell. The top and bottom viewports are the largest ports on the assembly at 6 inches nominal in diameter. The shape of the chamber also places these viewports closer to the center than any of the other viewports. This is great for imaging, as a large lens can be placed very near the sample to afford a large numerical aperture. For a two inch lens, the largest numerical aperture is 0.54 for a lens directly on the viewport.

3.1.4 Fluid Flow, Chamber Pressures, and Pumping

As pressures drops from 1 atmosphere to the UHV range, the nature of flow changes in a fundamental way. For concreteness, consider a fluid flowing down a long cylindrical tube with diameter d (and because the tube is long we assume its length $l \gg d$). For high pressure flows, the mean free path λ of the atoms and molecules is very short—much shorter than d. This means the particles are much more likely to collide amongst themselves than with the tube. This regime of flow is termed bulk flow, continuum flow, or hydrodynamic flow. But as pressure drops, the mean free path increases. Eventually, the mean free path will become comparable to d and beyond. Once $\lambda \gg d$, we have entered a fundamentally different flow regime termed free streaming or molecular flow. The flow regime is quantified by the Knudsen number, Kn, which is the ratio of the particles' mean

free path to a characteristic length scale of the system (d for our purposes):

$$\mathrm{Kn} = \frac{\lambda}{d}. \tag{3.1}$$

The continuum flow regime is defined to be fluids with $\mathrm{Kn} < 0.01$ while molecular flow is for fluids with $\mathrm{Kn} > 1$.

The molecular flow regime is needed to ensure the atoms leaving the crucible will reach the 2D MOT without collisions. Collisions would allow atoms to exchange momentum outside of the experimenter's control, rendering laser cooling ineffective. Put another way, the mean free path of the atoms leaving the crucible must be longer than the distance they must travel to reach the 2D MOT.

The pressure in the 2D MOT chamber is bounded on both sides by the oven and main chamber. The oven will have a pressure near 10^{-8} torr due to the high temperature of the crucible and large flux of atoms leaving it. The main chamber is targeted to operate at 10^{-11} torr. In order to support such a large pressure differential, we look to keep the 2D MOT chamber in between these pressures, i.e. near 10^{-9} torr. This can be achieved by assuring a small conductance between the oven and 2D MOT chamber, as well as between the 2D MOT chamber and main chamber.

To see this we begin by noting that conductance is defined as

$$C = \frac{Q}{P_1 - P_2} \tag{3.2}$$

where C is the conductance, Q is the throughput, and P_1 and P_2 are the pressures at the high and low pressure sides of the tube respectively. Throughput is the quantity of fluid passing a plane in a given time, $Q = d/dt(PV)$, and so conductance is a measure of how easily flow is driven through a pipe. Consider two pipes of equal length but different conductances. If both pipes are transporting fluid at the same throughput, from Equation 3.2 we can see this means the lower conductance pipe will have a higher pressure differential, i.e. requiring more work than the lower conductance pipe to drive the same flow.

For air at 20°C, the conductance of long round tubes in the molecular flow regime is approximately

$$C = (121 \frac{\mathrm{L}}{\mathrm{s\ m^2}}) \frac{d^3}{l} \tag{3.3}$$

where d and l are the diameter and length of the tube respective, both in meters, and the conductance is in L/s [43]. That the conductance scales with the tube's diameter makes sense, as throughput is a measure of fluid passing a boundary, and enlarging d will enlarge

this boundary and hence the throughput. Because we want to support a large pressure differential between the chambers, we want a small conductance. From Equation 3.3 we can see this drives our design of the tubes connecting the chamber, as we would like to make their diameters as small as possible. We have therefore chosen to use the smallest diameter CF nipples commonly available from suppliers which is a $1^1/_3$ CF nipple having in inner diameter of .65 inches.

The pumps for each chamber have been chosen to reach the required pressure targets. Based on previous experience, in the oven a small ion pump is expected to be all that is needed to reach 10^{-8} torr. If the pressure is found to be consistently higher, the ion pump can be replaced with a combination NEG+ion pump. In the 2D MOT chamber, the lower pressure requires a NEG pump in addition to the ion pump. It is worth taking a moment to discuss how these pumps work.

Ion pumps have a cathode and anode that electrons stream between and collide with passing atoms and molecules. The collision causes the atom or molecule to become ionized and therefore attracted to the cathode. The ion's collision with the cathode removes the ion from streaming throughout the chamber and so it has been "pumped".

Hydrogen is not well pumped by ion pumps both because it is difficult to ionize and because it has high mobility due to its small size which makes it hard to bury in the cathode. This can be overcome with a getter pump. A getter is a material that gas particles will adsorb to. Getter material can either be evaporated to coat the interior walls of the vacuum chamber, or left as a bulk solid that particles first adsorb to then diffuse inward. The latter are called non-evaporable getters to distinguish them from those that do evaporate. When initially evacuating the chamber, NEG pumps must be "activated" for their exposure to atmosphere will have caused enough adsorption to saturate the getter. After pumping down the chamber, the NEG is activated by bringing it to a high temperature for an extended period to allow the adsorbed particles to diffuse inward (500°C for 1 hour for our pump). The NexTorr Z100 pump in the 2D MOT chamber has an ion pump that can pump at 6 L/s and a getter that can pump H_2 at a rate of 150 L/s. The ion pump's speed has been matched to the conductance of the pipes it is fitted to, which are estimated to have a conductance of about 5.5 L/s. This was estimated using the equation

$$C_{\text{total}}^{-1} = C_{\text{aperture}}^{-1} + C_{\text{tube}}^{-1} \tag{3.4}$$

where C_{tube} is given by Equation 3.3 and C_{aperture} is

$$C_{\text{aperture}} = 29\pi d^2. \tag{3.5}$$

where d is the same as in Equation 3.3 and C_{aperture} is in L/s. That is, the conductance of the cross in which the NEG rests was estimated to be the conductance of an aperture

in series with the conductance of a long pipe[2]. The length for l was taken to be half the length of the cross (i.e. from where the NEG rests to the midpoint of the cross).

When selecting ion pumps, one must match the pump rate with the conductance, for if the pumping rate is lower, a faster pump could more effectively pump down the chamber, while if the pump rate is much higher it is inefficient because the conductance will limit the rate of pumping.

The main chamber is pumped using a 75 L/s ion pump, and a Ti:Sub pump. While the viewports surrounding the main chamber are 2¾ CF fittings, the port the cross and pump are attached to is a 4½ CF fitting. The larger diameter is intended to facilitate pumping, as it allows for a higher conductance which has been estimated to be about 80 L/s thereby optimally matching the pump's speed to the chamber's conductance. This is why the main chamber has such a large port on the back of it: the larger diameter allows for a higher conductance and so better pumping.

The Ti:Sub pump in the main chamber is an evaporable getter that is used to better remove hydrogen from the system. A Ti:Sub pump contains a filament of titanium that, in high vacuum, will sublimate when a current is passed through it. The titanium vapor will then deposit on the interior of the vacuum chamber, coating it in a surface that is very sticky to the gases in the chamber. When particles strike the titanium coated surfaces, they are much more likely to adsorb to it than steel. The more surface that is coated, the more chance of adsorbing particles. For this reason, the Ti:Sub in the main chamber is placed in a 4½ CF nipple rather than the 2¾ CF fittings more commonly used throughout the chamber. This is also part of the reason a Ti:Sub is *not* used in the 2D MOT chamber: it would take up too much room. Both because it would require a larger diameter nipple, and because it would require its own access to the chamber separate from the ion pump. By using a combination NEG+ion pump, a two fold space saving is afforded by reducing the number of access points needed on the chamber, and minimizing the size of the nipples using these access points.

3.2 Saturated Absorption and Frequency Modulation Spectroscopy

All the cooling and trapping techniques discussed in Chapter 2, most of which will be carried out in the vacuum chamber, rely on lasers being precisely tuned to a transition

[2]That conductances in series add as in Equation 3.4 can be seen from Equation 3.2 by recognizing that the throughput must be the same for the aperture and pipe.

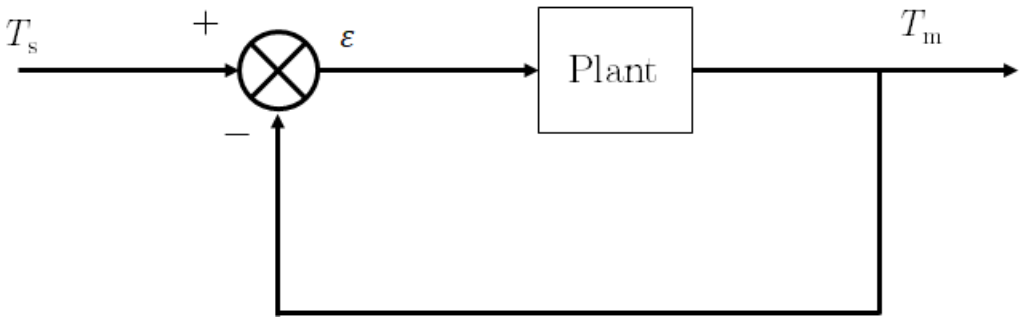

Figure 3.5: Prototypical closed-loop feedback control system.
The plant represents the portion of the system the designer wishes to control but whose characteristics the designer cannot easily change. T_S denotes the desired value for the controlled variable, T_m the variable's present value, and $\varepsilon = T_S - T_m$.

frequency of the atom it is interacting with (e.g. 671 nm for Doppler cooling lithium or 852 nm for cesium). Setting a laser to the proper frequency however is not as simple as merely setting a dial to the correct number. Instead the laser must be locked to a transition frequency using a control loop. A control loop is depicted schematically in Figure 3.5. A simple example of a thermostat will serve to demonstrate how control loops work. Suppose it is a particularly hot day and 28°C inside. To cool down, the user sets the thermostat to 22°C. The thermostat then uses the difference between the current temperature and the desired temperature, called the error signal, to determine how hard to work. Initially the difference is $22°C - 28°C = -6°C$ so the thermostat needs to run moderately strongly and in a way that decreases the current temperature (decrease because the error signal is negative). This causes the temperature to fall quickly, say by 3°C, resulting in a new error signal of −3°C. Now the thermostat will begin cooling the air less aggressively. This produces a smaller change, 2°C say, resulting in an error signal of −1°C so the thermostat begins working very gently. This cycle continues and has the effect of causing the system to eventually settle into a stable steady state near the set value[3]. This process is known as closed-loop negative feedback.

Saturated absorption spectroscopy provides a means of generating an error signal that may be used as part of a control system to lock the laser frequency. For concreteness,

[3]Depending on the system in question, there can be a small amount of steady state error that persists between the set value and true value. It is also not necessarily the case that a negative error signal results in a stable system, but such details are beyond the scope of this thesis. The interested reader is directed to an introductory text on automatic control such as Reference [40].

the current discussion will focus on spectroscopy with cesium with the understanding that the techniques apply equally well to other atomic species. Figure 3.6 shows a breadboard designed by the author for performing saturated absorption spectroscopy. Following the laser paths shown in the schematic, after exiting the fiber optic cable, the laser passes through a half-wave plate and into a polarizing beam splitter. Together, the half-wave plate and beam splitter can be used to control how much of the beam is reflected down the probe pathway (shown in blue) and how much is transmitted through to the pump pathway (shown in red). This is because the laser exiting the fiber is linearly polarized and the half-wave plate has the effect of rotating the laser's polarization by an amount dependent on the orientation of the wave plate. In other words, rotating the half wave plate also rotates the laser's polarization axis. The beam splitter then transmits the portion of the laser whose polarization is horizontal while reflecting the polarization that is vertical. Therefore the pump laser light is horizontally polarized while the probe light is vertically polarized.

The purpose of the pump can be better understood by first considering what would happen without it. This would correspond to absorption spectroscopy. Then the probe beam simply passes through the vapor cell and into the photodiode (the electro-optic modulator (EOM) can be disregarded for the time being as it is only needed for frequency modulation (FM) spectroscopy). Without the pump beam, all the atoms are in the ground state and so sweeping the laser's frequency will register a resonance at the vapor's transition frequency. Graphing the laser's power over time, this would be seen as a dip as more of the laser power is absorbed near resonance. However, the vapor cell is at room temperature so the spread of velocity of the cesium atoms in the vapor cell is a few hundreds of meters per second. This results in the resonance's width being broadened far beyond its natural width. The resulting broadened curve is known as the Doppler feature or Doppler profile and is shown in Figure 3.7. This is where the pump beam becomes useful.

The pump beam's power is stronger than the probe and near the saturation intensity of the vapor. The pump enters the vapor cell opposite the probe. The two laser beams are aligned to overlap, but because they enter from opposite sides, they propagate in opposite directions. This means an atom with non-zero velocity will experience opposite Doppler shifts in the two beams. The frequency of the beam propagating in the same direction will be shifted by $-kv$ where k is the laser's wave vector and v is the atom's component of velocity in the direction of the laser. On the other hand, the frequency of the beam propagating opposite the atom will be shifted by $+kv$. However, if and only if the atom has near-zero velocity, it will see both laser beams at near the same frequency. This has two consequences. The first is that the probe's interaction with near-zero velocity atoms will be altered by the pump's simultaneous interaction with these atoms. For non-zero velocity

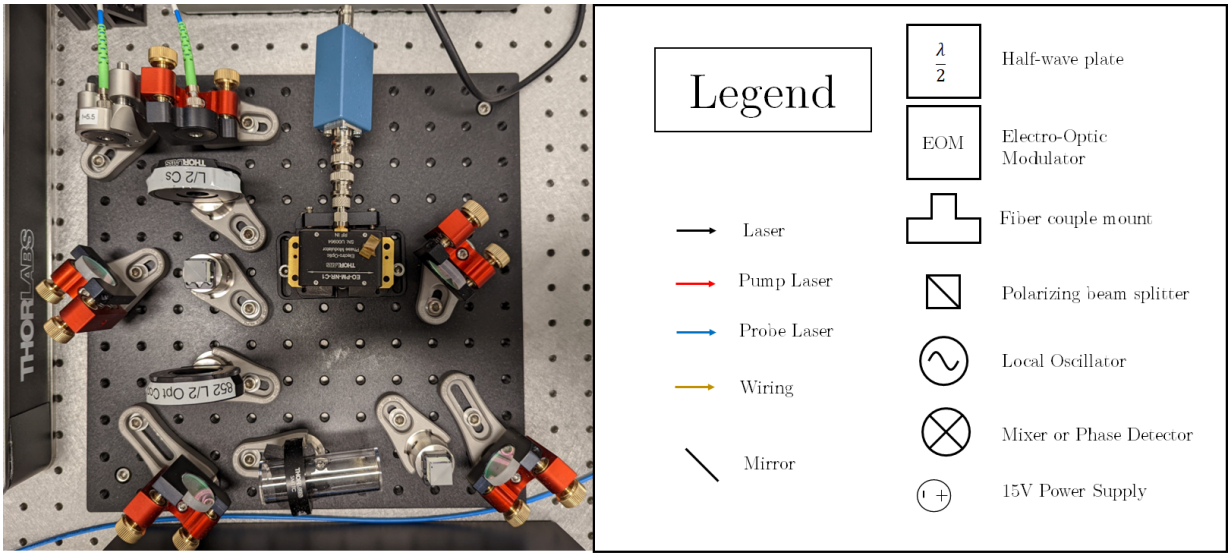

Figure 3.6: Saturated absorption and FM spectroscopy optical breadboard. **Bottom**: schematic representation of the breadboard. The pump and probe beams are shown side by side for clarity, but in an actual board the two beams must be overlapped when passing through the vapor cell. **Top right:** legend for the Schematic. **Top left**: a typical breadboard used in the lab for saturated absorption spectroscopy and FM spectroscopy.

atoms, the Doppler shift will lead to the probe's interaction being unaltered by the pump as the pump will be $2kv$ off resonance with the atoms Doppler shifted on resonance with the probe. This leads to the second consequence that, as the frequency is swept, the zero-velocity class atoms will not be able to absorb as much of the probe beam as before. This is because the pump beam saturates the transition, "burning a hole" for the probe to pass through. That is, since the zero-velocity atoms' transition is saturated, they will not as strongly absorb the probe beam. The lack of absorption will be seen as thin spikes on top of the overall Doppler feature. These thin spikes are smaller than the Doppler feature and so are known as sub-Dopper features.

Saturated absorption spectroscopy leads to a peculiar artifact known as cross-over peaks if there is more than one transition in the frequency range being swept. When considering a single transition as in the previous paragraph, the zero-velocity atoms are the only velocity class that can be simultaneously on resonance with the pump and probe beams. If there are multiple transitions present however, such is not the case. As the laser is swept, the point when it is halfway between two transition frequencies opens up a non-zero velocity class to be on resonance simultaneously with the pump and probe. For concreteness, let us consider a three level system where the ground to first excited state transition frequency is ω_1 and the ground to second excited state transition frequency is ω_2 and $\omega_2 > \omega_1$. We are interested in the case when the laser frequency f is halfway between these transition. This means

$$f = \omega_1 + (\omega_2 - \omega_1)/2 = (\omega_1 + \omega_2)/2 \tag{3.6}$$

and so the detuning from the transition 1 is $\delta_1 = f - \omega_1 = (\omega_2 - \omega_1)/2$ while the detuning from transition 2 is $\delta_2 = \omega_2 - f = -(\omega_2 - \omega_1)/2 = -\delta_1$. This is why the halfway point is important: the detunings between the two transitions are equal but opposite. Therefore, an atom with a velocity v such that its Doppler shift of the pump beam is $kv = \delta_1$ will also have a Doppler shift of the probe that is $-kv = -\delta_1$ leading to both lasers being on resonance with a transition at the same time[4]. The overall effect is as before: the pump will saturate the atoms, causing less of the probe to be absorbed than in the case of no pump, resulting in a spike appearing on top of the Doppler profile. This spike, however, is spurious and does not correspond to a transition. Because these spurious peaks occur as the laser frequency is crossing from one transition frequency to another, they are termed cross-over peaks.

Finally, The EOM and electronic components may be added to perform FM spectroscopy. The EOM serves to add sidebands onto the probe laser's frequency. When

[4]In this case, the pump will be on resonance with ω_2 while the probe will be on resonance with ω_1. If the velocity were reversed, $v \to -v$, then the transitions the beams are on resonance with would swap. In general, there are two velocity classes that are simultaneously on resonance at a cross over frequency.

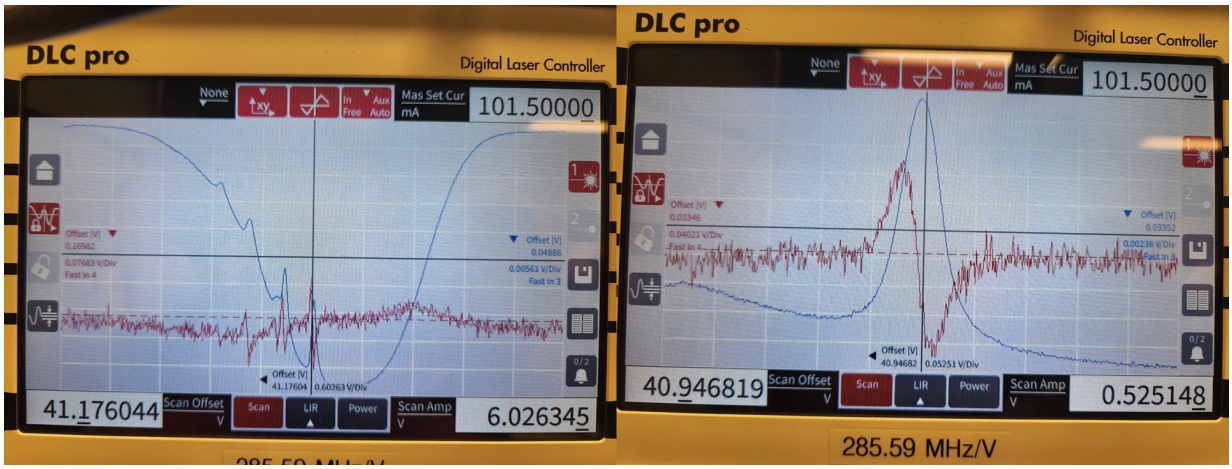

Figure 3.7: Oscilloscope trace of saturated absorption and FM spectroscopy. In both graphs the abscissa is time and the ordinate is laser power incident on the photodiode. Since the laser frequency is being changed linearly in time, the abscissa also corresponds to frequency. **Left**: the entire Doppler profile of cesium for the $6^2S_{1/2} \rightarrow 6^2P_{3/2}$ transition. The blue line shows the saturated absorption spectroscopy trace and the red line shows the error signal **Right:** close up on a single sub-Doppler feature (blue) and its associated error signal (red).

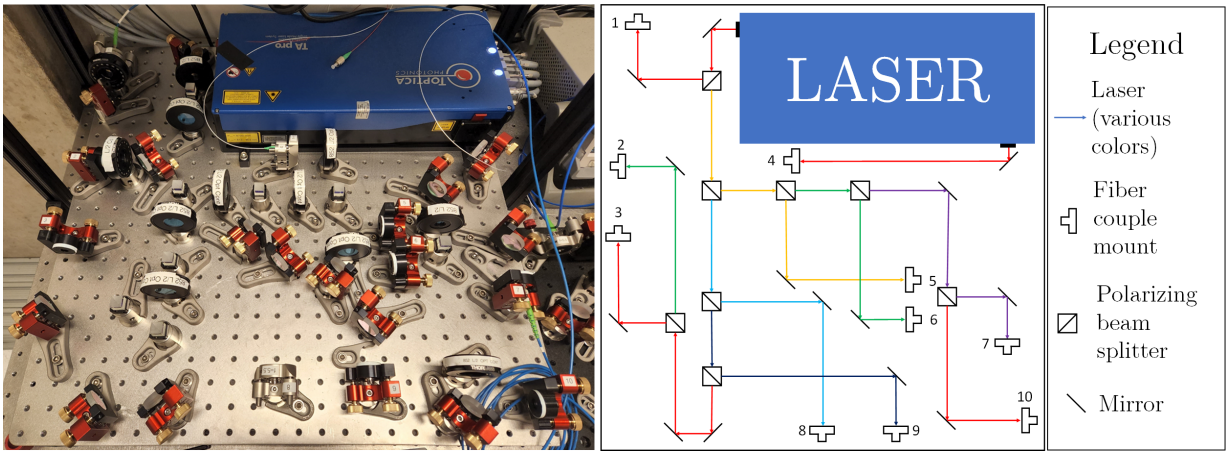

Figure 3.8: Laser distribution optical breadboard.
Left: the distribution board. **Right**: schematic representation of the board.

the laser probes the feature now, the sidebands gain a frequency dependent phase shift that, once demodulated, add in such a way to effectively produce the derivative of the sub-Doppler features [9]. Each sub-Doppler feature corresponds to a different hyperfine transition in cesium (or a cross-over), so the zero of the features' derivatives correspond to the transition (or cross over) frequency. An example of the error signal is shown in Figure 3.7.

3.3 Laser Distribution

As demonstrated in the previous sections, there are many locations that need a laser source. Lasers, however, are quite expensive, so rather than using a separate laser at each location a single high power laser can be split many times and coupled into fibers to be distributed about the lab as needed. The breadboard I designed to achieve this is shown in Figure 3.8 along with its schematic. The goal of this board is to split the laser as many times as possible, but there are several restriction to the layout. First, each splitting of the laser requires 4 components: 2 half-wave plates, a beam splitter, and a fiber couple mount. The first half-wave plate is placed just before the beam splitter to control the fraction of light reflected vs. transmitted through the beam splitter. The second half-wave plated is used to align the laser polarization with the fiber's polarization axis (discussed in Subsection 3.3.1). Second, it is ideal to minimize the paths taken by the laser as this will reduce the tendency for the optics to become decoupled. A longer path from laser to lens requires a smaller

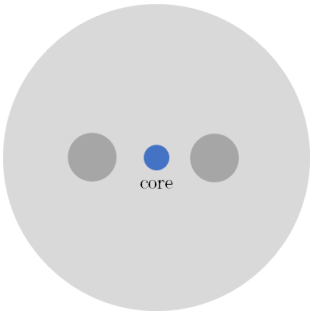

Figure 3.9: Schematic cross section of a polarization maintaining (PM) fiber optic cable. The two small dark grey circles are the stress rods, called panda ears, while the even smaller blue circle is the core through which light is transmitted.

angular change to decouple the lens, therefore the effects of thermal drift and vibrations become amplified over shorter paths. Broadly, this layout splits the laser into two main branches with couples being picked off each of these branches.

3.3.1 The Polarizing Rotor

Terminating each path of the distribution board is a fiber optic cable. These cables are polarization maintaining (PM), meaning that if polarized light enters the fiber, the light will exit the fiber still polarized if the entering light's polarization axis is aligned with one of the fiber's birefringent axes. birefringence is a material property where a medium's index of refraction is polarization dependent. Birefrigence can be used to maintain polarization, but unchecked it can hinder it. To help see how, consider linear polarized laser light moving in the z-direction (which we may align with our fiber). Linear polarization means the x- and y-components of the electric (and magnetic) field oscillate in phase. For simplicity, consider a birefringent medium in which the index of refraction for the x- component (horizontal polarization) is different than for the y-component (vertical polarization). The differing indices of refraction mean the x- and y-components will drift out of phase as the laser propagates down the fiber, and what exits the other side will be some degree of elliptically polarized light. If on the other hand only the x- or y-component entered the fiber, the polarization would be maintained as there would be no second component to drift out of phase with. This assumes however that the birefringence is not changing through space.

In fiber optic cables, bending of the cable induces stresses that lead to birefringence in the core (the portion of the cable transmitting light). The birefringence is therefore spatially dependent and somewhat outside the control of the user as fibers in a laboratory

environment can be frequently moved. This will have the effect of randomly changing the phase difference between the x- and y-components. To remedy this, PM fibers intentionally induce permanent stresses on the core much larger than those created by bending. This is done by placing so-called stress rods on opposite sides of the core to keep the core in a permanent state of high compression, shown in Figure 3.9. This creates permanently set axes for birefringence as now the bending from everyday use of the fiber will be a small perturbation on the induced stresses and have a negligible effect. So long as polarization is launched into the fiber aligned with one of these axes its polarization will not be lost from jostling of the fiber.

On the distribution board, because each laser passes through a polarizing beam splitter before entering a fiber, it is reasonable to assume the light entering the fibers is polarized, but one does not generally know what the fiber's required orientation is nor whether the laser's polarization is aligned with it.

To overcome this challenge, a polarizer can be used to determine if the entering light's polarization is aligned with the fiber axis. The idea is to shine the output of the fiber through a polarizer that is being rotated, and detect what is transmitted through. This could be done by placing a photodiode behind the polarizer and reading the signal on an oscilloscope. The variation of the photodiode's signal over time gives an indication of the polarization state of the light exiting the fiber. If the polarization were circular, the rotation of the polarizer would have no effect on how much of the light falls on the photodiode, so no variation would be seen on the oscilloscope. If the light exiting the fiber is elliptically polarized, a certain amount of variation will be seen, but the amount of light reaching the detector will never drop to zero. That is, a sine wave will be detected, the troughs of which are above zero. Linearly polarized light however will also produce a sine wave, and in this case there will be some orientation of the polarizer that will completely block the light so the troughs of the sine wave will correspond to zero. A rotating polarizer can therefore be used to align the polarized light to the fiber's axis by first maximizing the peak-to-peak distance of the sine wave, followed by small changes to drive the trough of the sinewave as close to zero as possible, at which point the polarization will be optimally aligned.

A device named the polarizing rotor was constructed to hold and rotate a polarizer. Figure 3.10 shows the assembled device while an exploded-parts view is shown in Figure 3.11. The basic principle is to use a DC motor to rotate a large pulley that is connected to a smaller pulley holding the polarizer. The large pulley is driven by a direct current (DC) motor and connected by a belt to the smaller pulley, called the pinion, which is half the diameter of the larger pulley. Under a no-slip assumption, the belt will constrain the two pullies to have the same linear velocity at the points the belt is in contact. Calling the

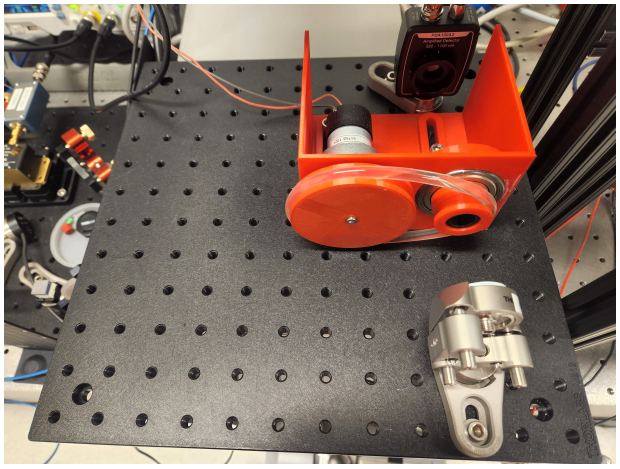

Figure 3.10: Polarizing rotor optical breadboard.
The large red structure is the polarizing rotor proper, which consists of a 1:2 torque multiplier driven by a DC motor. The pulleys and housing were all 3D printed in house. The pinion is adhered to a stock bearing from McMaster-Carr.

larger pulley's radius r_1 and angular velocity ω_1 and the smaller pulley's radius r_2 and angular velocity ω_2, this means that

$$r_1\omega_1 = r_2\omega_2 \Rightarrow \omega_2 = \frac{r_1}{r_2}\omega_1 = 2\omega_1 \tag{3.7}$$

with the last equality following from the fact that the smaller wheel is half the diameter of the larger. The ratio r_1/r_2 is typically expressed in the form $r_1 : r_2$ and is called the torque multiplier or gear reduction, though the latter term is reserved for cases when $r_1/r_2 < 1$. The DC motor is rated to run at a maximum angular velocity of 60 RPM at 24 volts, so the pinion rotates at about 120 RPM or 2 Hz maximum. The pinion is made to have a large inner diameter so that a lens tube can rest inside and hold the polarizer. Specifically, a ThorLabs SM05L05 lens tube was used for compactness. The lens tube is glued inside the pinion, and the pinion is then glued onto a ball bearing which is then glued into the housing. Mating inside the bearing is a spacer (# 7 in Figure 3.11), which was included as a last minute addition to assist with alignment. Having half the lens tube in the spacer and the other half in the pinion ensures that the pinion's axis is aligned with the bearing. If a second device were to be made, it is recommended that the pinion and spacer be joined together as one piece.

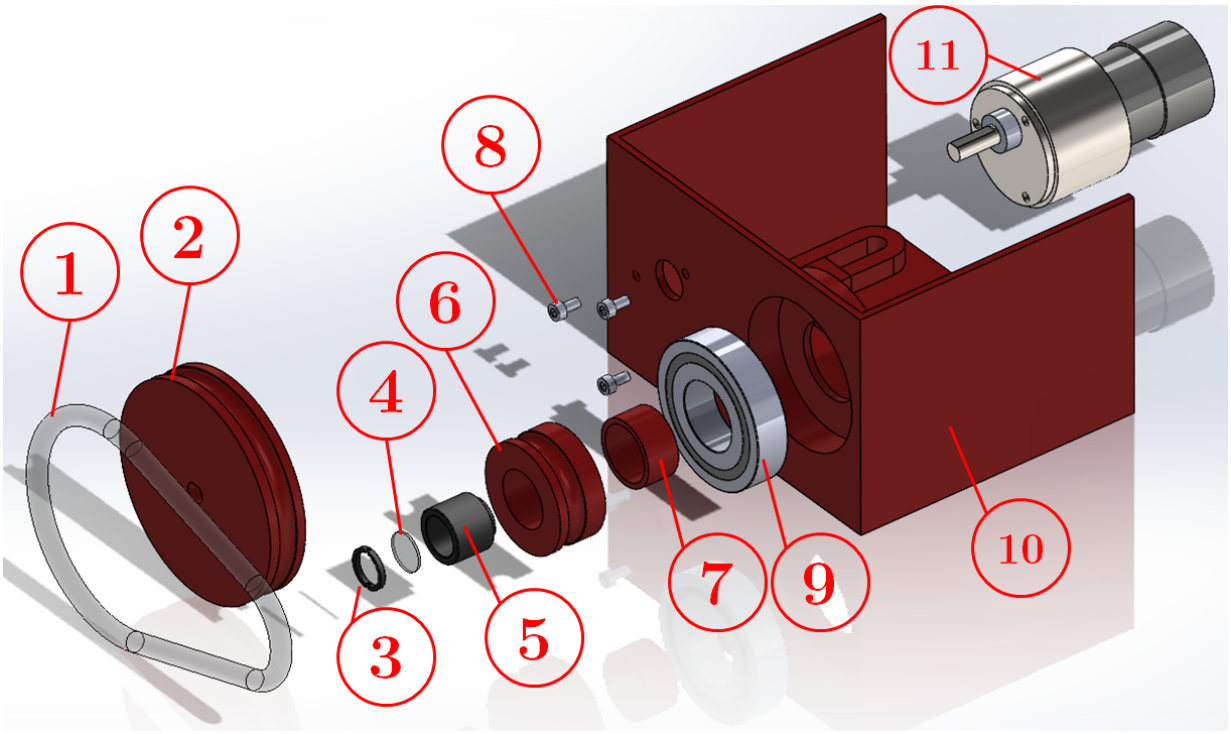

Figure 3.11: Exploded parts view of polarizing rotor.
1. Belt 2. Drive pulley 3. Retaining ring 4. Polarizer 5. 1/2" lens tube 6. Pinion i.e. driven pulley 7. Spacer 8. M4 socket head bolts 9. Ball bearing 10. Housing 11. DC motor.

Chapter 4

A New Atomic Beam Source

The previous chapter gave a broad overview of the vacuum chamber that will be used in our lab, as well as some key components for the optical control of atoms. This chapter takes a closer look at the design of the chamber's oven sub-assembly, which departs greatly from how atomic ovens are traditionally designed. Traditional ovens tend to waste a majority of their atomic flux, and generate large thermal gradients in the lab that negatively impact optical alignment near the chamber. The new design aims to mitigate these issues and is, in short, an optimization project. Optimization is often not needed in an experimental laboratory because it is a process that takes a long time and many iterations. For ad hoc devices, ones that will be put together for an experiment or two then removed, the resources required for optimization outweigh the resources lost from sub-optimal design. Optimization is really only beneficial to an experimental lab when it is for something that will be used many times over. The atomic beam source of our experimental apparatus meets this requirement. Every atomic physics experiment must start with a source of atoms; therefore, *every* experiment to be performed in our lab will make use of the beam source. Over the lifetime of the lab then, the time spent optimizing its design will produce a net benefit.

These benefits are as follows. The new design achieves a far lower exterior temperature than traditional atomic ovens, and allows for making precise alignments more stable, thereby giving finer control over single atoms. The oven keeps the heating confined to a small area within the vacuum chamber, and this allows for benefits to the achievable vacuum pressures. This in turn could lead to even more compact designs in the future. Furthermore, the atomic beam is collimated, making more efficient use of the atoms. This results in fewer oven changes, which is a time consuming and invasive process that involves breaking and reestablishing UHV.

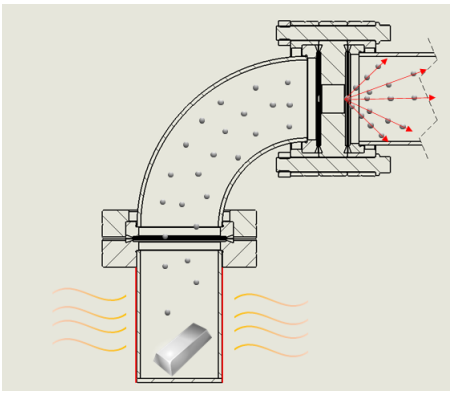

Figure 4.1: A traditional atomic beam oven.
Cross section of a prototypical traditional oven. The metal is placed at the bottom of the oven and heated from the exterior. This, combined with moderate vacuum, is enough to produce a vapor that then effuses through a small hole. As a result the atomic flux is more or less constant across the entire hemisphere.

4.1 Traditional Oven Design

We begin by looking at how atomic beam ovens are traditionally designed and the draw backs we wish to resolve with the new design. A traditional oven is depicted in Figure 4.1. In this sort of design, an ingot of the working atom is placed in the vacuum chamber and heated from an external source. This produces an atomic vapor that then exits a small aperture which sprays atoms evenly in all directions. This sort of design suffers from two main draw backs. First, the atomic flux is uniform for all angles exiting the aperture but only those atoms with a direction of motion near-parallel to the axis of the tube will be able to be slowed by the laser and captured in the magneto-optical trap. As a result, much of the atoms are simply wasted on the walls of the vacuum chamber. Second, many atoms desirable for cooling require very high temperatures such as lithium and ytterbium. With such high temperatures on the exterior of the vacuum chamber, non-trivial thermal gradients will be produced in the surrounding air, leading to currents. These air currents will negatively impact any optical components (e.g. mirrors and lenses) near the chamber.

One method to avoid both these problems is to use dispensers, but dispensers pose several problems of their own. Dispensers are only available for those elements that are prevalently used in industry for deposition processes. Furthermore, dispensers tend to be very costly (about $ 10,000 per unit) with a short lifespan. Like dispensers, our design avoids the problems of the traditional oven while having a reduced cost compared to a

dispenser, and a greater lifetime than both the traditional design and the dispenser.

4.1.1 Design Objectives

There are two ovens in the vacuum chamber. One will produce a beam of lithium atoms, the other cesium. Lithium and cesium have been chosen because of the alkali atoms, there is the largest difference in electronegativity between these two [5], leading to the largest dipole moment when formed into a molecule. In addition, of all the possible combinations of alkali pairs, CsLi has the largest dipole moment in its ground state [32]. The oven must be able to produce these beams with enough flux to load a MOT in about 1 second. This benchmark is chosen because experiments take about 10 ms to a few seconds to perform per run. If the MOT requires more than about a second to load, then the bulk of the time in the experiment is spent on loading the MOT and it becomes a bottleneck [30]. Based on the size of the oven's nozzle, and the capture range of the Zeeman slower [27], we pessimistically expect to capture about 1% of the flux leaving the nozzle in the 2D MOT. In general, MOTs have a maximum capture number of 10^9 atoms [30], so this requires a flux leaving the oven of at least 10^{11} atoms per second in order to load the 2D MOT in one second.

The flux leaving the oven is proportional to the vapor pressure of the atoms. The vapor pressure for lithium at a given temperature is lower than that of cesium [51], and so the maximum temperature required of the oven is determined by the vapor pressure required to produce a sufficient flux of lithium. Using lithium's Antoine equation [3] and the ideal gas law, the flux of lithium leaving the oven at 400°C was found to be on the order of 10^{14} atoms per second. From this, for conservatism, the upper temperature requirement of the oven was taken to be 450°C. This allows for the possibility for these rough calculations to be over estimates by one or two orders of magnitude without a deleterious impact to the performance of the oven.

Finally, the new design aims to reduce the amount of atoms that are unable to be captured by the MOT. This is desirable because the more efficiently the atomic source is used, the less frequently it must be replenished. Bringing a vacuum chamber back up to atmosphere to reload, and then back down to UHV is at least a week long process. Reducing the frequency with which it must be performed allows for more time running experiments and collecting data.

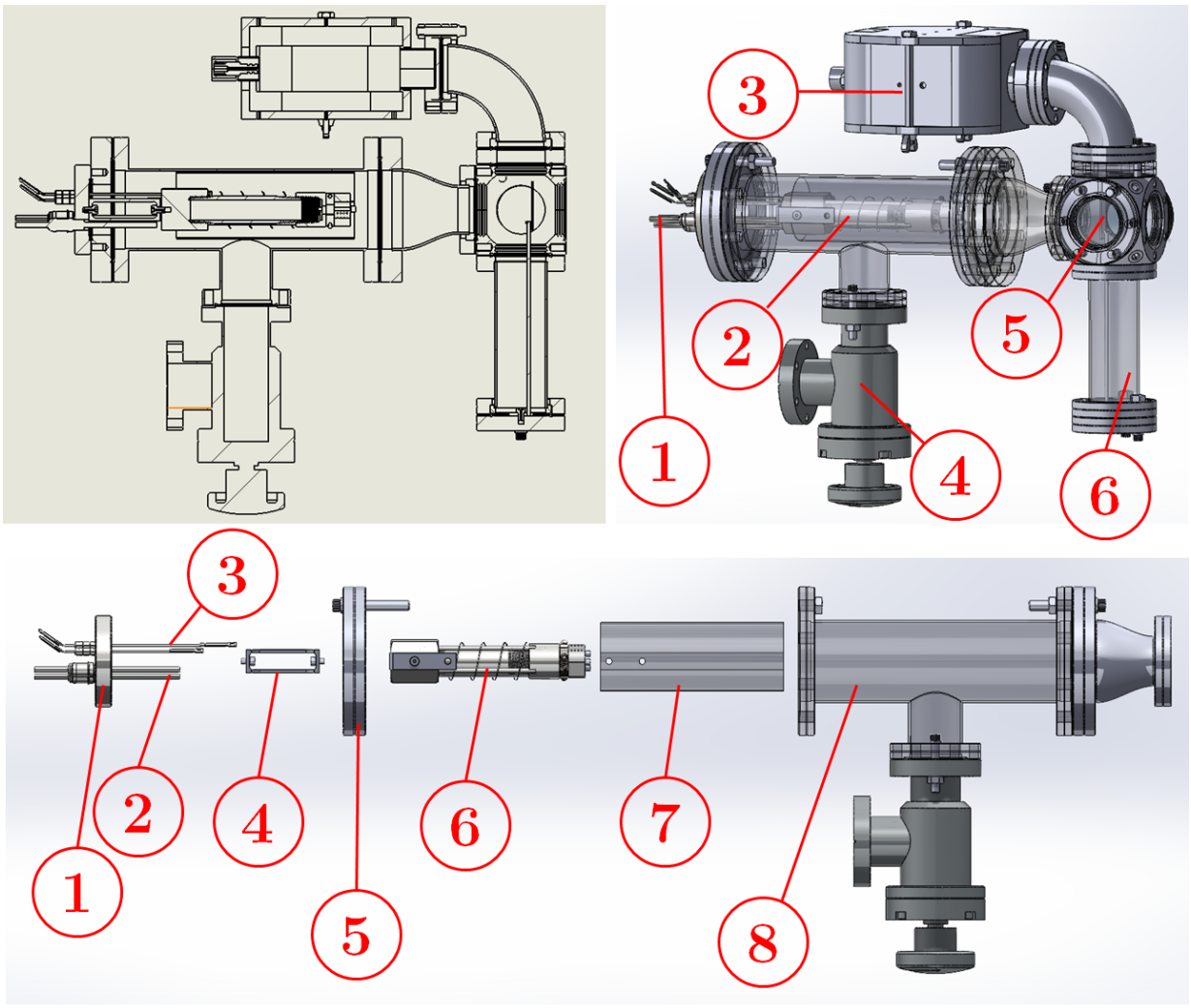

Figure 4.2: CAD model of the new oven.
Top left: cross section of oven. **Top right**: trimetric view of CAD Model 1. Power and thermocouple feedthrough leads 2. Crucible assembly 3. 10 L/s ion pump 4. All metal angle valve 5. Beam blocker 6. Hydraulically formed bellows. **Bottom**: exploded parts view. 1. Thermocouple and power feedthrough 2. Power leads 3. Thermocouple leads 4. Cantilever 5. Adapter flange 6. Crucible 7. Heat shield 8. Vacuum chamber.

4.2 New Oven Design

The new oven design is shown in Figure 4.2. Fundamentally, the design is a crucible suspended in a vacuum chamber. The crucible is filled with the desired atomic species and brought to a high temperature via heating wires. The crucible is closed except for a hole in the front which atoms may pass through. This hole would spray atoms uniformly hemispherically, so a microchannel nozzle is placed in front to collimate the beam. This is discussed in Subsection 4.2.2. Since the oven has only an active heating element, and no active cooling element, a beam block (# 6 in top right panel of Figure 4.2) is used to stop the atomic beam from continuing into the next chamber when needed. This design is more economical in its emission of atoms, and heating is performed within the vacuum chamber on an isolated piece that is greatly thermally decoupled from the rest of the system.

4.2.1 The Crucible

The crucible design is shown in Figure 4.3 and shown assembled in Figure 4.6. The crucible proper is made of 316 stainless pipe fittings and consists of three components: the front cap, rear cap, and pipe (#'s 5, 4, and 1 respectively in Figure 4.3). The pipe is 1/2 NPT with an overall length of 3.5". The rear cap (#1) has a tapped blind hole in its center exterior to allow the crucible to be mounted and suspended from a ConFlat flange. Because this hole is blind, it is fastened to the assembly with a vented screw. The front cap has a .25" diameter through hole in its center to serve as the nozzle for the atomic beam. Spaced evenly around this hole are 3 tapped 4-40 through holes on a .5" bolt circle diameter. This allows for mounting of the microchannel nozzle (#6) and its heater (# 7).

To heat the crucible, it is wrapped with a coil of 24 gauge nickel-chromium wire (# 2). Tungsten wire was originally used for its high melting temperature, but it was found to turn brittle after being heated and would snap from the slightest disturbance. Nickel-chromium is commonly used for resistance heating, and remains malleable even after repeated heatings and coolings. Its electrical resistivity increases as the gauge increases (diameter decreases). Since the power dissipated in a resistor—and hence transferred to its surroundings as heat—is proportional to the resistance and the square of the current, a higher resistivity wire will produce more heat for the same current. The wire cannot be made arbitrarily small however because the maximum current a wire can withstand before breaking decreases as the diameter decreases. It is nonetheless desirable to keep current requirements low, as sourcing large currents is both more dangerous and more expensive. From experimentation, it was found that a current of 0.5 to 3 amps was needed to achieve temperatures in the

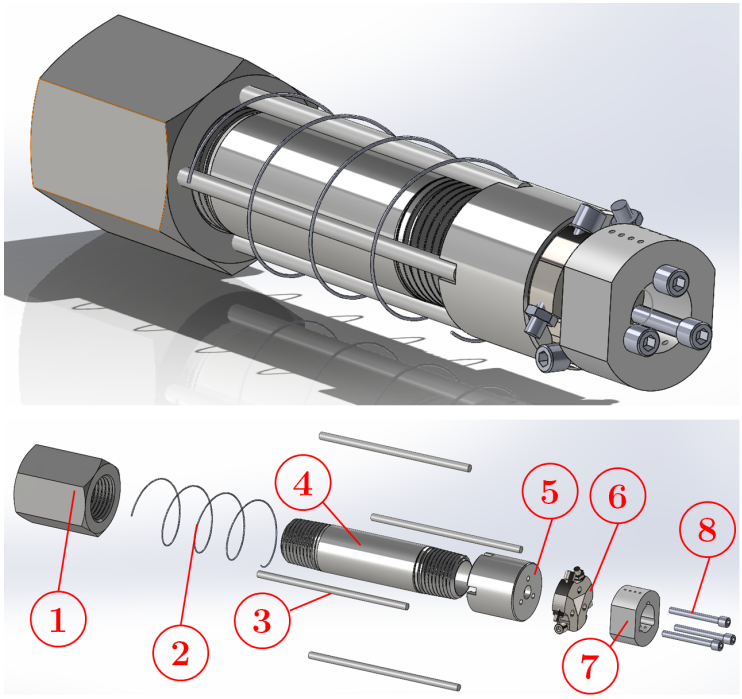

Figure 4.3: CAD model of the crucible.
Top: trimetric view of crucible model. **Bottom**: exploded parts view 1. Rear cap 2. Heating wire 3. Ceramic dowels 4. American national standard taper pipe thread (NPT) steel pipe 5. Front cap 6. Microchannel nozzle 7. Microchannel nozzle heater 8. 4-40 silver plated bolts.

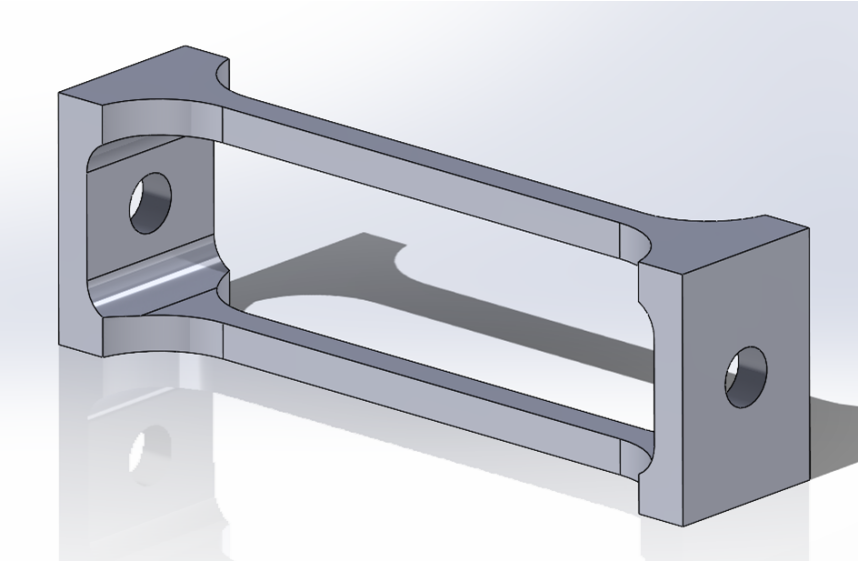

Figure 4.4: CAD model of the cantilever.
The cantilever is designed to provide a high thermal resistance while also being easy to machine from a mill.

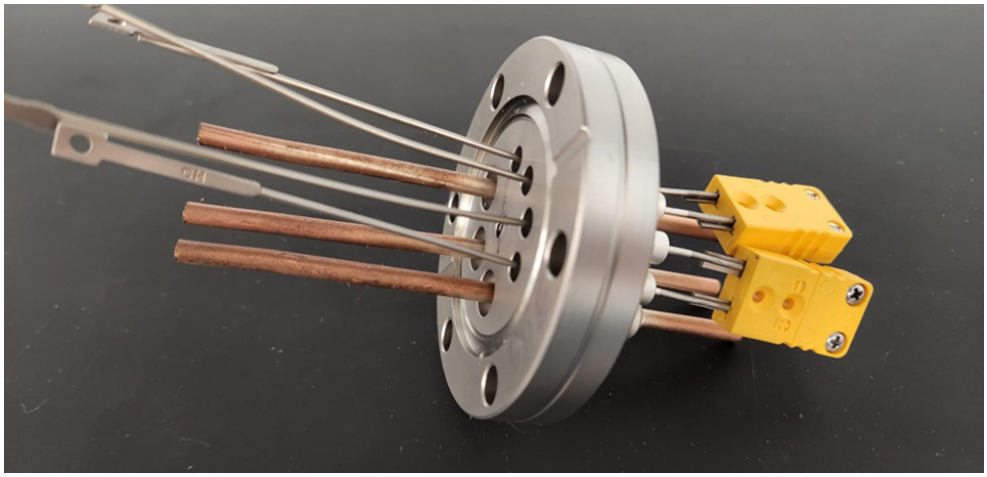

Figure 4.5: MPF A0800-2-CF thermocouple-power feedthrough.
The feedthrough has two Type K thermocouple lead pairs, and three .156" diameter power leads all fedthrough a 2¾ ConFlat Flange. The feedthrough has been machined in house to shorten the lengths of the power leads and add an 8-32 tapped blind hole into the base. A short cantilever (Figure 4.4) is attached to this hole which the crucible then attaches to.

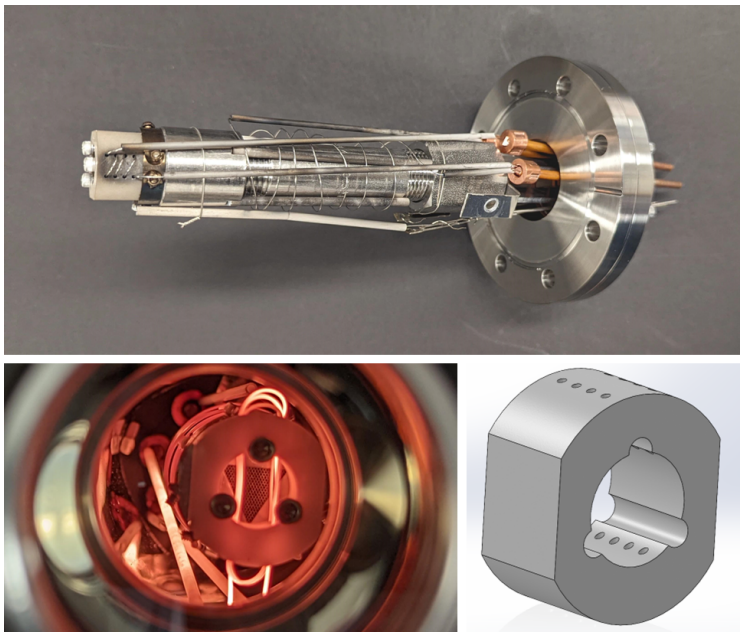

Figure 4.6: The crucible and nozzle heater.
Top: the crucible ready for installation into the vacuum chamber. **Bottom left**: view of the heat wires as they bring the crucible to operating temperature. **Bottom right:** CAD model of the nozzle heater.

range 50°–500°C with 24 gauge wire. Any smaller, and the wire was prone to fail after several hours of use.

Since the crucible is itself a conductor, the heating wire must be kept isolated from it. This is accomplished by four ceramic Macor rods that are positioned radially around the crucible's body. Small channels are cut into the front cap to help prevent the rods from moving, but otherwise the rods are held in place purely by the tension of the heating wire. The microchannel nozzle is separately heated by its own coil of nickel-chromium wire (Figure 4.6, bottom panels). This coil is held in front of the nozzle by means of a custom machined piece of Macor (# 7 in Figure 4.3). This allows the operator to run the nozzle at a different temperature than the crucible. It is preferable to have the nozzle at a slightly higher temperature than the crucible, because this ensure the vapor pressure in the nozzle is higher. Were the vapor pressure lower than the crucible, atoms would deposit inside the nozzle leading to clogging. The vapor pressure of Cesium for a given temperature can be calculated using the Antoine equation [54]

$$\log_{10}(P) = A - \frac{B}{T + C}, \tag{4.1}$$

where P is the vapor pressure, T is the temperature, and the parameters A, B, and C, have been calculated from Reference [54] by the national institute of standards and technology (NIST) [3] and are reproduced here for convenience: $A = 3.69576$ Barr, $B = 3453.122$ Barr $\cdot$ K, and $C = -26.829$ K. For the operating range of the oven, 50°–450°C, this equation predicts that a 50°C increase in temperature results in about a half to an order of magnitude increase in the vapor pressure in bars, which is expected to be enough to prevent clogging. It should be noted that Equation 4.1 is only valid for the temperature range 552–963 K, but testing in the lab has found that holding the nozzle at 50°C above the crucible prevents clogging even below the range of applicability of Equation 4.1.

Power is supplied to the heating wires via the feedthrough shown in Figure 4.5. This piece allows 3 power leads and two thermocouple leads to be passed from the exterior of the chamber to the interior without breaking vacuum. The heating wire is attached to the power leads by copper crimps as shown in Figure 4.6. To avoid the various wires from shorting on each other, each wire is run through its own ceramic tube. Additionally there are two thermocouples attached to the crucible. These are attached on the body and nozzle and electrically isolated the same way using ceramic tubes (the nozzle's thermocouple can be seen in Figure 4.6). These thermocouples are necessary for the operator to ensure the crucible and nozzle are at their desired temperatures.

The crucible is suspended from the feedthrough as a cantilevered beam. If the crucible were in direct contact with the feedthrough, the heat flux coming from the crucible could

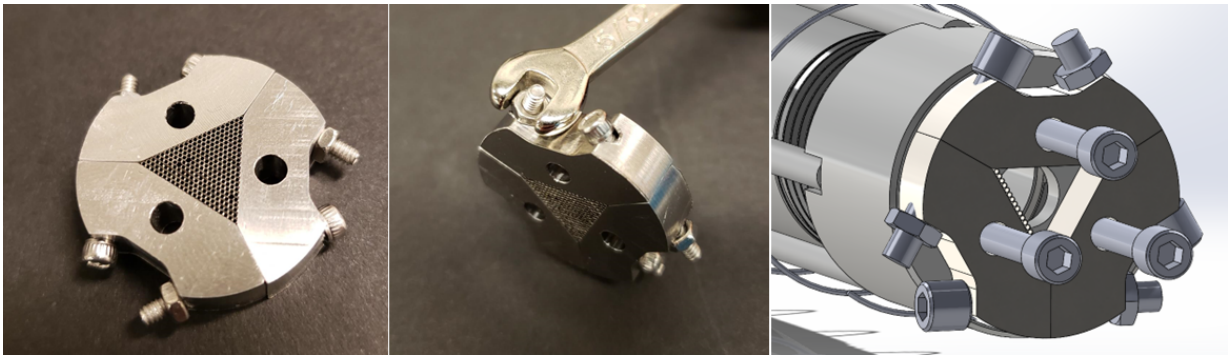

Figure 4.7: The microchannel nozzle.
From left to right: head-on view of the microchannel nozzle, a tool fitting into the microchannel nozzle, and the microchannel nozzle assembled to the crucible.

easily conduct into the walls of the vacuum chamber. To avoid this, a small structural beam of minimal cross section called the cantilever (Figure 4.4, #4 bottom panel Figure 4.2) is placed between the crucible and feedthrough to act as a thermal conduction resistor. In addition, the wires radiate thermally outwards to the chamber walls just as well as they do to the crucible. Effectively, half the wire's radiation is lost. This is minimized by including a heat shield (# 2 top right panel and # 7 bottom panel Figure 4.2), which serves to both more efficiently heat the crucible, and lower the exterior temperature of the vacuum chamber.

4.2.2 Microchannel Nozzle

The purpose of a microchannel nozzle is to help collimate the atomic beam. Having the beam collimated is desirable as it reduces the amount of wasted atoms leaving the oven, which reduces the frequency of oven changes. Our design is based on previous designs from other research groups [49, 55]. Our microchannel nozzle is shown in Figure 4.7.

The microchannel nozzle is a stack of hypodermic needles with a length much larger than the diameter. Holding a stack of such needles in front of the main nozzle serves to restrict the velocities of atoms that exit the chamber, for only those atoms with a velocity nearly parallel to the axis of the needles will successfully leave the chamber. If the transverse velocity is too high, the atoms will collide with the side of the chamber and re-emit in a random direction. Such atoms are more likely to re-emit back into the crucible rather than out the nozzle. This is because most atoms will collide with the

tube walls before the midpoint which is a result of the atoms' trajectory in the crucible having a uniform angular distribution [49]. Put another way, collimation is selecting those atoms whose component of velocity transverse to the needle axis is much smaller than the longitudinal component. This can be seen with the aid of Figure 4.8. The time for an atom to travel through the tube is

$$t = \frac{L}{v_{\mathrm{l}}} \tag{4.2}$$

were v_{l} is the atom's velocity component longitudinal to the tube axis. In order to escape the tube, the atom must not reach the inner diameter during its transit, and so it can have a transverse velocity no faster than

$$v_{\mathrm{t}} = \frac{h}{t} = \frac{h}{L} v_{\mathrm{l}}. \tag{4.3}$$

Defining $\alpha \equiv h/L$ as the aspect ratio, we can see that the needles' aspect ratio sets the theoretical degree of collimation of the atomic beam. We are free to choose h and L as desired. However, there is an additional constraint on the length of the needles that takes precedence. The needles should not be longer than twice the mean free path of the atoms [49]. From kinetic theory, one can show that the mean free path of a particle is given by [43]

$$\lambda = \left(\sqrt{2}\pi d_0^2 n\right)^{-1}. \tag{4.4}$$

For cesium, the squared atomic diameter was determined experimentally by the national aeronautics and space administration (NASA) [37] and found to be $d_0^2 = 2.4 \times 10^{-17}$ m^2. The number density can be calculated from the ideal gas law. For cesium a temperature of 78°C is used. Since the crucible is in UHV, the pressure comes almost entirely from the vapor pressure, which can be calculated using the Antoine equation for cesium [54] or looked up in a graph [51]. The mean free path is found to be approximately .16". This means there is a limit on the length of the needles at .32". The length of the needles are therefore chosen to be .25". This will help prevent clogging while still allowing a majority of the beam flux to reach the MOT.

For the needles' diameter, h, we chose to use the same needles as our predecessors, 304H25XX from microgroup [55], which have an inner diameter of .0155"–.0170". With the aspect ratio set, we can calculate the optimal placement of the MOT and the flux effusing from the nozzle. To find the flux for a hole with negligible thickness and area A_{h}, the flux is given by [55]

$$\frac{dN}{dt} = \frac{1}{4} n v_{\mathrm{mean}} A_h \tag{4.5}$$

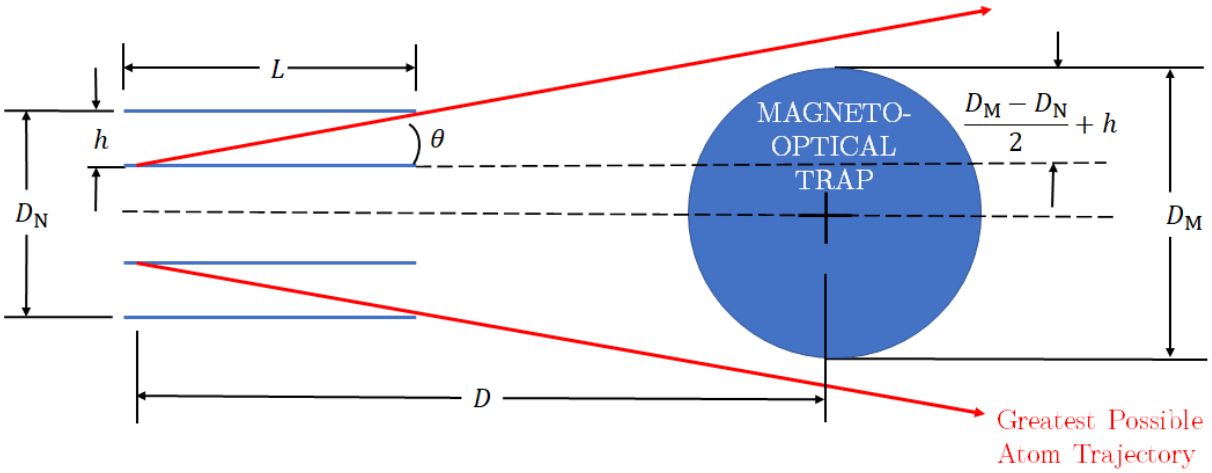

Figure 4.8: Diagram of the collimating effect of the microchannel nozzle. Cross section of the needle stack with only the top most and bottom most needles shown (horizontal blue lines). The red arrows trace out the maximum spread of atoms from the nozzle. The large blue circle on the right depicts the diameter, D_M, of our MOT. Its distance from the needles, D, is constrained by the geometry of the vacuum system and must be somewhere between 8" and 10". D_N is the diameter of the hole on the front of the crucible which is chosen to be .25". The MOT will have a diameter of about .6".

where v_{mean} is the average velocity of the particles. When the thickness is not negligible, and $L \gg h$, this flux is diminished by the factor $\frac{4}{3}\alpha$ [44]. Using this method, our design is predicted to yield a flux on the order of 10^{13} to 10^{14} atoms per second for cesium atoms at 78°C. But not all of the atoms will necessarily reach the MOT. With the aid of Figure 4.8, the MOT's maximal distance from the nozzle can be calculated via similar triangles as

$$D = \left(\frac{D_{\text{M}} - D_{\text{N}}}{2h} + 1 \right) L \approx 6.3\text{”}. \tag{4.6}$$

Since the MOT cannot be placed any closer than 8” away, the flux reaching the MOT is reduced from the total flux by the ratio of the solid angles swept out by the MOT to that of the needles.

4.2.3 Material Considerations

Material selection is driven by a number of factors such as cost, machinability, strength, rigidity, resistance to fatigue, and resilience to environmental conditions [10] (This is not intended to be an exhaustive list). It is often just a small handful of these considerations that ultimately drive the selection of the material. In the case of the crucible components, this is certainly true, as selection is largely driven by the material's resilience to its environment. Of greatest concern, the materials must not outgas or leach chemicals that break UHV. This prevents carbon steels from being used, which begin to leach out carbon monoxide below $\sim 10^{-2}$ mTorr. In addition, the crucible must be able to be brought to high temperatures without suffering damage to its form, fit, or function. Additionally, resistance to fatigue takes a sub-leading roll, as there will be a great deal of thermal cycling to the components, so thermally induced strains and material creep is of concern. While thermal strain is unavoidable, its effects can be minimized by making every metallic component of the crucible and cantilever from the same material and alloy. This ensures they all have the same coefficient of thermal expansion, and therefore will not create shear strains (which serve to deflect the atomic beam's direction) due to different pieces expanding at different rates.

A typical first choice is aluminum due to its relatively low cost and ease of machining, but the temperature is too high. At maximum operating temperature (450°C), aluminum's strength is at best 4% of its room temperature value [1]. Since weight is not a concern, the

[1] See Figures 3.6.2.2.1(a) and (b) from MMPDS-11 [1] [1]. The graphs show the thermal knockdowns of aluminum's ultimate and yield tensile strengths respectively. Specifically, they are for Aluminum 6061-T6, a common high strength allow and temper for structural components, and also the most readily available

next cost effective solution is to use steel. Steel's strength will drop to about 60% of its room temperature value at operating temperatures[2] [1]. This is an acceptable reduction in strength, but a specific alloy must also be chosen. Carbon steels must be avoided because of their propensity to outgas. This leaves available tool and stainless steels. Between these two, the greater corrosion resistance afforded by stainless steel makes it the preferred choice. Specifically, we have chosen to make the crucible's metallic components from 316 stainless steel. The one exception to this are the fasteners. The stresses in a bolt's threads, combined with the high temperature, is enough to potentially weld the components together in a process known as galling [10]. This is commonly protected against by plating the bolts with silver. The bolts in the crucible assembly are all silver plated, and those mating with a blind hole are vented to minimize outgasing.

4.2.4 Thermal Analysis

In addition to material concerns, the operating temperature of the crucible makes it desirable to thermally insulate the crucible from the rest of the vacuum system. This provides two benefits. First, insulation keeps the vacuum chamber's exterior temperature lower, which reduces the chance of causing burns to experimenters who accidentally bump the chamber, and also prevents large air currents forming from natural convection. Second, it reduces the power required to maintain the crucible at a given temperature.

Fortunately, the crucible is in UHV so heat primarily transfers radiatively. To reduce the amount of radiation reaching the rest of the vacuum system, an aluminum foil heat shield surrounds the crucible to reflect heat back. The heat transfer of this configuration is a well studied engineering problem [28]. For two infinitely long coaxial cylinders, the heat transfer rate leaving the interior cylinder's surface and reaching the exterior cylinder's inner surface is given by

$$q_{12} = \frac{A_1 \sigma (T_1^4 - T_2^4)}{\frac{1}{\varepsilon_1} + \frac{1-\varepsilon_2}{\varepsilon_2}\left(\frac{r_1}{r_2}\right)} \tag{4.7}$$

alloy of aluminum from McMaster-Carr. There are higher strength alloys, such as 7075, but even so, at a 4% reduction the extra strength from these harder-to-source alloys is still unworkable. Furthermore, the graphs are representative of the large reduction in the strength of aluminum in general due to operating near 60% of its melting point.

[2] See Figure 2.7.1.1.1(b) [1]. Note that most charts don't show over 1/2 hour of heat exposure for steel because extended exposure to such high temperatures can alter the tensile properties of steel (typically becoming more ductile) [10]. Since we have high margins, the potentially altered tensile properties are not of great concern.

where q_{12} is the rate of heat transfer leaving surface area A_1 of the interior cylinder, r_1, T_1, and ε_1 are the radius, temperature, and emissivity of the interior cylinder's surface, and r_2, T_2, and ε_2 are defined analogously for the exterior cylinder's interior surface [28]. All emissivities in this discussion are average hemispherical emissivities. The cantilever provides an additional path for heat transfer via conduction. Its heat transfer rate is given by

$$q = \frac{kA}{L}(T_1 - T_2) \tag{4.8}$$

where k is the thermal conductivity of the cantilever, L its length, A its cross sectional area whose normal is parallel to the direction of heat transfer, and T_1 and T_2 are the temperatures at the opposite sides of the cantilever[28]. These two equations for heat transfer may be used to estimate whether the oven's heat transfer is dominated by radiation, conduction, or split nearly equally between the two modes. For example, given that the cantilever is made of 316 stainless steel, it has a thermal conductivity $k = 15.2\text{W/m} \cdot \text{K}$. From its design we know it has an overall length $L = 2.2$" and a cross sectional area $A = .02"^2$. The temperature of the side in contact with the crucible will be equal to the crucible's temperature, $T_1 = 450°\text{C}$ while the side opposite we may assume for a rough estimate to be equal to the laboratory's ambient temperature $T_2 = 22°\text{C}$. This produces a heat rate for conduction of 1.2 Watts. For radiation, the procedure is slightly more complicated since the temperature of the heat shield is not known. One must use Equation 4.7 in series twice: once for the heat transferred from the crucible to the heat shield, and again for heat shield to vacuum chamber. Upon doing so and substituting in the appropriate geometry and material properties, one finds that for radiation the net rate is 1.5 Watts. These rough estimates suggests that neither mode is dominant in the system, and that equal care should be taken to minimize both modes of heat transfer. To aid with sizing the cantilever and heat shield, a more thorough analysis was performed to allow for estimation of the vacuum chamber's exterior temperature. Specifically, an effective resistor network of the system was made to help estimate the temperature of the vacuum system's exterior, shown in in Figure 4.9.

Referring back to Equation 4.7, radiation can be minimized by keeping the emissivity and diameter of the heat shield as small as possible. This is what has influenced the geometry of the heat shield. Its diameter is the minimum that allows for assembly without touching any of the components it surrounds. Furthermore, its material is a specially made foil with a polished side for minimizing the emissivity of the interior. For conduction, referring back to Equation 4.8, there are two parameters that can be changed to increase the cantilever's resistance to conduction: its cross sectional area, and its length. The cross sectional area was chosen to be as small as possible while still easily machinable with a

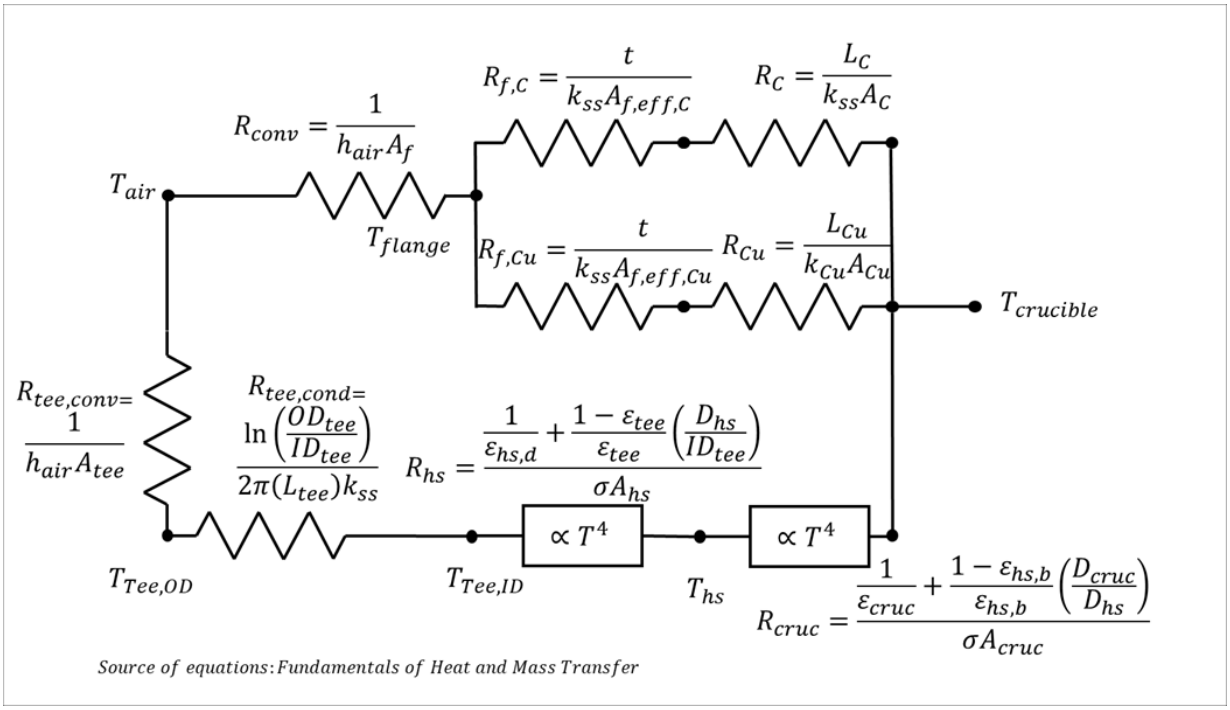

Figure 4.9: Resistor network of heat transfer in the oven.
Conductive and convective modes of heat transfer are linear in temperature and admit an analogy between electric circuits where heat transfer rate q is analogous to current, temperature T is analogous to voltage, and the two are related through a proportionality constant called the resistance, which is determined through geometry and boundary conditions. Heat transfer through radiation acts as a non-linear element as it is proportional to T^4, and while a resistor analogy can still be made, it cannot be reduced to an equivalent resistance with the conductive and convective resistances. The variables in the figure are summarized in Table 4.1.

Variable	Definition
A_{c}	Cross sectional area of cantilever.
A_{cruc}	Surface area of crucible.
A_{Cu}	Cross sectional area of copper rods.
A_{f}	Surface area of flange exposed to convection.
$A_{\mathrm{f,eff,C}}$	Effective area of conduction through flange from crucible.
$A_{\mathrm{f,eff,Cu}}$	Effective are of conduction through flange from copper rods.
A_{hs}	Surface area of heat shield.
A_{tee}	Exterior surface area of tee exposed to convection.
D_{cruc}	OD of crucible.
D_{hs}	Diameter of heat shield.
ID_{tee}	ID of tee.
OD_{tee}	OD of tee.
h_{air}	Natural convection coefficient of air.
k_{Cu}	Thermal conductivity of copper.
k_{ss}	Thermal conductivity of stainless steel.
L_{C}	Overall length of cantilever.
L_{Cu}	Length of copper rods.
L_{tee}	Length of portion of tee exposed to convection.
R_{C}	Conductive thermal resistance of cantilever.
R_{conv}	Convective thermal resistance of flange.
R_{cruc}	Radiative thermal resistance from crucible to heat shield.
R_{Cu}	Conductive thermal resistance of copper rods.
$R_{\mathrm{f,C}}$	Conductive thermal resistance of flange to cantilever.
$R_{\mathrm{f,Cu}}$	Conductive thermal resistance of flange to copper rods.
R_{hs}	Radiative thermal resistance from heat shield to tee ID.
$R_{\mathrm{tee,cond}}$	Conductive thermal resistance of tee.
$R_{\mathrm{tee,conv}}$	Convective thermal resistance of tee.
t	Thickness of flange.
T_{air}	Temperature of laboratory air (boundary condition 22°C).
T_{crucible}	Temperature of crucible (boundary condition 450°C).
T_{f}	Temperature of flange exterior.
T_{hs}	Temperature of heat shield (assumed uniform through thickness).
$T_{\mathrm{tee,ID}}$	Temperature of tee ID.
$T_{\mathrm{tee,OD}}$	Temperature of tee OD.
$\varepsilon_{\mathrm{cruc}}$	Normal emissivity of crucible.
$\varepsilon_{\mathrm{hs,b}}$	Total hemispherical emissivity of heat shield interior ("bright" side).
$\varepsilon_{\mathrm{hs,d}}$	Total hemispherical emissivity of heat shield exterior ("dark" side).
$\varepsilon_{\mathrm{tee}}$	Total hemispherical emissivity of tee ID.

Table 4.1: Resistor network variables.

mill. The length of the crucible was chosen to be as long as possible without causing the crucible to no longer fit inside the chamber. The length is therefore set by the size of the components surrounding it. Namely, the ConFlat tee and conical reducer (# 8 bottom panel in Figure 4.2). The size of the tee was chosen to be the smallest size possible that can contain the crucible. This is to minimize the space the chamber requires in the lab to allow for maximal room for optics.

4.2.5 Alignment of the Atomic Beam

The crucible and cantilever form a cantilevered beam[3]. It is important to make sure that the crucible does not deflect under its own weight so greatly that the atoms leaving the crucible are no longer on a trajectory to reach the MOT. The deflection may be estimated using Euler-Bernoulli bending theory [21]. The crucible is approximated as a prismatic member with annular cross section and the cantilever is approximated as a prismatic member with rectangular cross section as shown in Figure 4.10. A prismatic member is a structural component whose cross section is constant throughout its length. Accounting for the decreased stiffness of 316 stainless steel at operating temperature, the greatest angular deflection due to beam bending was found to be 1.43×10^{-5} radians. At the center of the MOT 8" away, this results in a linear deflection of .2 thousandths of an inch, or about 7 μm. The MOT is conservatively expected to have a diameter of .6", so this deflection is negligible. In addition, the atomic beam's path can deviate from its true position due to the misalignment of mating components. To minimize this, the components have been toleranced near what is possible using a mill. This results in constraining the worst possible deflection of the atomic beam due to misalignment to .033" or 0.86 mm.

4.3 Cesium Production

Cs is highly reactive with water to the point that when exposed to the water vapor in the atmosphere it ignites [31]. This poses a challenge to loading the crucible, as it must be done in an environment that can be evacuated of water vapor e.g. in a glove box that has been pumped out and refilled with argon. The potential dangers of working with pure cesium coupled with the greatly increased difficulty of assembling the crucible inside a glove box makes it desirable to find a method of producing a cesium beam that does not rely on working directly with pure cesium.

[3]beam here meaning a structural member with a characteristic length in one direction far greater than in any other and loaded transverse to its axis, not to be confused with a laser beam or atomic beam.

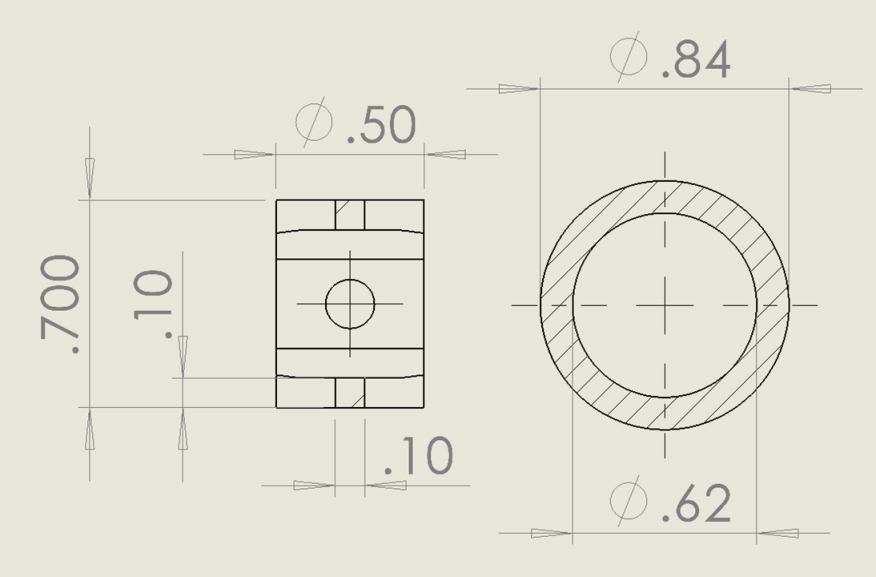

Figure 4.10: Cross section of cantilever and crucible for calculating deflection. The cross sections shown in this diagram are assumed to be uniform throughout the lengths of the components.

Cesium chloride (CsCl) offers a potential solution. It is unreactive with the water vapor in the air, and readily reacts with calcium (Ca) at elevated temperatures to form cesium and calcium chloride (CaCl) viz.

$$2\mathrm{CsCl} + \mathrm{Ca} \rightleftharpoons \mathrm{CaCl_2} + 2\mathrm{Cs} \tag{4.9}$$

which is a common process for producing solid cesium [26, 33]; some methods even employ distillation of a cesium vapor [47, 48]. The reaction (Equation 4.9) could therefore be carried out in the crucible and thus avoid the need to work with pure cesium directly.

4.3.1 Experimental Setup and Data

To test the feasibility of cesium chloride and calcium, the oven was assembled as shown in Figure 4.11. The crucible was loaded with a 2:1 mixture of cesium chloride powder to calcium granules as this has been found to produce the most efficient yield [33]. In the shown orientation the crucible is pointing directly upwards. A laser can be shone through the pictured viewports and used to detect cesium either through a fluorescence or

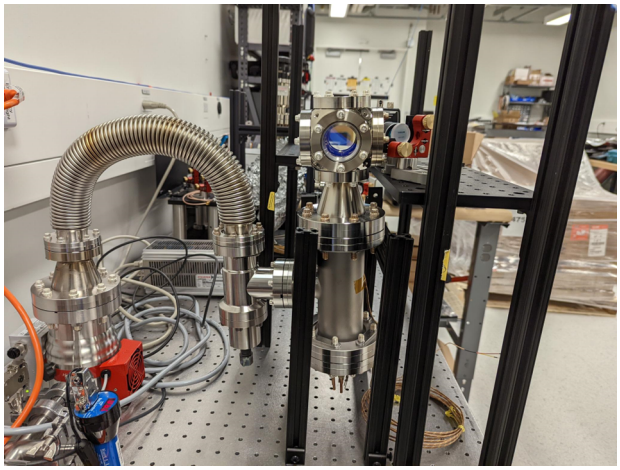

Figure 4.11: The experimental test bed.
The crucible was loaded with CsCl and Ca and placed in the vacuum chamber. The crucible is heated to different temperatures and the flux of cesium effusing from the crucible is measured using absorption spectroscopy.

absorption measurement. We chose to measure absorption, and an additional breadboard was placed approximately at the location from which the photo in Figure 4.11 was taken so that a laser could be shone through the chamber onto a photodiode. This is shown in Figure 4.12. Specifically, a ThorLabs PDA100A2 photodiode was used and fitted with a ThorLabs FL850-10 notchpass filter. The filter was included because the nickel-chromium wires used to heat the crucible emit a significant amount of blackbody radiation near 852 nm that interferes with measurements on the photodiode. The filter blocks out the majority of the radiation from the wires as well as the room lights. The photodiode's output was fed into a Keysight EDUX1052G oscilloscope from which measurements of the flux could be made by measuring the voltages on the oscilloscope. Specifically, the laser frequency was swept around cesium's $6^2S_{1/2}$ to $6^2P_{3/2}$ transition to probe for absorption as a function of frequency; if the intensity of the laser on the photodiode dips significantly at the transition frequency, this is evidence that the laser has passed through a gas of cesium.

To produce the atomic beam, the oven was heated in increments of 10°C from 200°C to 360°C and the flux at each temperature step was measured. No flux was detected until 360°C even after sweeping the laser's path through the entirety of the viewport and allowing 2 hours between temperature increments to ensure the powder's temperature had reached steady state with its environment. However, upon reaching 360°C a flux similar to that shown in Figure 4.14 at the 360°C data point was measured. Upon subsequent

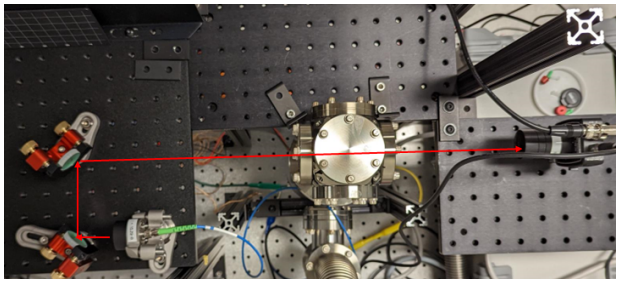

Figure 4.12: Top down view of the test bed.
A laser is shone through the vacuum system where it interacts with Cs before landing on a photodiode for detection. The red arrow traces out the approximate path of the laser beam.

cooling and reheating, fluxes at lower temperatures were detected, as low as 300°C. It has been found that each time the crucible is reloaded, the mixture will not produce a cesium vapor until first reaching between 360°C and 450°C after which it will continue to produce cesium even at lower temperatures. The signal at 360°C is shown in Figure 4.13.

The atomic beam flux can be calculated from the measured voltages using Beer's law:

$$I(\omega, z) = I_0 \exp(-\kappa(\omega) z) \tag{4.10}$$

Where I_0 is the initial intensity before absorption, $I(\omega, z)$ is the intensity a length z into the cesium gas at frequency ω, and $\kappa(\omega)$ is the absorptivity of cesium for monochromatic radiation of frequency ω. The absorptivity is related to the flux through the relation

$$\Phi = \frac{\kappa(\omega)}{\sigma(\omega)} v_{\mathrm{m}}(T) \tag{4.11}$$

where σ is the optical cross section of cesium at ω and $v_{\mathrm{m}}(T)$ is most probable velocity of a cesium atom at temperature T.

The measured voltages can be converted to intensities by accounting for the photodiode's gain G and Responsivity R. For a beam with a waist of w_0, the voltage on the photodiode can be converted to an intensity via the equation

$$I = \frac{V}{GR\pi w_0^2/4} \tag{4.12}$$

from which we can define a conversion factor β as

$$\beta = \frac{1}{GR\pi w_0^2/4}. \tag{4.13}$$

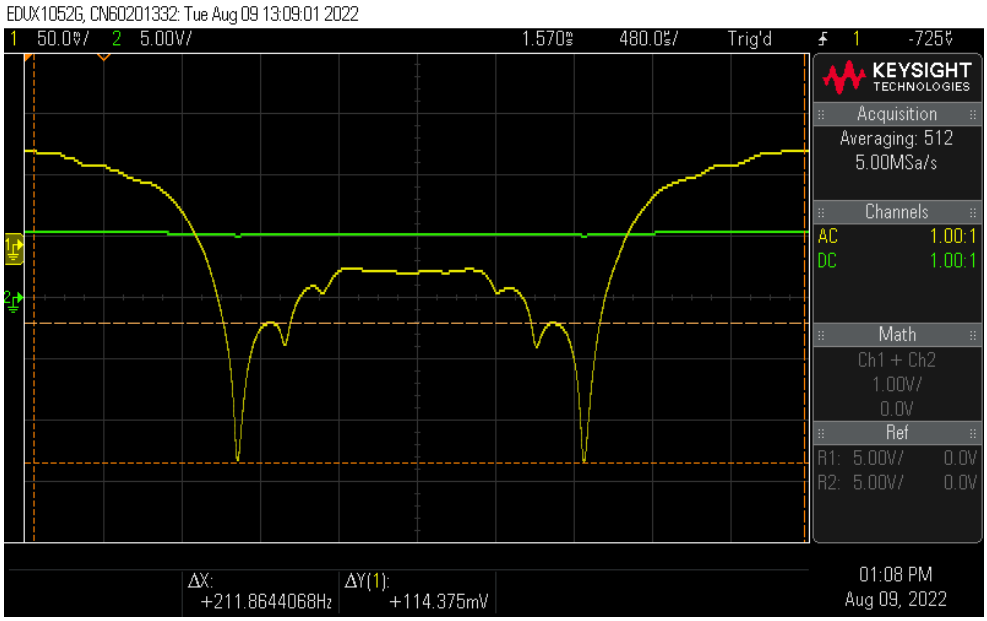

Figure 4.13: The absorption curve at 360°C.
Oscilloscope trace of a crossed-beam spectroscopy measurement. The green line is the DC value incident on the detector, while the yellow curve is alternating current (AC) coupled to show the small variation on top of the DC value. The large dip marked by the y-axis cursors is the $F = 4$ to $F' = 5$ transition while the smaller dips inward correspond to $F' = 4$ and $F =' 3$ respectively.

The exact value of β is not important for the current discussion. This is because the calculation of κ involves a ratio of intensities, so with $I = \beta V$ one can see that the conversion factor will cancel when taking a ratio of two intensities.

For far off resonance light, ω_{FOR}, $\kappa(\omega_{\text{FOR}}) \approx 0$ and so we have $I(\omega_{\text{FOR}}, z) = I_0 = \beta V_{\text{DC}}$. The point on resonance corresponds to the lowest point of the oscilloscope trace, and here we have $I(\omega_0, z) = I_0 \exp(-\kappa(\omega_0) z) = \beta(V_{\text{DC}} - \Delta V)$ where z is the diameter of the atomic beam, which is taken to be the collimated diameter of .25" and ΔV is the difference between the DC voltage and the voltage on resonance[4]. From this we may find the absorptivity as

$$\kappa(\omega_0) = \ln\left(1 - \frac{\Delta V}{V_{\text{DC}}}\right)/z. \tag{4.14}$$

[4]shown as ΔY(1) in Figure 4.13

Temperature (°C)	Flux $10^{11}(s^{-1}cm^{-2})$	Flux % Error
325	1.19	4.6
340	2.65	2.4
350	4.86	1.7
360	8.88	1.4
370	14.4	1.3
380	29.4	1.2

Table 4.2: Flux data.

The atomic density N is related to the absorptivity by

$$N = \frac{\kappa_B(\omega_0)}{\sigma(\omega_0)} \tag{4.15}$$

where $\sigma(\omega_0) = \lambda^2/2\pi \approx 1.2 \times 10^{-9}$ cm^2 is the optical cross section of cesium on resonance with unpolarized light [20]. Finally, the flux Φ effusing from the microchannel nozzle may be calculated by multiplying this density by the most probable velocity v_m given by

$$v_m = \sqrt{2k_BT/m} \tag{4.16}$$

where k_B is the Boltzmann constant, T is the temperature of the gas, and m is the mass of cesium. For the gas at 360°C shown in Figure 4.13, we have

$$\Phi = v_m N = 2.58 \times 10^{12} \frac{\text{atoms}}{\text{s} \cdot \text{cm}^2}. \tag{4.17}$$

The results are summarized in Table 4.2 and Figure 4.14. Extrapolating the data in Table 4.2, the temperature required for a flux of 1×10^{13} atoms s^{-1} cm^{-2} is approximately 400°C. The oven's flux therefore spans 3 orders of magnitude over an 80°C temperature range. In addition to the flux, the degree of collimation can be roughly estimated from Figure 4.13 with the aid of Figure 3.6 and the fact that the $F = 4$ to $F = 5$ transition is separated from the $F = 4$ to $F = 3$ transition by a frequency of 450 MHz [53]. Using this fact, one can deduce that the x-axis spacing in Figure 3.6 corresponds to 450 MHz for every 2.5 gridlines. The FWHM is about 3.5 gridlines, leading to a frequency width of about (3.5/2.5)450 MHz $\approx$ 630 MHz. Using the same trick in Figure 4.13, here 450 MHz corresponds to about one major division. The FWHM of this beam is about one minor division, leading to a frequency spread of (1/4)450 MHz $\approx 110MHz$. The transverse velocity spread has therefore been reduced by the factor 630/110 $\approx$ 6. This however does not account for the different velocities of a room temperature vapor, and the vapor effusing from the nozzle at 360°C. Multiplying by $\sqrt{660/300}$ this leads to a collimation factor of 8.

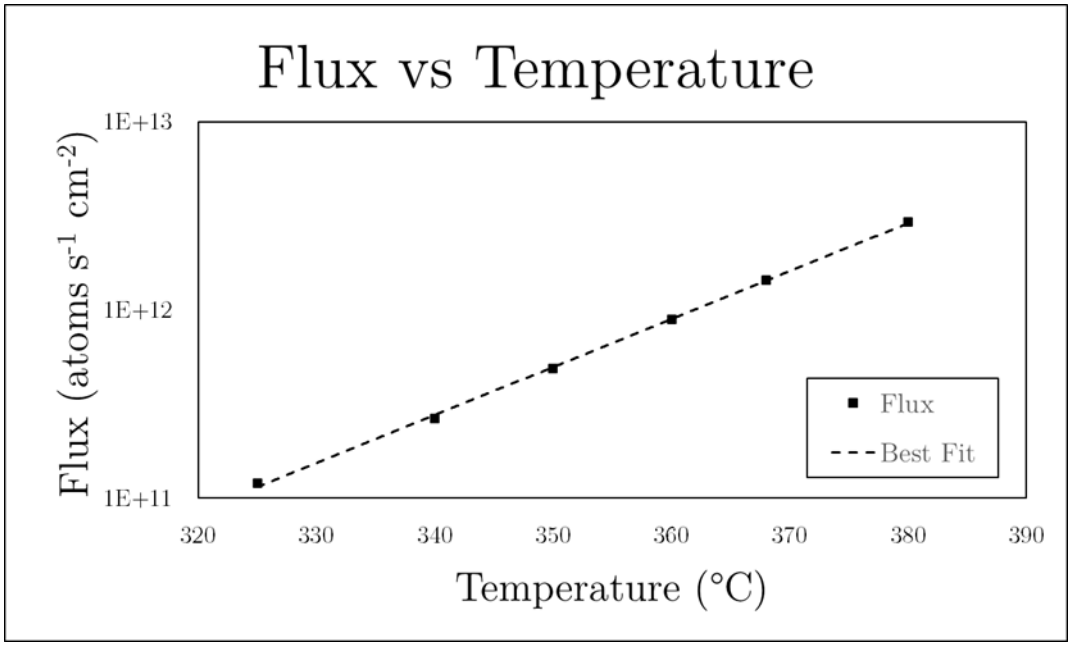

Figure 4.14: Flux vs. temperature.
A semi-log plot of flux vs. temperature. The flux follows an approximately exponential relation to temperature. The best fit curve is given by $\Phi = 589.67 \exp(0.0587T)$ with an R^2 value of 0.999. Error bars are smaller than the squares.

4.4 Summary of Results

A new atomic beam oven has been designed that allows for varying the flux over 3 orders of magnitude within an 80°C temperature range while keeping the exterior of the vacuum chamber below 60°C. The Flux varying so greatly over a small temperature range is very promising. A laser cooling this atomic beam could capture about 1% of the flux, so at 360°C this would result in loading the magneto-optical trap at a rate on the order of 10^9 atoms per second after accounting for imperfect collimation. 10^9 atoms per second is about the slowest we would like to load the MOT, so the data confirms that the flux from the oven can be adjusted to allow for optimal loading. In addition, at 360°C, the exterior of the vacuum chamber reaches a steady state temperature of 43°C which is low enough to prevent air currents from forming.

Chapter 5

Dipole Blockade for Molecular Quantum Computing

The current chapter is a departure from the vacuum technology discussed in the preceding chapters. Now, we take a look forward at one avenue of experimentation we plan to carry out with the chamber once it is assembled. Specifically, using dipole blockade in molecules for quantum computing. Dipole blockade has a rich history of use in quantum computing with neutral atoms[22, 29, 35, 45] and while molecules can also take advantage of dipole blockade [6, 14, 57, 58], there are no experiments to-date that have done so. What follows is a new scheme for performing a two-qubit gate with molecules via dipole blockade, as well as preliminary calculations to determine the fidelity of the gate.

5.1 Dipole Blockade

Dipole blockade occurs when an on resonance laser excites an atom to a state with a large dipole moment which in turns shifts the energy levels of neighboring atoms so greatly they become detuned from resonance with the laser. In atoms this is most commonly done by exciting to a state with a large quantum number (about n=40 or greater), called a Rydberg state. The electron is far enough away from the atom that in a semi-classical picture it can be thought of as a physical dipole. Atoms excited this way are known as Rydberg atoms, and dipole blockades formed in this way are known as Rydberg blockades. This forms the basis for Rydberg atom quantum computing, as Rydberg blockade allows for the performance of CNOT gates. The molecular CNOT gate introduced in this chapter is

based on a Rydberg CNOT gate, and so to aid in discussion, Rydberg CNOT gates will be discussed first.

5.2 Rydberg Atom CNOT gates

This review of Rydberg CNOT gates is largely a summary from Reference [45]. A diagram of the Rydberg CNOT gate is shown in Figure 5.1. A CNOT gate is a specific instance of a more general class of operations called controlled gate operations. Controlled gates use the state of one or more qubits called the control qubits to decide whether or not to perform a gate on a different qubit called the target qubit. A CNOT operation uses one control and one target qubit. If the control qubit is in the state $|1\rangle$, then an X gate is performed on the target qubit. The X gate is given by

$$X = \begin{bmatrix} 0 & 1 \\ 1 & 0 \end{bmatrix} \tag{5.1}$$

in the $\{|0\rangle, |1\rangle\}$ basis. The CNOT gate along with a complete set of single qubit gates forms a universal set of gates [42]. But for Rydberg atoms, it is easier to instead perform a controlled-Z (CZ) gate. Fortunately, the CZ gate can be transformed to a CNOT gate using single qubit operations [42], so it too forms a universal set of gates. Demonstrating the ability for a platform to perform either of these gates is a good first step for demonstrating a platform as viable for quantum computation.

To perform CZ gates with Rydberg atoms, the atoms must first be arranged in such a way that their positions do not drift much, otherwise the researcher could loose track of which atom corresponds to which qubit. This could be done, for instance, by confining the atoms in an optical lattice or holding them in optical tweezers. Next, one must choose which states of the atom to use as $|0\rangle$ and $|1\rangle$. Typically, the $|0\rangle$ and $|1\rangle$ states are encoded in the hyperfine ground state of an alkali atom[45]. Then a CZ gate can be performed on a pair of neighboring atoms using a sequence of three laser pulses, all of which are tuned to the atoms' $|1\rangle \rightarrow |r\rangle$ transition frequency where $|r\rangle$ denotes a Rydberg state. The sequence consists of a π-pulse on the control qubit, a 2π-pulse on the target qubit, then a π-pulse on the control qubit. It is instructive to walk through how this pulse sequence affects a few of the basis states. The two particle states are labeled using the shorthand notation $|\text{control qubit, target qubit}\rangle = |\text{control qubit}\rangle \otimes |\text{target qubit}\rangle$. If we begin in the state $|11\rangle$, the first pulse stimulates the control qubit to the Rydberg state, $|r\rangle$. The control qubit is now blockading the target from also being able to be stimulated to the Rydberg state, and so the 2π-pulse on the target has no effect. The last pulse then brings the control

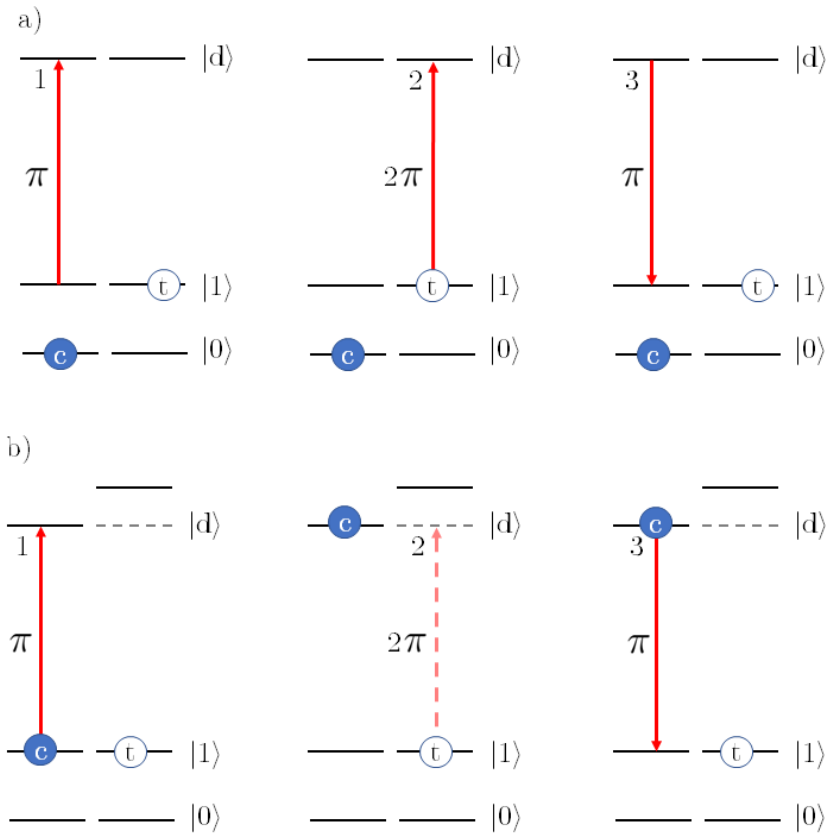

Figure 5.1: Dipole blockade for CNOT gates.
Level diagrams for the control (blue circle labeled "c") and target (white circle labeled "t") qubits during the three-pulse sequence described in Section 5.2. a) Level diagram for the three pulses when in the $|01\rangle$ state 1. A π-pulse is applied to the control qubit. The qubit is in the $|0\rangle$ state and so the laser's frequency is not sufficient to stimulate the atom into the Rydberg state. 2. A 2π pulse is applied to the target qubit which results in the qubit gaining a π phase shift. 3. Another π pulse is applied to the target qubit which has no effect. b) Level diagram for the three pulses when in the $|11\rangle$ state. 1. The control qubit is now in the $|1\rangle$ state and so the π pulse stimulates the qubit into the Rydberg state. 2. The energy needed for the target qubit to transition to the Rydberg state has been increased by the control qubit being in the Rydberg state. The target qubit is thus blocked from also transitioning to the Rydberg state, so the 2π pulse has no effect. 3. A second π pulse is applied to the target atom which brings it back to the ground state.

back from $|r\rangle$ to $|1\rangle$. As a result of this pulse sequence, the state $|11\rangle$ picks up a phase shift of -1. On the other hand, the basis state $|01\rangle$ has the control qubit in the $|0\rangle$ state, and so the first pulse will not stimulate the control qubit into $|r\rangle$, and so no blockade will be present. As a result, the 2π-pulse on the target will effectively stimulate it to the $|r\rangle$ state and back, accumulating a phase shift of -1 in the processes. By similar reasoning, one may work through the other basis states to find that in the basis $\{|00\rangle, |01\rangle, |10\rangle, |11\rangle\}$ the process is described by the transformation

$$CZ_{\mathrm{R}} = \begin{bmatrix} 1 & 0 & 0 & 0 \\ 0 & -1 & 0 & 0 \\ 0 & 0 & -1 & 0 \\ 0 & 0 & 0 & -1 \end{bmatrix}. \tag{5.2}$$

This can be converted to a CZ gate by applying a single-qubit Z gate to both qubits. Thus, the three pulse sequence described can be used to perform a CZ or CNOT gate.

5.3 Molecular CNOT Gate

Like atoms, molecules also benefit from having dipole moments that are highly state dependent. For performing CNOT gates with molecules, the initial configuration is similar. Molecules are distributed in a lattice, and a molecule in a large dipole state, call it $|d\rangle$, is sufficient to produce a dipole blockade on its neighbors, suppressing them from also transitioning to $|d\rangle$ if stimulated by a laser. There are several possibilities for which states of CsLi to use, but the specific choice of states is a subject for future research. The scheme proposed here, however, differs slightly from the gate discussed in Section 5.2. Whereas in the Rydberg atoms case, only the $|1\rangle \to |r\rangle$ transition is addressed, with molecules the $|0\rangle \to |d\rangle$ transition and the $|1\rangle \to |d\rangle$ transition are addressed. The laser tuned to the $|0\rangle \to |d\rangle$ transition has Rabi frequency Ω_0 and the laser tuned to the $|1\rangle \to |d\rangle$ transition has Rabi frequency Ω_1. This three-level system is depicted in Figure 5.2. We need not restrict ourselves however to making our computational states $\{|0\rangle, |1\rangle\}$ hyperfine states of the valence electrons. With molecules, we also have access to rovibrational states, which provide the advantage of being much longer lived generally than the electronic states of atoms.

The CNOT gate also uses a three pulse sequence: The first and third pulses are single photon π-pulses tuned to the $|0\rangle$ to $|d\rangle$ transition and act only on the control qubit. The second pulse is a two photon π-pulse acting on the target only. The two lasers are tuned to the $|0\rangle$ to $|d\rangle$ and $|1\rangle$ to $|d\rangle$ transitions. Without blockade, this pulse has the effect of

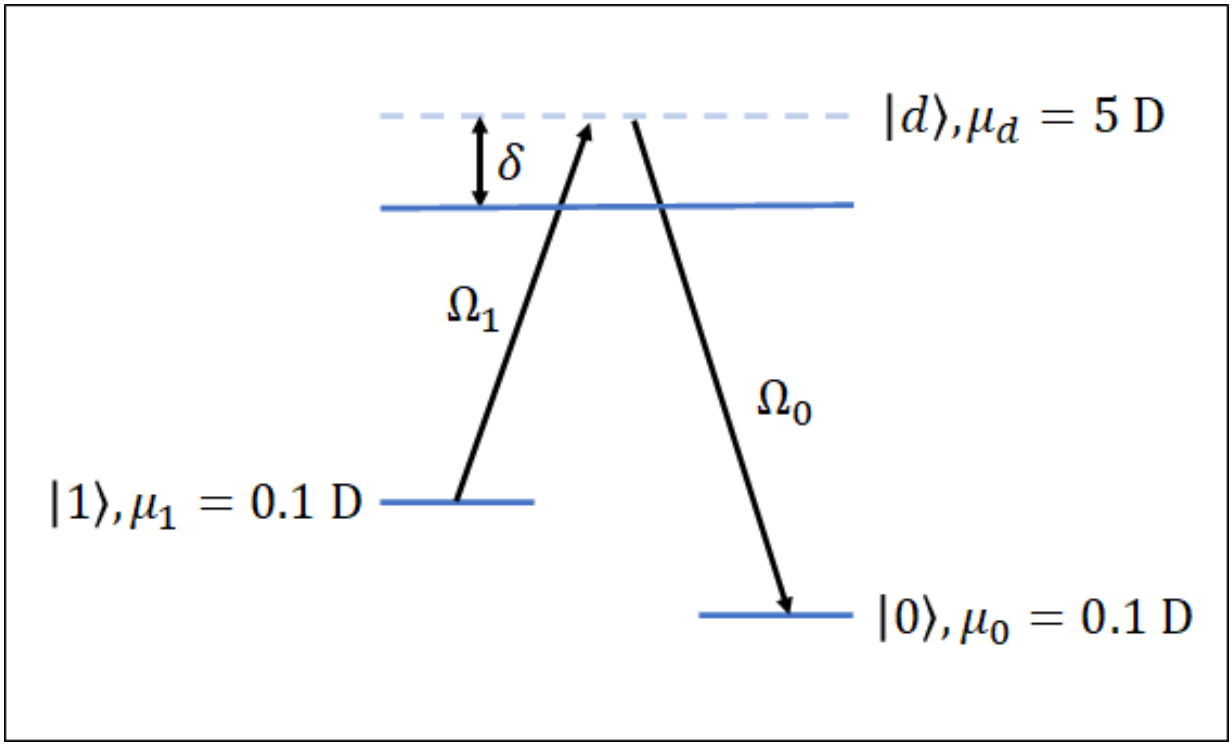

Figure 5.2: Level diagram for dipole blockade interactions with molecules. δ is the energy shift in frequency units produced by the blockade of a neighboring molecule in the dipole state. μ_0, μ_1, and μ_d are the magnitudes of a CsLi molecule's dipole moments in the $|0\rangle$, $|1\rangle$, and $|d\rangle$ states respectively.

swapping the population in $|0\rangle$ with $|1\rangle$ and vice-versa and so performs a NOT operation. With blockade the NOT operation is suppressed, and so the pulse sequence produces a CNOT behavior as desired. The pulse sequence is described in the computational basis by the matrix

$$U_{\mathrm{CNOT}} = \begin{bmatrix} -1 & 0 & 0 & 0 \\ 0 & -1 & 0 & 0 \\ 0 & 0 & 0 & -i \\ 0 & 0 & -i & 0 \end{bmatrix}. \tag{5.3}$$

The phases can be corrected by performing a $\sqrt{\mathrm{Z}}$ gate on the control qubit after this

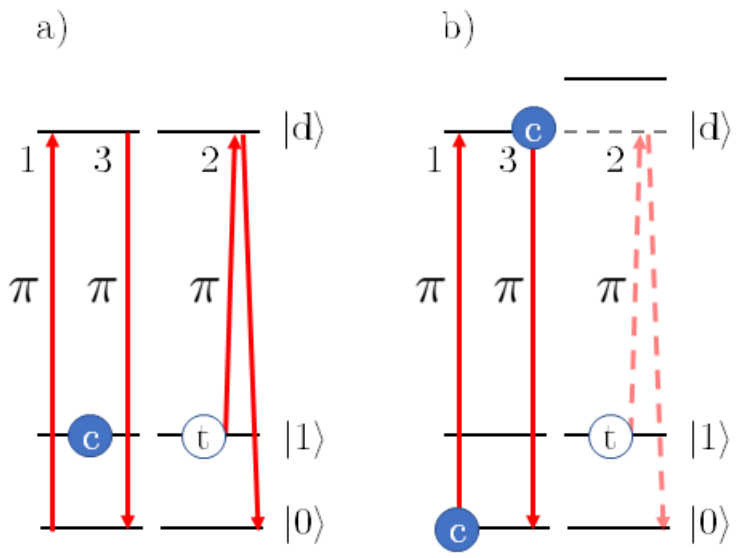

Figure 5.3: Molecular CNOT gate schematic.
a) The CNOT Gate performing a bit flip from $|01\rangle$ to $-|00\rangle$. b) The blockade preventing the bit flip causing the initial state to just collect an overall phase from pulses 1 and 3.

operation. In this basis the $\sqrt{\mathrm{Z}}$ gate acting on just the control qubit is given as

$$\sqrt{\mathrm{Z}} = \begin{bmatrix} 1 & 0 & 0 & 0 \\ 0 & 1 & 0 & 0 \\ 0 & 0 & -i & 0 \\ 0 & 0 & 0 & -i \end{bmatrix}. \tag{5.4}$$

The natural question to ask about Equation 5.3 is then, what is the best possible fidelity that can be achieved?

5.3.1 Fidelity

The purpose of the dipole blockade is to prevent driving the $|0\rangle \rightarrow |1\rangle$ transition (or vice-versa). But the energy shift from the blockade is finite, so a perfect blocking of the transition is impossible. That is, Equation 5.3 is an idealized evolution of the state. In reality, even with the blockade present, there will still be a small probability the target qubit state is flipped. The best possible fidelity can then be characterized as the percentage

of molecules that, beginning in the $|0\rangle$ state, remain there after the CNOT gate. This leads to the equation

$$F = |\langle 0|U'_{\text{CNOT}}|0\rangle|^2 \tag{5.5}$$

where U'_{CNOT} represents not the idealized gate behavior of Equation 5.3 but rather the true behavior of the gate. To find the fidelity, we must determine U'_{CNOT}. This gate is simply the time evolution of the system, and so can be found by determining the system's Hamiltonian. To do this, we begin by first quantifying the blockade's strength. This will lead to a detuning, $\hbar\delta$, and once this is known, the Hamiltonian for the three-level system shown in Figure 5.2 can be derived.

The blockade will cause a detuning, $\hbar\delta$, on its neighbor's $|d\rangle$ state energy level. Specifically, this detuning is the interaction energy between neighboring molecules when both are in the $|d\rangle$ state, which is simply the dipole-dipole interaction energy:

$$\hbar\delta = V_{\text{dd}} = \frac{1}{4\pi\varepsilon_0}\frac{1}{|\mathbf{r}_1 - \mathbf{r}_2|^3}\left[\mathbf{d}_1 \cdot \mathbf{d}_2 - 3(\mathbf{d}_1 \cdot \hat{\mathbf{r}})(\mathbf{d}_2 \cdot \hat{\mathbf{r}})\right] \tag{5.6}$$

where $\mathbf{r_1}$ and $\mathbf{r_2}$ are position vectors from the reference frame's origin to the center-of-mass of the first and second molecule respectively, $\mathbf{d}_1$ and $\mathbf{d}_2$ are the dipole moments of the first and second molecule respectively, and $\hat{\mathbf{r}} = (\mathbf{r}_1 - \mathbf{r}_2)/|\mathbf{r}_1 - \mathbf{r}_2|$. From this equation we can see that the blockade strength is proportional to the dipole moment of both molecules and inversely proportional to the cube of their separation. With CsLi molecules, dipole moments of 5 Debye can be reasonably achieved. Separation is set by the lattice spacing, which the experimenter has a fair degree of control over. We plan to trap the molecules in an optical lattice, and initially, a spacing of $1550/\sqrt{2}$ nm will be used. Eventually this will be decreased to 266 nm. For the latter spacing, The dipole-dipole interaction energy is

$$\delta \approx 200 \text{ kHz}. \tag{5.7}$$

Next, we simply need to incorporate this detuning into a three-level system Hamiltonian, which will be derived in what follows.

We begin by considering an atom rather than a molecule. The atom is a simpler system to begin with, and what is derived carries over to the case of molecules since the transitions in molecular states are also dipole transitions. We start by finding the Hamiltonian of an atom free of any external fields, called the bare state. The eigenstates of the atom's Hamiltonian, by definition, satisfy the eigenvalue equation

$$\hat{H}_0|i\rangle = E_i|i\rangle \tag{5.8}$$

and these states are simply the bare energy states of the atom (or molecule[1]). In addition to this, we must also include the interaction of the atom with laser radiation. The technique is very similar to that outlined in the discussion of two-level systems in Chapter 2, except now we are extending to a three-level system by including two laser frequencies:

$$\mathbf{E} = \mathbf{E}_0/2(\exp(-i\omega_0 t) + \exp(i\omega_0 t)) + \mathbf{E}_1/2(\exp(-i\omega_1 t) + \exp(i\omega_1 t)) \tag{5.9}$$

Using the picture of the atom as a physical dipole, we arrive at the correction to our Hamiltonian as

$$\delta\hat{H}_i = -e\mathbf{r}\cdot\mathbf{E} \tag{5.10}$$

leading us to our full Hamiltonian

$$\hat{H} = \hat{H}_0 + \delta\hat{H} = \hat{H}_0 - e\mathbf{r}\cdot\mathbf{E}_{\text{tot}} = \hat{H}_0 - e\hat{\mathbf{r}}\cdot\mathbf{E}_0\exp^{-i\omega_0 t} - e\hat{\mathbf{r}}\cdot\mathbf{E}_1\exp^{-i\omega_1 t}. \tag{5.11}$$

From here we can calculate how the state $|0\rangle$ changes over time. This is most easily done in matrix form. We will express Equation 5.11 in the eigenbasis of $\hat{H}_0$, and therefore, $\hat{H}_0$ will only contribute diagonal terms. Likewise, due to parity, all diagonal terms of $\delta\hat{H}$ are zero. The off diagonal terms are all of the form

$$H_{ij} = \langle i|\hat{H}|j\rangle = \langle i|e\mathbf{r}\cdot\mathbf{E}_0 e^{i\omega_0 t}|j\rangle + \langle i|e\mathbf{r}\cdot\mathbf{E}_1 e^{i\omega_1 t}|j\rangle \; i \neq j \tag{5.12}$$

and since the Hamiltonian is Hermitian, there are only three independent terms we must calculate: H_{12}, H_{13}, and H_{23}. To cut down on notation, we first define the Rabi frequencies Ω_0 and Ω_1 as

$$\Omega_0 = \frac{\langle 0|\mathbf{r}\cdot\mathbf{E}_0|d\rangle}{\hbar} \tag{5.13}$$

$$\Omega_1 = \frac{\langle 1|\mathbf{r}\cdot\mathbf{E}_1|d\rangle}{\hbar}. \tag{5.14}$$

All other inner products of this form are so far off resonance that they are effectively zero. Now we may calculate the necessary matrix elements:

$$H_{12} = \hbar(\Omega_0/2)(e^{i\omega_0 t} + e^{-i\omega_0 t}) \tag{5.15}$$

$$H_{13} = 0 \tag{5.16}$$

$$H_{23} = \hbar(\Omega_1/2)(e^{-i\omega_1 t} + e^{i\omega_1 t}) \tag{5.17}$$

[1]For CsLi molecules these energy states have been measured [52]; however, for our purposes we will need to measure these states more precisely.

thus leading to the perturbing Hamiltonian

$$\delta\hat{H} = \hbar \begin{bmatrix} 0 & \frac{\Omega_0}{2}(e^{i\omega_0 t} + e^{-i\omega_0 t}) & 0 \\ \frac{\Omega_0}{2}(e^{-i\omega_0 t} + e^{i\omega_0 t}) & 0 & \frac{\Omega_1}{2}(e^{i\omega_1 t} + e^{-i\omega_1 t}) \\ 0 & \frac{\Omega_1}{2}(e^{-i\omega_1 t} + e^{i\omega_1 t}) & 0 \end{bmatrix}. \tag{5.18}$$

We can again use the trick of redefining our zero-point energy to be the $|0\rangle$ level's energy, then make a transformation into the interaction picture, apply the rotating wave approximation, and transform back. The result is that the perturbing Hamiltonian may be approximated as:

$$\delta\hat{H} \approx \delta\hat{H}' = \hbar \begin{bmatrix} 0 & \frac{\Omega_0}{2}e^{i\omega_0 t} & 0 \\ \frac{\Omega_0}{2}e^{-i\omega_0 t} & 0 & \frac{\Omega_1}{2}e^{-i\omega_1 t} \\ 0 & \frac{\Omega_1}{2}e^{i\omega_1 t} & 0 \end{bmatrix} \tag{5.19}$$

The full Hamiltonian under this approximation is then

$$\hat{H}' = \hbar \begin{bmatrix} 0 & \frac{\Omega_0}{2}e^{i\omega_0 t} & 0 \\ \frac{\Omega_0}{2}e^{-i\omega_0 t} & \omega_{\mathrm{d}0} & \frac{\Omega_1}{2}e^{-i\omega_1 t} \\ 0 & \frac{\Omega_1}{2}e^{i\omega_1 t} & \omega_{10} \end{bmatrix} \tag{5.20}$$

where we have defined the transition frequencies as follows

$$\omega_{\mathrm{d}0} = (E_{\mathrm{d}} - E_0)/\hbar \tag{5.21}$$

$$\omega_{10} = (E_1 - E_0)/\hbar. \tag{5.22}$$

Finally, we can move to the dressed atom picture using the unitary transformation $\hat{U}$ as

$$\hat{U} = \begin{bmatrix} 1 & 0 & 0 \\ 0 & e^{-i\omega_0 t} & 0 \\ 0 & 0 & e^{-i(\omega_0 - \omega_1)t} \end{bmatrix}. \tag{5.23}$$

As in Chapter 2, making the transformation amounts to

$$\hat{H}' \to \hat{U}^\dagger \hat{H}' \hat{U} - i\hbar \hat{U}^\dagger \frac{d\hat{U}}{dt}. \tag{5.24}$$

which leads to

$$\hat{H} = \hbar \begin{bmatrix} 0 & \frac{\Omega_0}{2} & 0 \\ \frac{\Omega_0}{2} & \omega_{\mathrm{d}0} - \omega_0 & \frac{\Omega_1}{2} \\ 0 & \frac{\Omega_1}{2} & \omega_{01} - \omega_0 + \omega_1 \end{bmatrix}. \tag{5.25}$$

We can rewrite the laser frequencies ω_0 and ω_1 in terms of their detunings from the transitions they address. For our present purposes the detunings are the same, labeled as δ so we have $\omega_0 = (E_\mathrm{d} - E_0)/\hbar + \delta$ and $\omega_1 = (E_\mathrm{d} - E_1)/\hbar + \delta$. Substituting these expressions in along with Equation 5.21 leads to the final Hamiltonian:

$$\hat{H} = \hbar \begin{bmatrix} 0 & \frac{\Omega_0}{2} & 0 \\ \frac{\Omega_0}{2} & -\delta & \frac{\Omega_1}{2} \\ 0 & \frac{\Omega_1}{2} & 0 \end{bmatrix}. \tag{5.26}$$

Using standard techniques, this Hamiltonian can be solved for its eigenvalues which are

$$\lambda_0 = 0 \tag{5.27a}$$

$$\lambda_\pm = \hbar \frac{-\delta \pm \sqrt{\delta^2 + \Omega_0^2 + \Omega_1^2}}{2} \tag{5.27b}$$

and its normalized eigenvectors

$$|\lambda_0\rangle = \frac{1}{\sqrt{\Omega_0^2 + \Omega_1^2}} \begin{bmatrix} \Omega_1 \\ 0 \\ -\Omega_0 \end{bmatrix} \tag{5.28a}$$

$$|\lambda_\pm\rangle = \frac{1}{\sqrt{\Omega_0^2 + \Omega_1^2 + \frac{1}{(\lambda_\pm + \delta)^2}\left(\frac{\Omega_0^2}{2} + \frac{\Omega_1^2}{2}\right)^2}} \begin{bmatrix} \Omega_0 \\ \frac{\pm 1}{\lambda_\pm + \delta}\left(\frac{\Omega_0^2}{2} + \frac{\Omega_1^2}{2}\right) \\ \Omega_1 \end{bmatrix}. \tag{5.28b}$$

With this we are now ready to calculate the fidelity Equation 5.5. We begin by expanding $|0\rangle$ in the eigenbasis,

$$|0\rangle = |\lambda_0\rangle\langle\lambda_0|0\rangle + |\lambda_+\rangle\langle\lambda_+|0\rangle + |\lambda_-\rangle\langle\lambda_-|0\rangle, \tag{5.29}$$

and its time evolution can be found by applying the time-evolution operator:

$$\begin{aligned} |0(t)\rangle = \hat{U}(t)|0\rangle &= \exp\left(-\frac{i\hat{H}t}{\hbar}\right)|0\rangle \\ &= \exp\left(-\frac{i\hat{H}t}{\hbar}\right)\left(|\lambda_0\rangle\langle\lambda_0|0\rangle + |\lambda_+\rangle\langle\lambda_+|0\rangle + |\lambda_-\rangle\langle\lambda_-|0\rangle\right) \\ &= |\lambda_0\rangle\langle\lambda_0|0\rangle + \exp\left(-\frac{i\lambda_+ t}{\hbar}\right)|\lambda_+\rangle\langle\lambda_+|0\rangle + \exp\left(-\frac{i\lambda_- t}{\hbar}\right)|\lambda_-\rangle\langle\lambda_-|0\rangle. \end{aligned} \tag{5.30}$$

The first term in the final equality follows from $\lambda_0 = 0$. From here, we may determine the probability that a molecule initially in the $|0\rangle$ state is later measured in the $|1\rangle$ state by projecting onto $|0\rangle$ and squaring:

$$\begin{aligned} P(0 \mid 0) = |\langle 0|0(t)\rangle|^2 =& |\langle 0|\lambda_0\rangle|^4 + |\langle 0|\lambda_+\rangle|^4 + |\langle 0|\lambda_-\rangle|^4 \\ &+ 2|\langle 0|\lambda_0\rangle|^2\langle 0|\lambda_+\rangle|^2 \cos\left(\frac{\lambda_+}{\hbar}t\right) \\ &+ 2|\langle 0|\lambda_0\rangle|^2|\langle 0|\lambda_-\rangle|^2 \cos\left(\frac{\lambda_-}{\hbar}t\right) \\ &+ 2|\langle 0|\lambda_+\rangle|^2|\langle 0|\lambda_-\rangle|^2 \cos\left(\frac{\lambda_+ - \lambda_-}{\hbar}t\right). \end{aligned} \tag{5.31}$$

For the sake of compactness we define the following constants:

$$A = |\langle 0|0(t)\rangle|^2 = |\langle 0|\lambda_0\rangle|^4 + |\langle 0|\lambda_+\rangle|^4 + |\langle 0|\lambda_-\rangle|^4 \tag{5.32a}$$
$$B = 2|\langle 0|\lambda_0\rangle|^2\langle 0|\lambda_+\rangle|^2 \tag{5.32b}$$
$$C = 2|\langle 0|\lambda_0\rangle|^2|\langle 0|\lambda_-\rangle|^2 \cos\left(\frac{\lambda_-}{\hbar}t\right) \tag{5.32c}$$
$$D = 2|\langle 0|\lambda_+\rangle|^2|\langle 0|\lambda_-\rangle|^2 \cos\left(\frac{\lambda_+ - \lambda_-}{\hbar}t\right) \tag{5.32d}$$
$$\omega_{\mathrm{B}} = \lambda_+/\hbar \tag{5.32e}$$
$$\omega_{\mathrm{C}} = \lambda_-/\hbar \tag{5.32f}$$
$$\omega_{\mathrm{D}} = (\lambda_+ - \lambda_-)/\hbar \tag{5.32g}$$
$$\tag{5.32h}$$

so that Equation 5.31 may be written as

$$|\langle 0|0(t)\rangle|^2 = A + B\cos(\omega_{\mathrm{B}}t) + C\cos(\omega_{\mathrm{C}}t) + D\cos(\omega_{\mathrm{D}}t). \tag{5.33}$$

An analogous procedure may be performed to find $|\langle 1|0(t)\rangle|^2$ and $|\langle d|0(t)\rangle|^2$, and then the populations of the states may be calculated over time[2]. With this equation now derived, it is instructive at this point to pause and consider the dynamics of the gate with and without blockade. Note that in Equation 5.33, the amplitudes and frequencies are implicitly dependent on δ and so will yield a different equation with and without blockade. The two

[2]In fact, only one of these two additional values needs to be calculated since $|\langle 0|0(t)\rangle|^2 + |\langle 1|0(t)\rangle|^2 + |\langle d|0(t)\rangle|^2 = 1$.

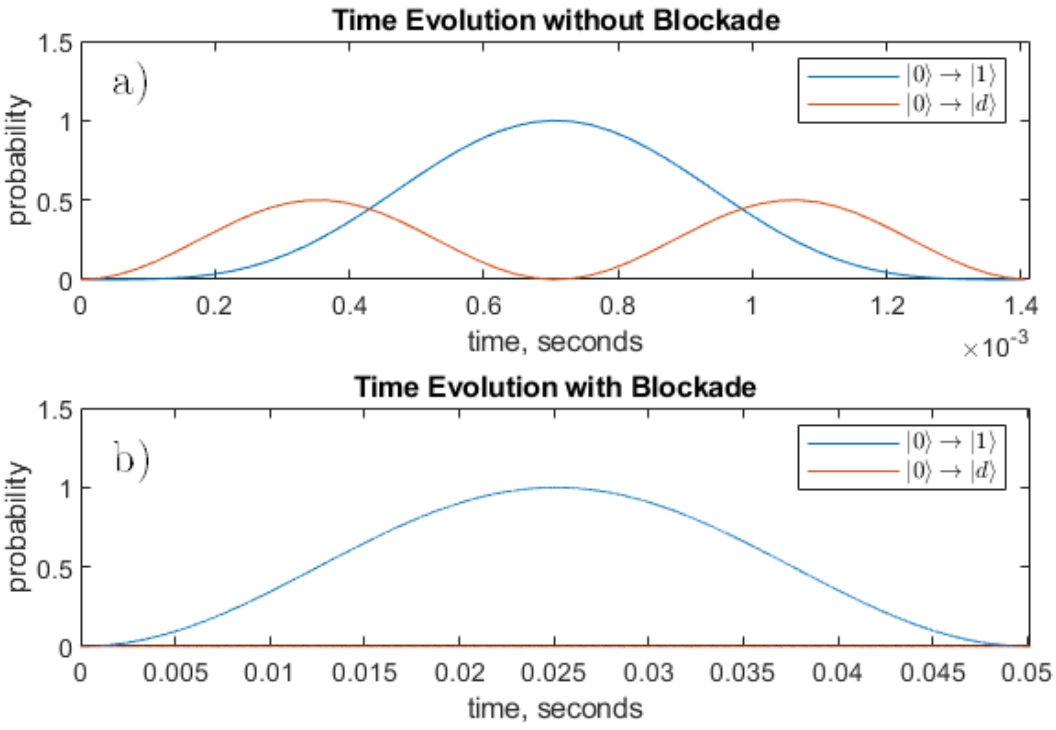

Figure 5.4: Rabi oscillations of a molecule initially in the $|0\rangle$ state.
Note the different time scales between the two plots. The blockade has two effects: it greatly reduces the population transfer to $|d\rangle$, and it slows down the rate of transfer to $|1\rangle$. a) Oscillations without blockade. b) Oscillations with blockade.

cases are plotted over time in Figure 5.4. The figure shows that the blockade has the effect of both suppressing the $|0\rangle$ to $|d\rangle$ transition, as well as slowing down the rate of transfer to $|1\rangle$ by several orders of magnitude.

To finish finding the fidelity, we need to know what value to use for t in Equation 5.33 when the blockade is present. We are interested in how the $|0\rangle$ state is affected by a CNOT gate, so the time to use is the time for a CNOT gate. The CNOT gate time is the time it takes for 100% population transfer from $|0\rangle$ to $|1\rangle$ *without* blockade (i.e. with $\delta = 0$). Thus, we must set Equation 5.33 equal to unity and solve for t for the case $\delta = 0$. We can then substitute this time into Equation 5.33 for the case $\delta \neq 0$. At this point we shall take $\Omega_0 = \Omega_1$ because the transition will be limited by the slowest Rabi frequency, while having different Rabi frequencies will lead to the larger contributing additional stark shifts with no benefit. Now the eigenvalues and eigenvectors simplify to

$$\lambda_{\pm} = \pm\frac{\Omega_0}{\sqrt{2}} \tag{5.34a}$$

$$|\lambda_0\rangle = \frac{1}{\sqrt{2}}\begin{bmatrix} 1 \\ 0 \\ -1 \end{bmatrix} \tag{5.34b}$$

$$|\lambda_{\pm}\rangle = \frac{1}{2}\begin{bmatrix} 1 \\ \pm\sqrt{2} \\ 1 \end{bmatrix} \tag{5.34c}$$

from which it follows that Equation 5.33 becomes

$$|\langle 1|\hat{U}(t)|0\rangle|^2 = 1 = \frac{1}{4}\left[\cos\left(\frac{\Omega_0}{\sqrt{2}}t_{\mathrm{G}}\right) - 1\right]^2 \tag{5.35}$$

where t_{G} is the gate time, which is the minimum value of t needed for Equation 5.33 to equal unity. Solving Equation 5.35 leads to the gate time

$$t_{\mathrm{G}} = \frac{\sqrt{2}\pi}{\Omega_0} \tag{5.36}$$

which is the length of a π-pulse to drive $|0\rangle$ to $|1\rangle$. The gate time is therefore a function purely of the Rabi frequency.

From here all that's left is to substitute the gate time t_{G} back into Equation 5.33 for a given δ and Ω_0. However, before doing so, Equation 5.33 can be simplified even further for the case $\delta \neq 0$. We begin by noticing that the cosines' frequencies are the differences

of the energy eigenvalues from Equation 5.27. In the case $\delta \gg \Omega_0, \Omega_1$ the eigenvalues may be simplified by a perturbative expansion in Ω^2/δ. For our purposes this is justified as $\delta \sim \mathcal{O}(10^5)$ Hz while $\Omega \sim \mathcal{O}(10^3)$ Hz. The eigenvalues then become (continuing to assume $\Omega_0 = \Omega_1$)

$$\lambda_+ = \hbar \frac{\Omega_0^2}{2\delta} \tag{5.37a}$$

$$\lambda_- = \hbar \left(-\delta + \frac{\Omega_0^2}{2\delta} \right) \tag{5.37b}$$

and so the frequencies (Equation 5.32) reduce to

$$\omega_{\mathrm{B},\delta\neq 0} = \lambda_+/\hbar = \frac{\Omega_0^2}{2\delta} \tag{5.38a}$$

$$\omega_{\mathrm{C},\delta\neq 0} = \lambda_-/\hbar = -\delta + \frac{\Omega_0^2}{2\delta} \tag{5.38b}$$

$$\omega_{\mathrm{D},\delta\neq 0} = (\lambda_+ - \lambda_-)/\hbar = \delta. \tag{5.38c}$$

Multiplying these frequencies by the gate time t_G, we see a separation in scale between the frequencies:

$$\omega_{\mathrm{B},\delta\neq 0} t_\mathrm{G} = \frac{\pi}{\sqrt{2}} \frac{\Omega_0}{\delta} \tag{5.39a}$$

$$\omega_{\mathrm{C},\delta\neq 0} t_\mathrm{G} = \sqrt{2}\pi \frac{\delta}{\Omega_0} + \frac{\pi}{\sqrt{2}} \frac{\Omega_0}{\delta} = -\sqrt{2}\pi \frac{\delta}{\Omega_0} \left(1 - \frac{1}{2} \frac{\Omega_0^2}{\delta^2} \right) \approx -\sqrt{2}\pi \frac{\delta}{\Omega_0} \tag{5.39b}$$

$$\omega_{\mathrm{D},\delta\neq 0} t_\mathrm{G} = \sqrt{2}\pi \frac{\delta}{\Omega_0}. \tag{5.39c}$$

Since $\delta \gg \Omega_0$, this shows that over the duration of a π-pulse, $\omega_{\mathrm{C},\delta\neq 0}$ and $\omega_{\mathrm{D},\delta\neq 0}$ will oscillate many times and hence average to zero while $\omega_{\mathrm{B},\delta\neq 0}$ will not. We can therefore drop the last two terms from Equation 5.33. Finally, the amplitudes A and B in this approximation become

$$A = B = \frac{1}{2} \left(1 - \frac{\Omega_0^2}{2\delta} \right) \tag{5.40}$$

$$\tag{5.41}$$

therefore the fidelity simplifies to

$$F = |\langle 0|\hat{U}(t)|0\rangle|^2 = A(1 + \cos \omega_{\mathrm{B},\delta\neq 0} t_\mathrm{G}) = \left(1 - \frac{\Omega_0^2}{2\delta^2} \right) \cos^2 \left(\frac{\Omega_0^2}{4\delta} t_G \right). \tag{5.42}$$

We are interested in how the imperfection of the blockade degrades the performance of the gate, so it is helpful to recast this into the infidelity of the gate $\mathcal{F} = 1 - F$. Substituting in the gate time (Equation 5.36), we arrive at the infidelity equation for strong blockade:

$$\mathcal{F} = \frac{\Omega_0^2}{2\delta^2} + \left(1 - \frac{\Omega_0^2}{2\delta^2}\right) \sin^2\left(\frac{\pi}{2\sqrt{2}} \frac{\Omega_0}{\delta}\right). \tag{5.43}$$

We can see that the infidelity is dependent on both the strength of the blockade, and the speed of the Rabi frequency. The experimenter has some control over both these parameters: the Rabi frequency is dependent on the intensity of the laser, and the blockade strength is dependent on the spacing of the molecules, increasing as the spacing is decreased. Figure 5.5 plots the infidelity of the gate against gate time for several different lattice spacings. The bottom right panel of Figure 5.5 shows that a gate time of less than 2 ms is possible with a fidelity of 99.9%.

This is only a best possible fidelity, and ignores many degrading factors from the experiment such as: scattering of light from the trap, collisions with background gas particles, scattering of blackbody radiation, and uncontrolled external fields. Future work in the group will aim to quantify the performance of this CNOT gate, and these factors will need to be taken into consideration as well. Nonetheless, these calculations show that the technique of dipole blockade can be extended for use in molecular quantum computing. Molecules offer a nice trade-off between interaction strength and storage state lifetime. Like neutral atoms, molecules' interactions can be turned on and off as needed. Unlike atoms, the computational states' natural lifetime is not a limitation compared to decoherence due to the scattering of trapping light.

In conclusion, a new vacuum system has been designed that is predicted to allow for loading a MOT in one second. Future work is planned to test the load time. The collimation of the beam reduces the frequency of oven changes, allowing for less down-time of the apparatus and so more time collecting data. In addition, atomic beams of lithium and cesium can be produced with minimal temperature increase of the exterior vacuum chamber or surrounding air and optics. This allows for optics to be more precisely fine tuned and remain aligned. The design of the apparatus allows for great optical access to the main chamber where experiments will be performed, and hence allows for a wide array of experiments to be carried out.

One avenue of experimentation to be performed with this machine is dipole blockade and CNOT gates with molecules. The method given here is predicted to have a fidelity of 99.9% with a gate time as low as 2 ms. The method is based on a three-level approximation, and is dependent on the dipole-dipole interaction between two neighboring

molecules, and the two-photon Rabi frequency of the $|0\rangle$ to $|1\rangle$ transition. Future work will require incorporating more degrading factors to the fidelity as discussed in the previous paragraph.

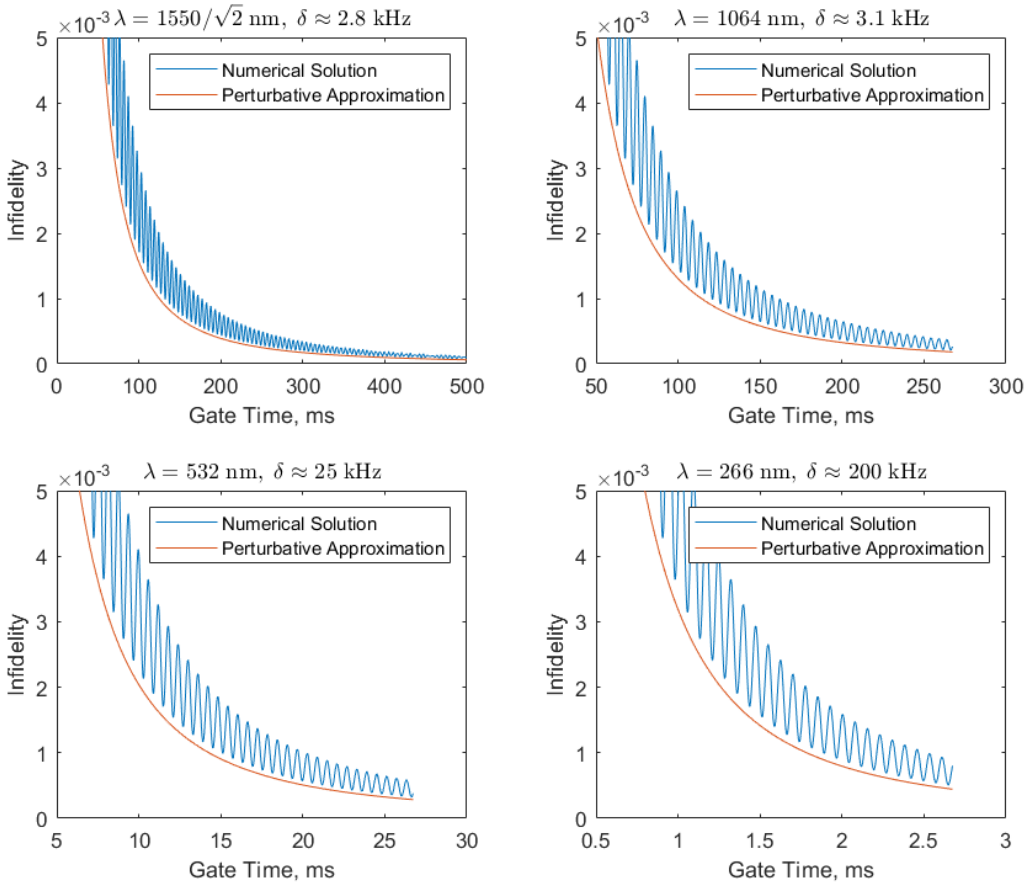

Figure 5.5: Infidelities vs. gate time.
Each panel shows the infidelity vs. gate time for a different blockade strength which is determined by the lattice spacing, λ. These plots are of Equation 5.43, made by finding the infidelity vs. Rabi frequency, and then converting the x-axis to time through Equation 5.36 since the gate time is defined by the Rabi frequency and has a one-to-one correspondence. As the lattice spacing decreases the blockade strength increases, leading to faster gate times for comparable infidelity.

References

[1] *Metallic Materials Properties Development and Standardization (MMPDS-11)*. Battelle Memorial Institute, 2016.

[2] *Dimensioning and Tolerancing*. American Society of Mechanical Engineers, Two Park Avenue, New York, NY 10016, Y14.5-2018 edition, 2019.

[3] W. E. Acree Jr. and J. S. Chickos. *NIST Chemistry WebBook, NIST Standard Reference Database Number 69, Editors P. J. Linstrom and W. G. Mallard*. National Institute of Standards and Technology, Gaithersburg MD, 20899, 2022.

[4] M. H. Anderson, J .R. Ensher, M. R. Matthews, C. E. Wieman, and E. A. Cornell. Observation of Bose-Einstein condensation in a dilute atomic vapor. *Science*, 269(5221):198–201, 1995.

[5] P. W. Atkins and L. Jones. *Chemical principles: the quest for insight*. W.H. Freeman, New York, fifth edition edition, 2010.

[6] A. Barenco, D. Deutsch, A. Ekert, and R. Jozsa. Conditional quantum dynamics and logic gates. *Phys. Rev. Lett.*, 74:4083–4086, May 1995.

[7] C. H. Bennett and G. Brassard. Quantum cryptography: Public key distribution and coin tossing. *Proceedings of IEEE International Conference on Computers, Systems and Signal Processing*, pages 8–13, 1984.

[8] I. I. Beterov, I. I. Ryabtsev, D. B. Tretyakov, and V. M. Entin. Quasiclassical calculations of blackbody-radiation-induced depopulation rates and effective lifetimes of Rydberg ns, np, and nd alkali-metal atoms with n $leq80$. *Physical review A*, 79(5):052504, 2009.

[9] G. C. Bjorklund, M. D. Levenson, W. Lenth, and C. Ortiz. Frequency modulation (fm) spectroscopy. *Applied Physics B*, 32:145–152, Nov 1983.

[10] K. G. Budinski. *Engineering materials: properties and selection*. Prentice Hall, Englewood Cliffs, N.J, fourth edition edition, 1992.

[11] W. D. Callister. *Fundamentals of materials science and engineering: an integrated approach*. Wiley, Hoboken, NJ, fourth edition edition, 2012.

[12] A. H. Carter. *Classical and statistical thermodynamics*. Prentice Hall, Upper Saddle River, N.J, 2001.

[13] C. Cohen-Tannoudji. *Advances in atomic physics: an overview*. World Scientific, Singapore, 2011.

[14] D. DeMille. Quantum computation with trapped polar molecules. *Phys. Rev. Lett.*, 88:067901, Jan 2002.

[15] W. Demtroder. *Laser Spectroscopy: Basic Concepts and Insrumentation*. Springer, 2010.

[16] D. P. DiVincenzo. The physical implementation of quantum computation. *Fortschritte der Physik: Progress of Physics*, 48(9-11):771–783, 2000.

[17] A. Einstein. Quantentheorie des einatomigen idealen gases. zweite abhandlung. *Akademie-Vorträge: Sitzungsberichte der Preußischen Akademie der Wissenschaften 1914–1932*, pages 245–257, 2005.

[18] R. P. Feynman. Simulating physics with computers. *International Journal of Theoretical Physics*, 21:467–488, June 1982.

[19] R. P. Feynman. Quantum mechanical computers. *Foundations of Physics*, 16:507–531, June 1986.

[20] C. J. Foot. *Atomic physics*. Oxford master series in physics; 7. Atomic, optical, and laser physics. Oxford University Press, Oxford, 2005.

[21] J. M. Gere and B. J. Goodno. *Mechanics of materials.* Cengage Learning, Stamford, CT, USA, eighth edition edition, 2013.

[22] T. M. Graham, Y. Song, J. Scott, C. Poole, L. Phuttitarn, K. Jooya, P. Eichler, X. Jiang, A. Marra, B. Grinkemeyes, M. Kwon, M. Ebert, J. Cherek, M. T. Lichtman, M. Gillette, J. Gilbert, D. Bowman, T. Ballance, C. Campbell, E. D. Dahl, O. Crawford, N. S. Blunt, T. Noel, and M. Saffman. Multi-qubit entanglement and algorithms on a neutral-atom quantum computer. *Nature Physics*, 604:457–462, Apr 2022.

[23] M. Greiner, O. Mandel, T. Esslinger, T. W. Hänsch, and I. Bloch. Quantum phase transition from a superfluid to a mott insulator in a gas of ultracold atoms. *Nature*, 415:39–44, Jan 2002.

[24] D. J. Griffiths. *Introduction to quantum mechanics*. Prentice Hall, Englewood Cliffs, NJ, 1995.

[25] L. K. Grover. A fast quantum mechanical algorithm for database search. In *Proceedings of the twenty-eighth annual ACM symposium on Theory of computing*, pages 212–219, 1996.

[26] L. Hackspill. Sur une nouvelle préparation du rubidium et du caesium. *Comptes rendus hebdomadaires des séances de l'Académie des sciences*, pages 106–107, 1905.

[27] Omar Hussein. [omar's thesis title]. Master's thesis, University of Waterloo, Ontario, 2022.

[28] F. P. Incropera. *Fundamentals of heat and mass transfer*. John Wiley, Hoboken, NJ, sixth edition edition, 2007.

[29] D. Jaksch, J. I. Cirac, P. Zoller, S. L. Rolston, R. Côté, and M. D. Lukin. Fast quantum gates for neutral atoms. *Phys. Rev. Lett.*, 85:2208–2211, Sep 2000.

[30] Alan Jamison. personal communication.

[31] J. I. Kroschwitz and A. Seidel, editors. *Kirk-Othmer encyclopedia of chemical technology*. Wiley-Interscience, Hoboken, N.J, fifth edition edition, 2004.

[32] M. Lepers, R. Vexiau, M. Aymar, N. Bouloufa-Maafa, and O. Dulieu. Long-range interactions between polar alkali-metal diatoms in external electric fields. *Physical Review A*, 88(3):032709, 2013.

[33] Leonid Lerner. *Small-scale synthesis of laboratory reagents with reaction modeling*. CRC Press, Boca Raton, Fla, 2011.

[34] J.-R. Li, W. G. Tobias, K. Matsuda, C. Miller, G. Valtolina, L. De Marco, R. R. W. Wang, L. Lassablière, G. Quéméner, J. L. Bohn, and J. Ye. Tuning of dipolar interactions and evaporative cooling in a three-dimensional molecular quantum gas. *Nature Physics*, 17:1144–1148, Oct 2021.

[35] M. D. Lukin, M. Fleischhauer, R. Cote, L. M. Duan, D. Jaksch, J. I. Cirac, and P. Zoller. Dipole blockade and quantum information processing in mesoscopic atomic ensembles. *Phys. Rev. Lett.*, 87:037901, Jun 2001.

[36] S. Majidy, C. Wilson, and R. Laflamme. *An Introduction to Building Quantum Computers*. pre-print, 2022.

[37] E. J. Manista and J. W. Sheldon. Atomic beam determination of the cesium-cesium total scattering cross section. Technical report, National Aeronautics and Space Administration, 1965.

[38] A. Mazurenko, C. S. Chiu, G. Ji, M. F. Parsons, M. Kanász-Nagy, R. Schmidt, F. Grusdt, E. Demler, D. Greif, and M. Greiner. A cold-atom fermi–hubbard antiferromagnet. *Nature*, 545(7655):462–466, 2017.

[39] H. J. Metcalf and P. van der Straten. *Laser Cooling and Trapping*. Springer, 1999.

[40] I. J. Nagrath and M. Gopal. *Control systems engineering*. New Age International P Ltd., New Delhi, fifth edition edition, 2009 - 2007.

[41] K.-K. Ni, S. Ospelkaus, M. H. G. de Miranda, A. Pe'er, B. Neyenhuis, J. J. Zirbel, , S. Kotochigova, P. S. Julienne, D. S. Jin, and J. Ye. A high phase-space-density gas of polar molecules. *Science*, 322:231–235, Oct 2008.

[42] M. A. Nielsen and I. L. Chuang. *Quantum Computation and Quantum Information*. Cambridge University Press, Cambridge, United Kingdom, tenth anniversary edition edition, 2019.

[43] J. F. O'Hanlon. *A User's Guide to Vacuum Technology*. John Wiley and Sons Inc., Hoboken, New Jersey, third edition edition, 2003.

[44] N. Ramsey. *Molecular beams*. Oxford classic texts in the physical sciences. Clarendon Press, Oxford, 2005 - 1956.

[45] M. Saffman, T. G. Walker, and K. Mølmer. Quantum information with Rydberg atoms. *Rev. Mod. Phys.*, 82:2313–2363, Aug 2010.

[46] J. J. Sakurai. *Modern Quantum Mechanics*. Cambridge University Press, Cambridge, United Kingdom, second edition. edition, 2017 - 2011.

[47] F. C. Schmidt, F. J. Studer, and J. Sottysiak. Heats of solution and heats of reaction in liquid ammonia. v. 1 the alkali and alkaline earth metals. *Journal of the American Chemical Society*, 60(11):2780–2782, 1938.

[48] P. H. Schmidt. The purification of cesium and rubidium metals by chloride reduction under high vacuum conditions. *Journal of The Electrochemical Society*, 116(9):1279, 1969.

[49] R. Senaratne, S. V. Rajagopal, Z. A. Geiger, K. M. Fujiwara, V. Lebedev, and D. M. Weld. Effusive atomic oven nozzle design using an aligned microcapillary array. *Review of Scientific Instruments*, 86(2):023105, 2015.

[50] P. W. Shor. Algorithms for quantum computation: discrete logarithms and factoring. In *Proceedings 35th annual symposium on foundations of computer science*, pages 124–134. IEEE, 1994.

[51] J. Singh, P. A. M. Dolph, and W. A. Tobias. Alkali metal vapor pressures & number densities for hybrid spin exchange optical pumping. *University of Virgina*, 2008.

[52] P. Staanum, A. Pashov, H. Knöckel, and E. Tiemann. $x\,^1\Sigma^+$ and $a\,^3\Sigma^+$ states of LiCs studied by Fourier-transform spectroscopy. *Phys. Rev. A*, 75:042513, Apr 2007.

[53] Daniel A Steck. Cesium d line data. 2003.

[54] D. R. Stull. Vapor pressure of pure substances. Organic and inorganic compounds. *Industrial & Engineering Chemistry*, 39(4):517–540, 1947.

[55] F. Top. *p-wave Collisions in Ultracold Fermions*. PhD thesis, Massachusetts Institute of Technology, Cambridge, MA, 2020.

[56] E. Urban, T. Johnson, T. Henage, L. Isenhower, D. D. Yavuz, T. Walker, and M. Saffman. Observation of Rydberg blockade between two atoms. *Nature Physics*, 5:110–114, Feb 2009.

[57] B. Yan, S. A. Moses, B. Gadway, J. P. Covey, K. R. A. Hazzard, A. M. Rey, D. S. Jin, and J. Ye. Observation of dipolar spin-exchange interactions with lattice-confined polar molecules. *Nature*, 501:521–525, Sep 2013.

[58] S. F. Yelin, K. Kirby, and Robin Côté. Schemes for robust quantum computation with polar molecules. *Phys. Rev. A*, 74:050301, Nov 2006.